

New *Hubble Space Telescope* Discoveries of Type Ia Supernovae at $z \geq 1$: Narrowing Constraints on the Early Behavior of Dark Energy¹

Adam G. Riess^{2,3}, Louis-Gregory Strolger⁴, Stefano Casertano³, Henry C. Ferguson³, Bahram Mobasher³, Ben Gold², Peter J. Challis⁵, Alexei V. Filippenko⁶, Saurabh Jha⁶, Weidong Li⁶, John Tonry⁷, Ryan Foley⁶, Robert P. Kirshner⁵, Mark Dickinson⁸, Emily MacDonald⁸, Daniel Eisenstein⁹, Mario Livio³, Josh Younger⁵, Chun Xu³, Tomas Dahlén³, and Daniel Stern¹⁰

ABSTRACT

We have discovered 21 new Type Ia supernovae (SNe Ia) with the *Hubble Space Telescope* (*HST*) and have used them to trace the history of cosmic expansion over the last 10 billion years. These objects, which include 13 spectroscopically confirmed SNe Ia at $z \geq 1$, were discovered during 14 epochs of reimaging of the GOODS fields North and South over two years with the Advanced Camera for Surveys on *HST*. Together with a recalibration of our previous *HST*-discovered SNe Ia, the full sample of 23 SNe Ia at $z \geq 1$ provides the highest-redshift sample known. Combined with previous SN Ia datasets, we measured $H(z)$ at discrete, uncorrelated epochs, reducing the

¹Based on observations with the NASA/ESA *Hubble Space Telescope*, obtained at the Space Telescope Science Institute, which is operated by AURA, Inc., under NASA contract NAS 5-26555.

²Department of Physics and Astronomy, Johns Hopkins University, Baltimore, MD 21218.

³Space Telescope Science Institute, 3700 San Martin Drive, Baltimore, MD 21218.

⁴Department of Physics and Astronomy, Western Kentucky University, 1906 College Heights Blvd., Bowling Green, KY 42101-1077

⁵Harvard-Smithsonian Center for Astrophysics, 60 Garden St., Cambridge, MA 02138.

⁶Department of Astronomy, 601 Campbell Hall, University of California, Berkeley, CA 94720-3411.

⁷Institute for Astronomy, University of Hawaii, 2680 Woodlawn Drive, Honolulu, HI 96822.

⁸NOAO, Tucson, AZ 85726-6732.

⁹Steward Observatory, University of Arizona, Tucson, AZ 85721-0065.

¹⁰Jet Propulsion Laboratory, California Institute of Technology, Pasadena, CA 91109

uncertainty of $H(z > 1)$ from 50% to under 20%, strengthening the evidence for a cosmic jerk—the transition from deceleration in the past to acceleration in the present. The unique leverage of the *HST* high-redshift SNe Ia provides the first meaningful constraint on the dark energy equation-of-state parameter at $z \geq 1$. The result remains consistent with a cosmological constant ($w(z) = -1$), and rules out rapidly evolving dark energy ($dw/dz \gg 1$). The defining property of dark energy, its negative pressure, appears to be present at $z > 1$, in the epoch preceding acceleration, with $\sim 98\%$ confidence in our primary fit. Moreover, the $z > 1$ sample-averaged spectral energy distribution is consistent with that of the typical SN Ia over the last 10 Gyr, indicating that any spectral evolution of the properties of SNe Ia with redshift is still below our detection threshold.

subject headings: galaxies: distances and redshifts — cosmology: observations — cosmology: distance scale — supernovae: general

1. Introduction

The accelerating cosmic expansion first inferred from observations of distant type Ia supernovae (SNe Ia; Riess et al. 1998; Perlmutter et al. 1999) indicates unexpected gravitational physics, frequently attributed to the dominating presence of a “dark energy” with negative pressure. Increasingly incisive samples of SNe Ia at $z < 1$ have reinforced the significance of this result (Tonry et al. 2003; Knop et al. 2003; Barris et al. 2004; Conley et al. 2006; Astier et al. 2006). Using the new Advanced Camera for Surveys (ACS) and refurbished NICMOS camera on the *Hubble Space Telescope (HST)*, our collaboration secured observations of a sample of the most-distant known SNe Ia. These half-dozen SNe Ia, all at $z > 1.25$, helped confirm the reality of cosmic acceleration by delineating the transition from preceding cosmic deceleration during the matter-dominated phase and by ruling out simple sources of astrophysical dimming (Riess et al. 2004b, hereafter R04). The expanded sample of 23 SNe Ia at $z \geq 1$ presented here are now used to begin characterizing the early behavior of dark energy.

Other studies independent of SNe Ia now strongly favor something like dark energy as the dominant component in the mass-energy budget of the Universe. Perhaps most convincingly, observations of large-scale structure and the cosmic microwave background radiation provide indirect evidence for a dark-energy component (e.g., Spergel et al. 2006). Measurements of the integrated Sachs-Wolfe effect (e.g., Afshordi, Loh, & Strauss 2004; Boughn & Crittenden 2004; Fosalba et al. 2003; Nolta et al. 2004; Scranton et al. 2005) more directly suggest the presence of dark energy with a negative pressure. Additional,

albeit more tentative, evidence is provided by observations of X-ray clusters (Allen et al. 2004) and baryon oscillations (e.g., Eisenstein et al. 2005).

The unexplained existence of a dominant, dark-energy-like phenomenon presents a stiff challenge to the standard model of cosmology and particle physics. The apparent acceleration may result from exotic physics such as the repulsive gravity predicted for a medium with negative pressure or from entirely new physics. The explanation of strongest pedigree is Einstein’s famous “cosmological constant” Λ (i.e., vacuum energy; Einstein 1917), followed by a decaying scalar field similar to that already invoked for many inflation models (i.e., quintessence – Wetterich 1995, Caldwell, Davé, & Steinhardt 1998; Peebles & Ratra 2003). Competitors include the Chaplygin gas (Bento, Bertolami, & Sen 2002), topological defects, and a massless scalar field at low temperature. Alternatively, alterations to General Relativity may be required as occurs from the higher-dimensional transport of gravitons in string theory models (Deffayet et al. 2002) and braneworlds, or by finely-tuned, long-range modifications (e.g., Cardassian type, Freese 2005; or Carroll et al. 2004; see Szydlowski, Kurek, & Krawiec 2006 for a review). Empirical clues are critical for testing hypotheses and narrowing the allowed range of possible models.

SNe Ia remain one of our best tools for unraveling the properties of dark energy because their individual measurement precision is unparalleled and they are readily attainable in sample sizes of order 10^2 , statistically sufficient to measure dark-energy-induced changes to the expansion rate of $\sim 1\%$. Specifically, the equation-of-state parameter of dark energy, w (where $P = w\rho c^2$) determines both the evolution of the density of dark energy,

$$\rho_{DE} = \rho_{DE,0} \exp\left\{3 \int_a^1 \frac{da}{a} (1 + w(a))\right\}, \quad (1)$$

and its gravitational effect on expansion,

$$\ddot{a}/a = (-4\pi G/3)[\rho_m + \rho_{DE}(1 + 3w(a))], \quad (2)$$

where $\rho_{DE,0}$ is the present dark-energy density. Measuring changes in the scale factor, a , with time from the distance and redshift measurements of SNe Ia,

$$\frac{d_l(z)}{c(1+z)} = \int_t^{t_0} \frac{dt'}{a(t')} = \int_0^z \frac{dz'}{H(z')}, \quad (3)$$

constrains the behavior of $w(a)$ or $w(z)$ and is most easily accomplished at $z < 2$ during the epoch of dark-energy dominance.

Ideally, we seek to extract the function $w(z)$ for dark energy or its mean value at a wide range of epochs. Alternatively, we might constrain its recent value $w_0 \equiv w(z = 0)$ and a derivative, $dw/dz \equiv w'$, which are exactly specified for a cosmological constant to be

$(-1,0)$. Most other models make less precise predictions. For example, the presence of a “tracker” dark-energy field whose evolution is coupled to the (decreasing) dark matter or radiation density may be detected by a measured value of $w' > 0$ or $w(z > 1) \sim 0$. In truth, we know almost nothing of what to expect for $w(z)$, so the safest approach is to assume nothing and measure $w(z)$ across the redshift range of interest. SN Ia at $z > 1$ are crucial to constrain variations of w with redshift. These measurements can only be made from space, and we report here on that endeavor. We have discovered and measured 21 new SN Ia with HST and used them to constrain the properties of the dark energy. We present the follow-up spectroscopy and photometry of the new SNe Ia in §2, light-curve analysis and cosmological constraints in §3, a discussion in §4, and a summary in §5.

2. Further Discoveries and Data Reprocessing

2.1. ACS Searches, 2003–2005

In *HST* Cycle 11 (July 2002 – June 2003) we initiated the first space-based program designed to find and monitor SNe (R04). Our search was conducted by imaging the two high-latitude fields of the GOODS Treasury Program (the *Chandra* Deep Field South and the *Hubble* Deep Field North) with 15 ACS pointings, 5 times each at 6 or 7-week intervals (chosen to match the rise time of SNe Ia at $z \approx 1$). Multiple exposures in the *F850LP* bandpass were differenced to find transients. Contemporaneous color measurements and host-galaxy photometric redshifts were utilized to identify promising candidate SNe Ia at $z > 1$ for target-of-opportunity (ToO) follow-up observations (Riess et al. 2004a).

In *HST* Cycles 12 and 13 (July 2003 – June 2005) we continued our past efforts, imaging the GOODS fields (Giavalisco et al. 2004, Strolger et al. 2004) 14 more times and following newly discovered SN Ia candidates with *HST*. The observational methods we used in Cycles 12 and 13 were very similar to those of Cycle 11 and are extensively described by R04. Readers are directed to that publication for the sake of brevity; here we describe only *changes* to our observing and candidate-selection strategies.

To improve our search efficiency with finite observing time, we compressed our primary search exposures from 2 orbits to 1. We omitted the short-wavelength filters, whose use in the GOODS program was primarily to constrain the properties of galaxy formation. Our typical search sequence contained four dithered exposures of length 400 s in *F850LP* and one 400 s exposure in *F775W* for a typical orbit instead of the previous four exposures of 500 s length in *F850LP* (as well as two such exposures in each *F606W* and *F775W*). At times when we had unusually long orbits, especially approaching the continuous viewing

zone for the HDFN, we included a ~ 200 s exposure in $F606W$ as well to help constrain SN type and redshift.

Although our net exposure time was reduced by 20% from the Cycle 11 observations, the accumulation of additional template images for the host galaxies without the supernova during the GOODS program increased their total depth and more than compensated for the slightly decreased signal in this search.

We benefited from two modest improvements in our ability to identify high-redshift SNe Ia before initiating a ToO over the strategy utilized by R04. The first was the availability of spectroscopic host-galaxy redshifts obtained before the appearance of a SN candidate (e.g., from our Keck and other spectra assembled for the GOODS catalog, and from “Team Keck”; Wirth et al. 2004). The second was the result of building up a 3 year baseline of variability for each galaxy. This allowed us to distinguish between transient signals caused by supernovae and transient noise introduced by the variable emission from active galactic nuclei.

The 21 new SNe Ia are listed in Table 1 and their discovery images are shown in Figure 1. Internal names for the SNe are used in the following. Color images of all of the SN Ia host galaxies (where filters $F850LP$, $F606W$, and $F435W$ correspond to red, green, and blue, respectively) are shown in Figure 2, with the position of the SN indicated in each case.

2.2. Photometry

Our follow-up observations of candidate SNe Ia were similar to those previously obtained and described by R04. After the search phase, all images were reprocessed using up-to-date reference files and the CALACS pipeline in the STSDAS package in IRAF.⁸ Because improvements have been made to the standard CALACS pipeline (including an improved distortion map and more precise flatfield images), we also reprocessed all preceding SN data from our first year.

To produce light curves, we developed an automated pipeline to retrieve all images obtained by ACS and NICMOS in the GOODS fields from the Multimission Archive (reprocessing all data from R04 as well as all of the new frames). The enhanced set of images available from before and after each SN increased the depth of the constructed

⁸IRAF is distributed by the National Optical Astronomy Observatories, which are operated by the Association of Universities for Research in Astronomy, Inc., under cooperative agreement with the National Science Foundation.

Table 1. SN Discovery Data

Name	Nickname	JD–2,400,000	SN α (J2000)	SN δ (J2000)
HST04Sas	Sasquatch	53148.7	12:36:54.11	+62:08:22.76
HST04Man	Manipogo	53146.3	12:36:34.81	+62:15:49.06
HST04Yow	Yowie	53145.2	12:36:34.33	+62:12:12.95
HST04Pat	Patuxent	53196.3	12:38:09.00	+62:18:47.24
HST04Tha	Thames	53196.5	12:36:55.17	+62:13:04.05
HST04Cay	Cayanne*	53245.2	12:37:27.11	+62:12:07.68
HST04Eag	Eagle	53284.9	12:37:20.75	+62:13:41.50
HST04Haw	Hawk	53284.0	12:35:41.16	+62:11:37.19
HST05Spo	Spock	53376.8	12:37:06.53	+62:15:11.70
HST04Mcg	McGuire	53265.0	03:32:10.02	–27:49:49.98
HST04Gre	Greenberg	53265.0	03:32:21.49	–27:46:58.30
HST04Omb	Ombo	53356.3	03:32:25.34	–27:45:03.01
HST04Rak	Rakke	53356.3	03:32:18.15	–27:44:10.55
HST04Kur	Kurage	53355.2	03:32:36.03	–27:51:17.66
HST05Dic	Dickinson	53472.5	12:35:49.61	+62:10:11.96
HST05Fer	Ferguson	53472.6	12:36:25.10	+62:15:23.84
HST05Koe	Koekemoer	53472.7	12:36:22.92	+62:18:23.20
HST05Str	Strolger	53474.5	12:36:20.63	+62:10:50.58
HST05Gab	Gabi	53474.5	12:36:13.83	+62:12:07.56
HST05Red	Redford	53426.6	12:37:01.70	+62:12:23.98
HST05Lan	Lancaster	53427.1	12:36:56.72	+62:12:53.33
HS05Zwi	Zwicky	53403.2	03:32:45.65	–27:44:24.30

*not positively identified as SN Ia

template image (without SN light) for each SN, thereby increasing the subsequent precision of the SN photometry.

Two modest improvements to measurements of SN flux were made from the methods described by R04. First, due to backside scattering from the ACS WFC CCD mounting, the point-spread function (PSF) redward of $\sim 8500 \text{ \AA}$ displays a halo of scattered light which needs to be quantified for precise photometry in the $F850LP$ bandpass. R04 used a red star with $i-z$ color similar to a SN Ia at peak at $z \approx 1.3$ ($i-z = 1.0$ mag, Vega) as a model PSF for SN photometry. However, variations in SN redshift and phase around that model make the match with a single PSF at a single color inexact resulting in photometric errors ranging from ± 0.05 mag for our sample of phases and redshifts. Here, we adopted an individualized method for the PSF modeling of high-redshift SNe Ia. As described in detail by Casertano & Riess (2007), we used 6 observed monochromatic PSFs from ACS narrow-band filters between 8150 \AA and 10500 \AA to derive an empirical wavelength dependent correction to the average PSF model. At these monochromatic endpoints the difference between (nearly) infinite-aperture photometry and that determined from a fit to the previously used red-star PSF is -0.14 mag and $+0.46$ mag, respectively, with no difference occurring near 9300 \AA . These differences were evaluated for all monochromatic wavelengths. At every SN redshift and phase, the same representative model SN Ia spectral energy distribution (SED) used to derive K-corrections was used to integrate the monochromatic PSFs within the $F850LP$ band response and determined their photometric differences. In Figure 3 we show the required photometric correction as a function of SN Ia age and redshift. Spatial variations in the ACS WFC PSF are small (Krist 2003) and variations in the position of the SNe result in a PSF noise of 1-2%, well below the sky and read noise.

Second, we adopted an updated zeropoint for the *HST* ACS “Vegamag” photometric system from Sirianni et al. (2005) which uses the spectrophotometry of Vega from Bohlin & Gilliland (2004) and improved quantum efficiency data for ACS to set Vega to 0.00 mag in all passbands. We then utilized the same magnitudes of Vega assumed by Landolt (1992) to calibrate the *HST* photometry on the same Vega system as the nearby SN Ia sample. Thus our data is calibrated on the Landolt system. The resulting zeropoints corresponding to 1 electron s^{-1} are $F850LP = 24.35$, $F775W = 25.28$, and $F606W = 26.43$ mag. These are fainter than those used in R04 by 0.02 mag. For NICMOS we use the values of $F110W = 22.92$ mag and $F160W = 22.11$ mag given by the STScI NICMOS Handbook.

An improvement in our ability to estimate photometric errors was provided by the increased set of host images long before or after the appearance of the SNe. For each such image we added and measured an ideal PSF at a range of magnitudes at the *same* pixel position as the site of the SN and derived statistics from the recovered magnitudes such as

their dispersion and their bias at a given magnitude.¹¹

The calibration of *HST* NICMOS NIC2 photometry has changed since R04 due to the recent detection of an apparent non-linearity in all NICMOS detectors. This effect was initially discovered by Bohlin, Lindler, & Riess (2005) and has now been calibrated to good precision by de Jong et al. (2006) using pairs of star-cluster images obtained with the flatfield lamps switched on and off. The result for NIC2 is a reduction in the apparent flux by 0.06 and 0.03 mag per dex in *F110W* and *F160W*, respectively.¹²

For faint sources such as high-redshift SNe Ia, the nonlinearity in apparent flux pertains to the flux difference between the calibration stars (G191B2B and P330E, both ~ 12 mag in *J* and *H*) and the faint SN. For SN fluxes fainter than the sky level (all of those presented here) the nonlinearity pertains to the flux difference between the calibration stars and the sky level, below which any additional nonlinearity of sources is effectively “quenched”. For SN Ia plus host fluxes near or below the sky (a typical sky level is 0.17 electron s^{-1} in *F110W* and 0.14 electron s^{-1} in *F160W*), the correction we calculate and apply is 0.220 mag brighter (than the uncorrected zeropoints) in *F110W* and 0.086 mag brighter in *F160W*. Interestingly, the change in distance modulus from R04 due to these corrections is mitigated by their compensating effect in distance and reddening.¹³

SNe measured in our detection and follow-up observations are generally of high enough signal-to-noise ratio ($S/N > 10$) to support the use of magnitudes (where a magnitude is zeropoint $-2.5 \log_{10} \text{flux}$) without skewing the interpretation of photometric errors. The infrequent observation (less than 5% of observations) with ($S/N < 5$) on the post-maximum light curve of any SN has insignificant weight when used in conjunction with the higher

¹¹We found biases to exist only for the case of bright, sharp hosts which were “softened” by image interpolation in the registration of the template. The worst case hosts such as 2003XX and 2002hp seen in Figures 1 and 2 without correction would bias the magnitudes too bright by as much as 0.2 mag at the end of the observed light curve. We identified two valid solutions to this bias which gave consistent results: (1) equally soften the SN image by reinterpolation, or (2) estimate the bias from the simulated SNe Ia. This latter option is preferable as it is nearly noise-free.

¹²The correction is described by de Jong et al. (2006) in the form: count rate $\propto \text{flux}^\alpha$, where $\alpha = 1.025 \pm 0.002$ and $\alpha = 1.012 \pm 0.006$ for *F110W* and *F160W*, respectively.

¹³Because the change in the bluer band (*F110W*) is larger, the net change in the distance moduli from R04 to first order is approximately $\Delta F_{110W} - R(\Delta F_{110W} - \Delta F_{160W})$, which for a reddening ratio $R \approx 3$ is 0.17 mag. In practice, a second-order change occurs as the apparent color impacts other parameters in the fit as well as the individual K-corrections. For the highest-redshift SNe which rely heavily on NICMOS data, the average change from R04 was found to be 5% (0.10 mag) closer in distance, but depends on the individual SN Ia.

signal-to-noise ratio points. However, our *pre-discovery* images require the use of flux measurement and error estimates due to their greater leverage on the determination of the time of maximum. For these images we measured the sky-subtracted flux (electrons per second) in a $0.17''$ radius aperture within which the zeropoint for a 1 electron per second source is 24.68 mag for *F850LP*.

Our final photometry for all SNe Ia is listed in Table 2 and shown compared to the individual multicolor light-curve shape (MLCS) fits in Figure 4.

2.3. Spectroscopy and SN Identification

The ACS grism spectroscopy we obtained for the SNe Ia is listed in Table 3 (they will also be made available at the University of Oklahoma supernova spectra database, SUSPECT). In general, our reduction and analysis methods were the same as in R04 with the following exceptions. A more realistic skyflat was used to separate the contributions to each pixel from the sky and the source as described in Pirzkal et al. (2005). We also utilized a Lanczos kernel in the drizzling procedure to decrease the effective size of the pixel convolved with the images and improve the separation for cases where the SN and host were very close together (e.g., SN HST04Sas).

The spectra we obtained and used to classify the SNe are shown in Figure 5. As in R04, to classify the SNe, the detected SN spectra were cross-correlated with template spectra (after removal of the continuum) to identify their type and redshift using the “SNID” algorithm (Tonry et al. 2003, Blondin et al. 2006). For the cases listed in Table 3 for which narrow-line host emission was identified, the redshift was constrained to the value determined from the host emission before cross-correlation, improving the significance of the cross-correlation peak. For all 12 spectra shown in Figure 5, SNID provided a significant classification for each as type Ia. Although the diagnostic used by the SNID algorithm relies on the whole spectrum, the majority of these SNe can also be classified as type Ia from the presence of Si II absorption at 4130 \AA (Coil et al. 2000). Specifically, evidence of Si II absorption was seen in the two highest-redshift spectra presented here. Broad Ca II absorption near 3750 \AA is visible in all the spectra as well, but this feature is less secure than Si II for SN Ia classification due to its appearance in the spectra of SNe Ic (Filippenko 1997). For the highest redshift spectrum shown, HST04Sas, *F110W*, *F160W*, and *F205W* band NIC2 imaging of the host was obtained to constrain the phot- z of the red, elliptical host to $z = 1.4 \pm 0.15$ which compares well with the SN value of $z = 1.39 \pm 0.01$.

For SN HST04Cay cross-correlation peaks exist, but none with high significance and

the redshift of the host is not known. For HST05Red, the spectral match to a SN Ia at the host $z = 1.189$ in Table 3 is fair, but not secure. SN 2003XX, identified by R04 as an SN Ia on the basis of its elliptical host, is now spectroscopically classified as an SN Ia due to the acquisition of an ACS grism spectroscopic galaxy-only template on 2005-03-07 to subtract from the grism spectrum of the SN obtained on 2003-04-16 and heavily contaminated by galaxy light. We also analyzed the ACS grism spectra of two more apparent high-redshift SNe observed by another collaboration (GO-9729; P.I. Perlmutter) during the course of Cycle 12 in the GOODS fields (SN150G $\alpha = 12:37:09.456$, $\delta = +62:22:15.59$; SN150I at $\alpha = 12:37:51.533$, $\delta = +62:17:08.24$) but failed to find a significant peak in the cross-correlation so we cannot determine their type or redshift.

Because of the large range in the quality and breadth of the photometric record of individual SNe Ia, R04 developed a two-tiered approach to the confidence of our SN Ia identifications. By distinguishing or selecting data based on objective criteria of their good quality we can mitigate systematic errors caused by undersampling of light curves and misidentifications without introducing cosmological biases.

To summarize this approach: we classify as “high-confidence” (hereafter as “Gold”) SNe Ia those with a compelling classification and whose photometric record is sufficient to yield a robust distance estimate easily characterized by its measurement uncertainty. “Likely but uncertain SNe Ia” (hereafter “Silver”) are those with an aspect of the spectral or photometric record which is absent or suspect and whose distance error is described with a caveat rather than a quantitative uncertainty. As in R04, the three primary reasons for rejecting a SN Ia from the Gold set are that (1) the classification, though plausible, was not compelling, (2) the photometric record is too sparse to yield a robust distance (i.e., the number of model parameters is approximately equal to the effective number of samplings of the light and color curves, and (3) the extinction is so large as to be uncertain due to our ignorance of extragalactic extinction laws. Although R04 set this extinction threshold to 1 mag of visual extinction, here we adopt the more conservative threshold of 0.5 mag utilized elsewhere (Miknaitis et al. 2007; Tonry et al. 2003; Riess et al. 2005). SNe with two liens against its confidence (i.e., those rejected from the “Silver” set) are not included in the remainder of this paper (e.g., HST05Cay).

The measured SN Ia distances for the full Gold and Silver set of *HST*-discovered SNe are given in Table 6, including the revised distance measurements of the HST objects first presented by R04. These distances use the same distance scale as in R04. To this sample we add the same ground-discovered sample of SNe Ia employed in R04 for the following

analyses¹⁴

An important and recent addition to the ground-discovered sample is the first-year SNLS dataset from Astier et al. (2006) containing 73 new SNe Ia. We sought to define a similarly high-confidence subsample from this set using the information available from Astier et al. (2006) and Howell et al. (2005).

We removed from the full-sample 2 events discarded by the SNLS (SNLS-03D4au and SNLS-03D4bc), as well as the 15 objects classified by Howell et al. (2005) and Astier et al. (2006) as “SN Ia*,” meaning they are “probable SN Ia” but among the “least secure identification,” and another type (such as a SN Ic) is not excluded. As discussed by Astier et al. (2006), most of the objects at $z > 0.8$ suffer from imprecise color measurements which dominate the distance error and would lead to a distance bias after application of a low-extinction cut. However, the low-extinction cut is valuable to reduce the sensitivity to unexpected or evolving extinction laws. Our solution is to first eliminate objects with highly uncertain color measurements, $\sigma_{color} > 0.15$ mag, which removes the following 6 objects: SNLS-03D1ew, SNLS-03D4cn, SNLS-03D4cy, SNLS-04D3cp, SNLS-04D3dd, and SNLS-04D3ny. The distance uncertainty of these objects is typically 2 to 3 times that of the rest of the objects and thus the value of these 6 is very low (roughly the equivalent of losing a single well-measured SN Ia). Lastly, the same color cut of $A_V < 0.5$ mag used for all Gold sample SNe removes 3 objects: SNLS-03D1gt, SNLS-03D3ba, and SNLS-04D2gc. Thus, 47 high-confidence SNLS objects remain classified as “Gold”. The SNLS SNe were fit with our present MLCS2k2 algorithm to estimate their distances. Alternatively, we found that after the addition of 0.19 mag to distances measured to the SNLS SNe by Astier et al. (2006) (to account for the arbitrary choice of distance scale and determined from low-redshift SNe in common), the agreement between our MLCS2k2 measured distances on the distance scale used in R04 and here and those from Astier et al. (2006) were consistent in the mean to better than 0.01 mag. Thus, either set of distances measured to the SNLS SNe provide a comparable and suitable addition to our cosmological sample. We verified (next section) that either yields the same inferences for $w(z)$ and provide results fitting the SNLS SNe with either method in Table .¹⁵

¹⁴As in R04, past SN data such as light curves and spectra from Perlmutter et al. (1999) and spectra from the sample of Knop et al. (2003) remain unavailable. Thus we resort to the same reliance as in R04 on their published distances normalized to a consistent distance scale using SNe in common and classification confidences from these authors. In §4 we also consider the impact of rejecting these and other older data.

¹⁵We made use of the Astier et al. (2006) distances for our primary fit as their light curves were not initially published by Astier et al. and only recently made available during the preparation of this work.

We have not made use of any of the seven high-redshift SNe Ia from Krisciunas et al. (2005) due to the apparently biased selection of the sample, as discovered by Krisciunas et al. but not yet fully modeled and corrected.

Thus, a simple description of the full sample used here for the cosmological analyses consists of the addition of Table 5 from R04 to Table 6 provided here with the revised distances to the SNe in common (i.e., the leading 20 SNe in Table 6) superceding those given in R04 Table 5, and the SNLS objects from Astier et al. (2006) identified in §2.3. Either the Astier et al. (2006) provided distances (with the aforementioned addition of 0.19 mag) or our own fits are comparable and suitable. The sample can also be found at <http://braeburn.pha.jhu.edu/~ariess/R06> or upon request to ariess@stsci.edu.

Upcoming revisions to the ground-discovered samples and improvements to the distance-fitting algorithms are expected and will change the membership and distance measures in the full cosmological sample and these should be considered before construction of a cosmological sample of SNe Ia. In response to such improvements we will attempt to provide distance estimates to the HST-discovered sample with updated fitting tools or distance scaling as warranted at <http://braeburn.pha.jhu.edu/~ariess/R06> or upon request to ariess@stsci.edu.

Table 2. SN Ia Imaging

Date ^a	Vega Mag	Epoch(rest)	K-Corr
HST04Pat ($z = 0.97$)			
	<i>F775W</i>		<i>F775W</i> \rightarrow <i>U</i>
53196.3	23.86(0.04)	-1.1	-0.63(0.10)
53205.1	23.80(0.10)	3.3	-0.73(0.08)
	<i>F850LP</i>		<i>F850LP</i> \rightarrow <i>B</i>
53196.3	23.77(0.04)	-1.1	-1.25(0.05)
53205.1	23.81(0.04)	3.3	-1.28(0.04)
53205.4	23.77(0.04)	3.4	-1.28(0.04)
53225.3	24.45(0.04)	13.5	-1.35(0.05)
53377.7	27.01(0.40)	90.9	-1.49(0.01)
HST04Mcg ($z = 1.37$)			
	<i>F850LP</i>		<i>F850LP</i> \rightarrow <i>U</i>
53265.0	24.44(0.04)	5.9	-1.01(0.03)
53275.6	24.61(0.06)	10.4	-1.06(0.04)
53285.6	25.39(0.14)	14.6	-1.11(0.02)
53294.7	25.69(0.17)	18.4	-1.12(0.01)
53306.5	25.95(0.14)	23.4	-1.15(0.02)
53312.3	27.00(0.50)	25.9	-1.16(0.02)
	<i>F110W</i>		<i>F110W</i> \rightarrow <i>B</i>
53277.6	24.22(0.05)	11.2	-1.71(0.07)
53286.6	24.59(0.09)	15.0	-1.77(0.12)
	<i>F160W</i>		<i>F160W</i> \rightarrow <i>R</i>
53277.7	23.99(0.05)	11.3	-1.93(0.05)
53285.6	24.37(0.12)	14.6	-1.90(0.02)
53217.9	flux:0.180(0.06)	-13.9	—(—)
HST05Fer ($z = 1.02$)			
	<i>F775W</i>		<i>F775W</i> \rightarrow <i>U</i>
53486.8	24.55(0.10)	10.1	-0.82(0.04)
	<i>F850LP</i>		<i>F850LP</i> \rightarrow <i>B</i>
53472.6	23.58(0.03)	3.1	-1.39(0.02)
53486.8	24.14(0.04)	10.1	-1.40(0.01)
53493.8	24.28(0.06)	13.6	-1.40(0.02)
53504.3	24.99(0.08)	18.8	-1.43(0.03)
53513.2	25.24(0.08)	23.2	-1.45(0.01)
53527.3	26.08(0.17)	30.2	-1.45(0.01)
	<i>F110W</i>		<i>F110W</i> \rightarrow <i>V</i>
53486.4	23.73(0.05)	9.9	-1.40(0.05)
53491.2	23.87(0.06)	12.3	-1.37(0.05)
53427.7	flux:-0.03(0.03)	-19.0	—(—)
HST05Koe ($z = 1.23$)			
	<i>F775W</i>		<i>F775W</i> \rightarrow <i>U</i>

Table 2—Continued

Date ^a	Vega Mag	Epoch(rest)	K-Corr
53472.7	25.18(0.05)	8.5	-0.15(0.05)
53486.8	26.11(0.10)	14.8	-0.07(0.03)
	<i>F850LP</i>		<i>F850LP</i> → <i>B</i>
53472.7	24.34(0.06)	8.5	-1.43(0.01)
53486.8	25.11(0.07)	14.8	-1.40(0.04)
53493.8	25.34(0.11)	18.0	-1.34(0.08)
53504.3	25.90(0.15)	22.7	-1.24(0.04)
53513.2	26.10(0.16)	26.7	-1.19(0.02)
53527.3	27.10(0.40)	33.0	-1.18(0.03)
	<i>F110W</i>		<i>F110W</i> → <i>V</i>
53485.3	24.48(0.07)	14.1	-1.46(0.08)
53491.3	24.66(0.09)	16.8	-1.42(0.09)
HST05Dic ($z = 0.638$)			
	<i>F606W</i>		<i>F606W</i> → <i>U</i>
53472.5	23.42(0.02)	4.3	0.160(0.03)
	<i>F775W</i>		<i>F775W</i> → <i>B</i>
53472.5	22.61(0.02)	4.3	-0.96(0.03)
	<i>F850LP</i>		<i>F850LP</i> → <i>V</i>
53472.5	22.44(0.02)	4.3	-1.06(0.02)
53530.8	23.97(0.02)	39.9	-1.09(0.01)
HST04Gre ($z = 1.14$)			
	<i>F775W</i>		<i>F775W</i> → <i>U</i>
53265.1	23.61(0.04)	1.0	-0.46(0.01)
53288.5	24.58(0.05)	12.0	-0.46(0.01)
53299.5	25.22(0.07)	17.1	-0.46(0.01)
53313.2	25.57(0.10)	23.5	-0.47(0.01)
	<i>F850LP</i>		<i>F850LP</i> → <i>B</i>
53265.1	23.25(0.02)	1.0	-1.51(0.02)
53275.6	23.38(0.02)	6.0	-1.49(0.02)
53288.5	24.00(0.05)	12.0	-1.47(0.03)
53299.5	24.68(0.10)	17.1	-1.43(0.05)
53313.2	24.98(0.07)	23.5	-1.36(0.02)
53356.3	26.26(0.31)	43.7	-1.32(0.03)
53378.4	26.31(0.38)	54.0	-1.37(0.02)
53388.6	25.94(0.26)	58.8	-1.36(0.01)
53398.1	26.79(0.32)	63.2	-1.37(0.01)
53404.2	26.10(0.23)	66.0	-1.37(0.01)
	<i>F110W</i>		<i>F110W</i> → <i>V</i>
53290.5	23.62(0.05)	12.9	-1.49(0.06)
53301.2	23.90(0.05)	17.9	-1.42(0.05)
53217.2	flux:-0.05(0.04)	-21.2	—(—)

Table 2—Continued

Date ^a	Vega Mag	Epoch(rest)	K-Corr
HST04Omb ($z = 0.975$)			
	<i>F775W</i>		<i>F775W</i> → <i>U</i>
53356.3	23.82(0.05)	-5.5	-0.58(0.05)
53373.7	23.81(0.05)	3.2	-0.74(0.07)
53378.5	24.06(0.06)	5.7	-0.79(0.05)
53388.6	24.46(0.06)	10.8	-0.86(0.05)
53398.1	24.77(0.07)	15.6	-0.93(0.02)
53404.1	25.09(0.08)	18.6	-0.94(0.01)
	<i>F850LP</i>		<i>F850LP</i> → <i>B</i>
53356.3	23.78(0.04)	-5.5	-1.26(0.02)
53373.7	23.58(0.03)	3.2	-1.30(0.03)
53378.4	23.61(0.03)	5.6	-1.32(0.02)
53388.6	23.99(0.05)	10.8	-1.34(0.03)
53398.1	24.31(0.06)	15.6	-1.39(0.05)
53404.2	24.40(0.06)	18.7	-1.44(0.06)
53407.9	24.50(0.07)	20.6	-1.47(0.05)
	<i>F110W</i>		<i>F110W</i> → <i>V</i>
53368.9	23.31(0.04)	0.8	-1.43(0.02)
53377.8	23.54(0.04)	5.3	-1.41(0.06)
HST05Red ($z = 1.19$)			
	<i>F775W</i>		<i>F775W</i> → <i>U</i>
53426.6	25.52(0.05)	12.0	-0.21(0.03)
53436.6	25.92(0.07)	16.6	-0.19(0.01)
	<i>F850LP</i>		<i>F850LP</i> → <i>B</i>
53426.6	24.42(0.04)	12.0	-1.38(0.04)
53436.6	24.74(0.06)	16.6	-1.34(0.07)
53439.6	25.10(0.11)	18.0	-1.30(0.07)
53445.5	25.47(0.14)	20.7	-1.26(0.07)
53454.8	26.22(0.21)	24.9	-1.20(0.02)
53463.3	26.58(0.25)	28.8	-1.19(0.03)
53471.7	26.75(0.34)	32.6	-1.21(0.02)
53472.9	26.65(0.20)	33.2	-1.21(0.03)
	<i>F110W</i>		<i>F110W</i> → <i>V</i>
53440.4	24.31(0.05)	18.3	-1.30(0.05)
	<i>F160W</i>		<i>F160W</i> → <i>R</i>
53440.5	23.51(0.08)	18.4	-1.69(0.13)
HST05Lan ($z = 1.23$)			
	<i>F775W</i>		<i>F775W</i> → <i>U</i>
53427.1	25.50(0.05)	-2.4	-0.24(0.05)
53436.6	25.75(0.05)	1.8	-0.19(0.05)
53436.7	25.88(0.10)	1.8	-0.19(0.05)

Table 2—Continued

Date ^a	Vega Mag	Epoch(rest)	K-Corr
	<i>F850LP</i>		<i>F850LP</i> → <i>B</i>
53427.2	24.75(0.10)	-2.4	-1.40(0.03)
53436.6	24.56(0.08)	1.8	-1.37(0.03)
53439.6	24.72(0.09)	3.1	-1.36(0.04)
53445.5	24.96(0.06)	5.8	-1.34(0.02)
53454.8	25.29(0.08)	9.9	-1.33(0.02)
53463.3	25.69(0.18)	13.7	-1.31(0.04)
53471.7	25.96(0.26)	17.5	-1.26(0.08)
53473.6	26.78(0.42)	18.4	-1.24(0.08)
	<i>F110W</i>		<i>F110W</i> → <i>V</i>
53439.4	24.40(0.06)	3.0	-1.56(0.05)
53445.4	24.43(0.06)	5.7	-1.53(0.06)
	<i>F160W</i>		<i>F160W</i> → <i>R</i>
53438.4	24.36(0.14)	2.6	-1.80(0.07)
53444.4	24.43(0.14)	5.3	-1.73(0.06)
HST04Tha ($z = 0.954$)			
	<i>F775W</i>		<i>F775W</i> → <i>U</i>
53196.5	24.19(0.05)	9.8	-0.91(0.05)
53207.7	25.16(0.10)	15.5	-0.99(0.02)
	<i>F850LP</i>		<i>F850LP</i> → <i>B</i>
53196.5	23.87(0.03)	9.8	-1.37(0.03)
53207.7	24.37(0.06)	15.5	-1.43(0.06)
53216.3	24.72(0.11)	19.9	-1.51(0.06)
53221.7	25.18(0.10)	22.6	-1.56(0.03)
53231.0	25.36(0.11)	27.4	-1.58(0.01)
53244.4	25.91(0.14)	34.3	-1.58(0.02)
53284.6	26.54(0.51)	54.8	-1.51(0.02)
	<i>F110W</i>		<i>F110W</i> → <i>V</i>
53208.2	24.17(0.07)	15.7	-1.25(0.03)
53146.4	flux:-0.01(0.05)	-15.8	—(—)
HST04Rak ($z = 0.74$)			
	<i>F606W</i>		<i>F606W</i> → <i>U</i>
53356.3	24.15(0.05)	2.5	0.362(0.01)
	<i>F775W</i>		<i>F775W</i> → <i>B</i>
53356.3	22.88(0.02)	2.5	-1.11(0.01)
53373.7	23.70(0.03)	12.5	-1.10(0.01)
53388.6	24.56(0.05)	21.1	-1.12(0.01)
53398.1	25.11(0.07)	26.5	-1.12(0.01)
53404.1	25.57(0.10)	30.0	-1.11(0.01)
53408.0	25.64(0.10)	32.2	-1.11(0.02)
	<i>F850LP</i>		<i>F850LP</i> → <i>V</i>

Table 2—Continued

Date ^a	Vega Mag	Epoch(rest)	K-Corr
53356.3	22.96(0.02)	2.5	-1.10(0.03)
53373.7	23.47(0.02)	12.5	-1.04(0.03)
53378.4	23.61(0.04)	15.2	-1.02(0.05)
53388.6	23.92(0.03)	21.1	-0.95(0.04)
53398.1	24.28(0.05)	26.5	-0.90(0.03)
53404.2	24.63(0.06)	30.0	-0.87(0.02)
53404.2	24.42(0.07)	30.0	-0.87(0.02)
53407.9	24.80(0.08)	32.2	-0.86(0.01)
53313.0	flux:0.070(0.06)	-22.3	—(—)
HST05Zwi ($z = 0.521$)			
	<i>F606W</i>		<i>F606W</i> → <i>B</i>
53415.9	22.94(0.02)	5.3	-0.27(0.03)
53435.0	24.13(0.02)	17.9	-0.14(0.06)
53443.1	24.52(0.10)	23.2	-0.04(0.03)
	<i>F775W</i>		<i>F775W</i> → <i>V</i>
53403.2	22.40(0.02)	-2.9	-0.86(0.02)
53415.9	22.19(0.10)	5.3	-0.81(0.04)
53435.1	23.04(0.02)	17.9	-0.71(0.07)
53443.2	23.30(0.02)	23.3	-0.61(0.07)
	<i>F850LP</i>		<i>F850LP</i> → <i>R</i>
53403.2	22.04(0.01)	-2.9	-0.84(0.04)
53415.9	22.16(0.02)	5.3	-0.90(0.04)
53435.1	22.95(0.02)	17.9	-0.97(0.04)
53443.2	22.91(0.02)	23.3	-0.90(0.06)
HST04Haw ($z = 0.490$)			
	<i>F606W</i>		<i>F606W</i> → <i>B</i>
53375.7	25.68(0.04)	49.4	-0.16(0.01)
53427.5	26.16(0.04)	84.2	-0.17(0.01)
53472.5	26.82(0.04)	114.4	-0.17(0.01)
	<i>F775W</i>		<i>F775W</i> → <i>V</i>
53284.0	23.97(0.03)	-12.0	-0.80(0.01)
53332.9	23.15(0.02)	20.7	-0.71(0.03)
53375.7	24.45(0.02)	49.4	-0.62(0.02)
53427.5	25.08(0.05)	84.2	-0.70(0.01)
	<i>F850LP</i>		<i>F850LP</i> → <i>R</i>
53284.0	23.81(0.03)	-12.0	-0.84(0.05)
53333.0	22.90(0.01)	20.8	-0.91(0.04)
53375.7	23.83(0.05)	49.4	-0.82(0.01)
53427.6	24.94(0.12)	84.3	-0.84(0.01)
53472.5	25.82(0.21)	114.4	-0.84(0.01)
53243.9	flux:0.020(0.08)	-38.9	—(—)

Table 2—Continued

Date ^a	Vega Mag	Epoch(rest)	K-Corr
HST04Kur ($z = 0.359$)			
	<i>F775W</i>		<i>F775W</i> → <i>V</i>
53355.2	23.60(0.02)	-5.3	-0.70(0.02)
53366.1	23.28(0.05)	2.6	-0.71(0.02)
53375.9	23.74(0.05)	9.9	-0.73(0.01)
53404.0	24.77(0.04)	30.5	-0.85(0.01)
53415.4	25.05(0.05)	38.9	-0.84(0.01)
53425.9	25.03(0.05)	46.6	-0.85(0.01)
	<i>F850LP</i>		<i>F850LP</i> → <i>R</i>
53355.3	23.04(0.02)	-5.2	-0.70(0.02)
53366.1	22.79(0.02)	2.6	-0.68(0.02)
53375.9	23.12(0.02)	9.9	-0.65(0.01)
53404.0	24.09(0.05)	30.5	-0.72(0.01)
53415.5	24.18(0.06)	39.0	-0.70(0.01)
53425.9	24.26(0.06)	46.6	-0.69(0.02)
HST04Yow ($z = 0.46$)			
	<i>F775W</i>		<i>F775W</i> → <i>V</i>
53145.1	22.73(0.01)	9.4	-0.75(0.02)
53157.0	23.18(0.01)	17.6	-0.72(0.03)
53169.4	23.70(0.01)	26.1	-0.67(0.02)
53195.2	24.42(0.30)	43.7	-0.66(0.02)
	<i>F850LP</i>		<i>F850LP</i> → <i>R</i>
53145.2	22.53(0.01)	9.5	-0.85(0.01)
53157.1	23.04(0.01)	17.7	-0.86(0.04)
53169.4	23.31(0.03)	26.1	-0.76(0.02)
53195.2	24.06(0.05)	43.7	-0.78(0.02)
53216.3	24.80(0.09)	58.2	-0.80(0.02)
53221.7	24.90(0.06)	61.9	-0.81(0.01)
53284.4	25.49(0.17)	104.8	-0.82(0.01)
53332.7	25.79(0.20)	137.9	-0.82(0.01)
53097.2	flux:0.050(0.06)	-23.3	—(—)
HST04Man ($z = 0.854$)			
	<i>F775W</i>		<i>F775W</i> → <i>B</i>
53146.3	23.38(0.04)	-1.0	-1.17(0.03)
53157.0	23.55(0.04)	4.7	-1.13(0.02)
53169.4	24.12(0.05)	11.4	-1.11(0.03)
53195.6	25.92(0.10)	25.5	-0.91(0.01)
	<i>F850LP</i>		<i>F850LP</i> → <i>V</i>
53146.3	23.35(0.05)	-1.0	-1.31(0.01)
53157.1	23.45(0.02)	4.8	-1.28(0.07)
53169.4	23.69(0.04)	11.4	-1.16(0.07)

Table 2—Continued

Date ^a	Vega Mag	Epoch(rest)	K-Corr
53195.6	25.04(0.10)	25.5	-0.75(0.06)
53207.7	25.94(0.21)	32.0	-0.68(0.02)
53098.0	flux:0.030(0.04)	-27.0	—(—)
HST05Spo ($z = 0.839$)			
	<i>F775W</i>		<i>F775W</i> → <i>B</i>
53427.1	24.06(0.04)	14.6	-1.12(0.04)
53427.3	23.95(0.04)	14.7	-1.12(0.04)
53436.6	24.67(0.05)	19.8	-1.04(0.06)
53436.6	24.76(0.10)	19.8	-1.04(0.06)
53473.6	26.30(0.30)	39.9	-0.98(0.01)
	<i>F850LP</i>		<i>F850LP</i> → <i>V</i>
53376.8	24.78(0.09)	-12.6	-1.17(0.04)
53427.2	23.66(0.03)	14.7	-1.09(0.10)
53427.4	23.61(0.04)	14.8	-1.09(0.10)
53436.6	24.00(0.05)	19.8	-0.93(0.10)
53439.6	24.17(0.07)	21.4	-0.88(0.08)
53445.5	24.35(0.06)	24.6	-0.80(0.08)
53454.8	24.91(0.10)	29.7	-0.71(0.03)
53463.3	25.11(0.09)	34.3	-0.70(0.04)
53471.7	25.37(0.12)	38.9	-0.73(0.02)
53473.6	25.31(0.21)	39.9	-0.73(0.03)
HST04Eag ($z = 1.02$)			
	<i>F775W</i>		<i>F775W</i> → <i>U</i>
53284.9	23.95(0.05)	-4.4	-0.63(0.03)
53332.1	26.59(0.60)	18.9	-0.84(0.01)
	<i>F850LP</i>		<i>F850LP</i> → <i>B</i>
53284.9	23.76(0.05)	-4.4	-1.34(0.02)
53296.9	23.60(0.02)	1.5	-1.36(0.02)
53305.6	23.70(0.03)	5.8	-1.37(0.01)
53316.5	24.19(0.04)	11.2	-1.38(0.02)
53326.2	24.62(0.07)	16.0	-1.40(0.03)
53332.2	24.93(0.11)	19.0	-1.42(0.03)
53334.9	24.96(0.07)	20.3	-1.42(0.03)
	<i>F110W</i>		<i>F110W</i> → <i>V</i>
53297.5	23.57(0.07)	1.8	-1.49(0.02)
53306.3	23.60(0.07)	6.1	-1.45(0.06)
HST05Gab ($z = 1.12$)			
	<i>F775W</i>		<i>F775W</i> → <i>U</i>
53474.5	24.52(0.05)	-6.0	-0.50(0.01)
53485.7	24.16(0.10)	-0.7	-0.50(0.02)
	<i>F850LP</i>		<i>F850LP</i> → <i>B</i>

Table 2—Continued

Date ^a	Vega Mag	Epoch(rest)	K-Corr
53474.5	23.83(0.04)	-6.0	-1.48(0.01)
53485.7	23.58(0.03)	-0.7	-1.48(0.02)
53493.9	23.66(0.03)	3.0	-1.48(0.02)
53504.2	23.88(0.04)	7.9	-1.47(0.02)
53513.3	24.24(0.04)	12.2	-1.44(0.03)
53530.8	25.38(0.13)	20.5	-1.38(0.03)
	<i>F110W</i>		<i>F110W</i> → <i>V</i>
53486.4	23.68(0.07)	-0.4	-1.57(0.02)
53492.3	23.60(0.07)	2.3	-1.57(0.03)
HST05Str ($z = 1.01$)			
	<i>F775W</i>		<i>F775W</i> → <i>U</i>
53474.5	23.93(0.04)	-0.0	-0.67(0.08)
53485.7	24.25(0.10)	5.4	-0.76(0.03)
	<i>F850LP</i>		<i>F850LP</i> → <i>B</i>
53474.5	23.67(0.03)	-0.0	-1.33(0.04)
53485.7	23.90(0.04)	5.4	-1.36(0.01)
53493.9	24.14(0.05)	9.5	-1.36(0.01)
53504.2	24.51(0.08)	14.7	-1.38(0.03)
53513.3	25.08(0.08)	19.2	-1.42(0.03)
	<i>F110W</i>		<i>F110W</i> → <i>V</i>
53485.4	23.85(0.12)	5.3	-1.45(0.06)
53492.2	23.99(0.12)	8.7	-1.41(0.04)
53426.8	flux:0.043(0.03)	-23.8	—(—)
HST04Sas ($z = 1.39$)			
	<i>F775W</i>		<i>F775W</i> → <i>U</i>
148.670	26.22(0.25)	-2.4	0.091(0.14)
	<i>F850lp</i> → <i>U</i>		
148.700	24.75(0.07)	-2.4	-0.96(0.06)
156.200	25.01(0.10)	0.7	-0.99(0.07)
163.600	25.13(0.08)	3.8	-1.04(0.05)
169.300	25.74(0.15)	6.2	-1.07(0.03)
176.100	25.54(0.14)	9.0	-1.08(0.03)
183.500	25.98(0.20)	12.1	-1.10(0.03)
190.400	26.29(0.25)	15.0	-1.12(0.02)
	<i>F110W</i>		<i>F110W</i> → <i>B</i>
164.050	24.50(0.07)	4.0	-1.68(0.05)
168.060	24.48(0.07)	5.6	-1.69(0.05)
	<i>F160W</i>		<i>F160W</i> → <i>R</i>
164.180	24.06(0.10)	4.0	-2.01(0.04)
169.050	24.05(0.10)	6.0	-2.00(0.03)
98.6000	flux:-0.06(0.04)	-23.3	—(—)

Table 2—Continued

Date ^a	Vega Mag	Epoch(rest)	K-Corr
2003aj ($z = 1.307$)			
	<i>F775W</i>		<i>F775W</i> → <i>U</i>
52673.1	26.62(0.10)	1.7	-0.05(0.08)
	<i>F850LP</i>		<i>F850LP</i> → <i>B</i>
52673.2	25.31(0.08)	1.7	-1.25(0.03)
52680.2	25.53(0.06)	4.8	-1.21(0.03)
52694.5	26.38(0.16)	11.0	-1.16(0.05)
	<i>F110W</i>		<i>F110W</i> → <i>V</i>
52684.2	25.13(0.11)	6.5	-1.49(0.06)
	<i>F160W</i>		<i>F160W</i> → <i>R</i>
52685.1	24.69(0.12)	6.9	-1.83(0.04)
52627.4	flux:0.062(0.03)	-18.0	—(—)
2002fx ($z = 1.400$)			
	<i>F775W</i>		<i>F775W</i> → <i>U</i>
52495.0	28.02(1.00)	-14.2	0.008(0.07)
52537.8	27.12(0.25)	3.6	0.300(0.10)
52580.0	29.02(1.00)	21.2	0.812(0.05)
	<i>F850LP</i>		<i>F850LP</i> → <i>B</i>
52537.8	25.21(0.07)	3.6	-1.20(0.09)
52580.5	27.10(0.27)	21.4	-0.82(0.08)
52490.3	flux:0.016(0.03)	-16.1	—(—)
2003eq ($z = 0.84$)			
	<i>F606W</i>		<i>F606W</i> → <i>U</i>
52783.7	24.58(0.01)	0.8	0.707(0.05)
	<i>F775W</i>		<i>F775W</i> → <i>B</i>
52783.7	23.22(0.01)	0.8	-1.18(0.03)
52799.1	23.67(0.02)	9.2	-1.14(0.02)
52807.3	24.15(0.04)	13.6	-1.12(0.04)
52819.8	25.05(0.07)	20.4	-1.02(0.06)
52838.3	26.22(0.30)	30.5	-0.97(0.02)
	<i>F850LP</i>		<i>F850LP</i> → <i>V</i>
52783.7	23.12(0.01)	0.8	-1.27(0.02)
52792.1	23.28(0.03)	5.4	-1.22(0.07)
52799.1	23.45(0.02)	9.2	-1.16(0.05)
52807.3	23.64(0.07)	13.6	-1.10(0.09)
52819.8	24.30(0.10)	20.4	-0.89(0.08)
52838.3	25.34(0.12)	30.5	-0.69(0.02)
	<i>F110W</i>		<i>F110W</i> → <i>R</i>
52792.9	23.20(0.10)	5.8	-1.22(0.01)
52735.5	flux:0.087(0.10)	-25.3	—(—)
2003es ($z = 0.954$)			

Table 2—Continued

Date ^a	Vega Mag	Epoch(rest)	K-Corr
	<i>F775W</i>		<i>F775W</i> → <i>U</i>
52784.5	24.12(0.03)	8.0	-0.87(0.05)
	<i>F850LP</i>		<i>F850LP</i> → <i>B</i>
52784.5	23.73(0.02)	8.0	-1.33(0.03)
52792.4	24.09(0.06)	12.0	-1.36(0.06)
52801.3	24.68(0.06)	16.6	-1.42(0.07)
52807.9	24.98(0.09)	19.9	-1.49(0.06)
52821.0	25.63(0.14)	26.6	-1.56(0.01)
52838.1	25.96(0.24)	35.4	-1.58(0.02)
	<i>F110W</i>		<i>F110W</i> → <i>V</i>
52792.8	24.20(0.08)	12.2	-1.28(0.05)
52734.6	flux:0.005(0.04)	-17.5	—(—)
2003az ($z = 1.265$)			
	<i>F775W</i>		<i>F775W</i> → <i>U</i>
52690.9	25.10(0.05)	3.0	-0.15(0.06)
52701.2	25.46(0.05)	7.5	-0.09(0.05)
	<i>F850LP</i>		<i>F850LP</i> → <i>B</i>
52690.9	24.36(0.04)	3.0	-1.40(0.03)
52701.2	24.48(0.04)	7.5	-1.37(0.02)
52709.1	24.64(0.05)	11.0	-1.35(0.03)
52716.9	25.09(0.06)	14.4	-1.32(0.05)
52726.5	25.52(0.08)	18.7	-1.25(0.08)
52733.2	25.75(0.09)	21.6	-1.17(0.07)
	<i>F110W</i>		<i>F110W</i> → <i>V</i>
52703.6	24.10(0.06)	8.6	-1.51(0.06)
52710.6	24.25(0.06)	11.7	-1.46(0.07)
52642.2	flux:0.054(0.03)	-18.4	—(—)
2002kc ($z = 0.216$)			
	<i>F606W</i>		<i>F606W</i> → <i>V</i>
52629.6	22.30(0.01)	-7.4	-0.23(0.05)
52672.3	23.28(0.01)	27.6	0.222(0.02)
	<i>F775W</i>		<i>F775W</i> → <i>R</i>
52629.6	21.81(0.02)	-7.4	-0.43(0.01)
52642.5	21.35(0.10)	3.1	-0.47(0.04)
52672.3	22.11(0.01)	27.6	-0.43(0.01)
	<i>F850LP</i>		<i>F850LP</i> → <i>I</i>
52629.7	21.70(0.01)	-7.4	-0.45(0.01)
52672.3	21.87(0.01)	27.6	-0.19(0.07)
2003eb ($z = 0.90$)			
	<i>F606W</i>		<i>F606W</i> → <i>U</i>
52734.6	24.26(0.02)	-1.1	0.824(0.07)

Table 2—Continued

Date ^a	Vega Mag	Epoch(rest)	K-Corr
52783.5	27.07(0.15)	24.5	1.233(0.02)
	<i>F775W</i>		<i>F775W</i> → <i>B</i>
52734.6	23.05(0.02)	-1.1	-1.14(0.05)
52745.6	23.15(0.02)	4.5	-1.10(0.03)
52783.5	25.22(0.06)	24.5	-0.83(0.02)
52799.1	25.92(0.10)	32.7	-0.80(0.03)
	<i>F850LP</i>		<i>F850LP</i> → <i>V</i>
52734.7	22.83(0.01)	-1.1	-1.32(0.01)
52745.7	22.84(0.01)	4.6	-1.27(0.09)
52751.2	22.98(0.01)	7.5	-1.20(0.06)
52763.6	23.47(0.01)	14.0	-1.09(0.14)
52774.0	24.02(0.04)	19.5	-0.92(0.13)
52783.6	24.39(0.04)	24.5	-0.75(0.10)
52792.1	24.77(0.11)	29.0	-0.60(0.03)
52792.4	24.63(0.08)	29.2	-0.60(0.03)
52799.1	25.06(0.15)	32.7	-0.55(0.02)
52801.3	24.84(0.06)	33.9	-0.56(0.04)
52807.9	25.03(0.10)	37.3	-0.61(0.02)
52821.0	25.40(0.09)	44.2	-0.63(0.02)
52838.1	25.36(0.10)	53.2	-0.69(0.05)
52692.5	flux:0.058(0.05)	-23.3	—(—)
2003XX ($z = 0.935$)			
	<i>F606W</i>		<i>F606W</i> → <i>U</i>
52733.6	25.17(0.05)	5.7	1.042(0.09)
	<i>F775W</i>		<i>F775W</i> → <i>B</i>
52733.6	23.57(0.05)	5.7	-1.08(0.02)
52745.6	24.12(0.05)	11.9	-1.05(0.04)
52783.5	26.40(0.25)	31.5	-0.77(0.02)
	<i>F850LP</i>		<i>F850LP</i> → <i>V</i>
52692.5	26.20(0.13)	-15.4	-1.12(0.06)
52733.7	23.26(0.01)	5.7	-1.27(0.10)
52745.7	23.63(0.01)	11.9	-1.14(0.10)
52751.2	23.88(0.02)	14.8	-1.07(0.15)
52763.6	24.56(0.04)	21.2	-0.77(0.11)
52774.0	24.87(0.05)	26.6	-0.58(0.05)
52783.6	25.20(0.06)	31.5	-0.48(0.02)
52792.1	25.36(0.13)	35.9	-0.50(0.05)
52799.1	26.04(0.20)	39.5	-0.53(0.04)
52807.3	26.45(0.19)	43.8	-0.56(0.02)
2002hr ($z = 0.526$)			
	<i>F606W</i>		<i>F606W</i> → <i>U</i>

Table 2—Continued

Date ^a	Vega Mag	Epoch(rest)	K-Corr
52579.6	24.04(0.03)	-6.4	0.103(0.08)
52629.5	25.82(0.15)	26.2	-0.36(0.03)
52674.1	27.43(0.30)	55.5	-0.35(0.07)
	<i>F775W</i>		<i>F775W</i> → <i>B</i>
52579.6	23.56(0.03)	-6.4	-0.84(0.01)
52589.7	23.20(0.12)	0.1	-0.87(0.05)
52590.0	23.28(0.11)	0.3	-0.87(0.05)
52596.6	23.44(0.14)	4.7	-0.93(0.09)
52614.5	23.91(0.08)	16.4	-1.27(0.18)
52629.5	24.42(0.05)	26.2	-1.66(0.03)
52674.1	25.67(0.10)	55.5	-1.58(0.02)
	<i>F850LP</i>		<i>F850LP</i> → <i>V</i>
52579.7	23.38(0.02)	-6.3	-0.96(0.05)
52629.5	23.76(0.03)	26.2	-1.18(0.04)
52674.1	25.04(0.10)	55.5	-1.14(0.02)
2003bd ($z = 0.67$)			
	<i>F606W</i>		<i>F606W</i> → <i>U</i>
52691.9	24.57(0.04)	8.1	0.162(0.02)
52735.4	27.50(0.12)	34.1	0.170(0.02)
	<i>F775W</i>		<i>F775W</i> → <i>B</i>
52691.9	23.41(0.03)	8.1	-1.05(0.02)
52735.4	25.77(0.10)	34.1	-1.24(0.02)
52745.6	26.05(0.10)	40.2	-1.25(0.01)
	<i>F850LP</i>		<i>F850LP</i> → <i>V</i>
52692.0	23.18(0.01)	8.1	-1.07(0.01)
52735.5	24.82(0.08)	34.2	-1.02(0.01)
52745.7	25.14(0.08)	40.3	-1.02(0.01)
52751.2	25.21(0.09)	43.6	-1.02(0.01)
52763.6	25.47(0.14)	51.0	-1.03(0.01)
52774.0	25.56(0.19)	57.2	-1.04(0.01)
52792.1	25.96(0.21)	68.1	-1.04(0.01)
52807.3	25.85(0.26)	77.2	-1.04(0.01)
52819.8	25.88(0.27)	84.6	-1.04(0.01)
52838.3	26.57(0.31)	95.7	-1.04(0.01)
52642.6	flux:0.057(0.03)	-21.4	—(—)
2002kd ($z = 0.735$)			
	<i>F606W</i>		<i>F606W</i> → <i>U</i>
52629.4	24.96(0.03)	-8.9	0.335(0.01)
52673.5	25.81(0.05)	16.4	0.335(0.03)
	<i>F775W</i>		<i>F775W</i> → <i>B</i>
52629.4	23.78(0.02)	-8.9	-1.06(0.04)

Table 2—Continued

Date ^a	Vega Mag	Epoch(rest)	K-Corr
52644.5	22.96(0.17)	-0.2	-1.10(0.03)
52645.5	22.76(0.10)	0.3	-1.10(0.03)
52673.5	24.18(0.05)	16.4	-1.11(0.02)
	<i>F850LP</i>		<i>F850LP</i> → <i>V</i>
52629.5	23.76(0.02)	-8.8	-1.10(0.01)
52639.4	23.09(0.01)	-3.1	-1.12(0.03)
52673.7	23.68(0.02)	16.5	-1.00(0.05)
2003be ($z = 0.640$)			
	<i>F606W</i>		<i>F606W</i> → <i>U</i>
52692.0	24.47(0.03)	12.1	0.096(0.03)
52732.5	27.26(0.20)	36.8	0.086(0.03)
	<i>F775W</i>		<i>F775W</i> → <i>B</i>
52641.3	28.02(0.80)	-18.7	-0.68(0.12)
52692.0	23.45(0.03)	12.1	-1.04(0.06)
52732.5	25.50(0.10)	36.8	-1.29(0.02)
52784.3	26.09(0.10)	68.4	-1.22(0.02)
	<i>F850LP</i>		<i>F850LP</i> → <i>V</i>
52692.1	23.04(0.01)	12.2	-1.07(0.01)
52732.5	24.45(0.05)	36.8	-1.08(0.01)
52784.4	25.31(0.13)	68.4	-1.07(0.01)
52641.3	flux:0.087(0.10)	-18.7	—(—)
2003dy ($z = 1.34$)			
	<i>F850LP</i>		<i>F850LP</i> → <i>U</i>
52733.7	24.45(0.04)	-0.1	-0.96(0.09)
52745.7	24.67(0.06)	4.9	-1.05(0.05)
52751.2	24.77(0.08)	7.3	-1.09(0.04)
52763.6	25.29(0.11)	12.6	-1.16(0.04)
52774.0	25.57(0.15)	17.0	-1.21(0.01)
52783.6	26.62(0.45)	21.1	-1.22(0.02)
52801.3	26.65(0.26)	28.7	-1.27(0.03)
	<i>F110W</i>		<i>F110W</i> → <i>B</i>
52751.6	24.28(0.07)	7.4	-1.73(0.05)
52754.6	24.38(0.08)	8.7	-1.74(0.05)
	<i>F160W</i>		<i>F160W</i> → <i>R</i>
52751.7	23.81(0.08)	7.5	-1.89(0.01)
52692.4	flux:0.037(0.04)	-17.8	—(—)
2002ki ($z = 1.14$)			
	<i>F775W</i>		<i>F775W</i> → <i>U</i>
52600.8	24.79(0.10)	-0.6	-0.46(0.01)
52643.6	26.82(0.17)	19.3	-0.46(0.01)
	<i>F850LP</i>		<i>F850LP</i> → <i>B</i>

Table 2—Continued

Date ^a	Vega Mag	Epoch(rest)	K-Corr
52600.8	23.89(0.04)	-0.6	-1.48(0.02)
52643.6	25.80(0.10)	19.3	-1.36(0.05)
52652.2	25.99(0.10)	23.3	-1.32(0.02)
52663.7	26.89(0.20)	28.7	-1.32(0.02)
	<i>F160W</i>		<i>F160W</i> → <i>I</i>
52652.4	24.68(0.25)	23.4	-1.65(0.03)
52664.5	24.87(0.25)	29.1	-1.55(0.07)
2003ak ($z = 1.551$)			
	<i>F850LP</i>		<i>F850LP</i> → <i>U</i>
52673.2	25.68(0.14)	5.0	-0.68(0.03)
52680.2	25.95(0.10)	7.7	-0.67(0.03)
52694.5	26.62(0.21)	13.3	-0.63(0.03)
	<i>F110W</i>		<i>F110W</i> → <i>B</i>
52681.1	25.03(0.10)	8.1	-1.71(0.03)
52693.0	25.03(0.10)	12.8	-1.74(0.05)
52708.5	25.38(0.15)	18.8	-1.82(0.07)
52715.4	25.80(0.15)	21.5	-1.87(0.04)
	<i>F160W</i>		<i>F160W</i> → <i>V</i>
52681.3	24.01(0.05)	8.2	-2.29(0.03)
52693.4	24.21(0.07)	12.9	-2.25(0.03)
52701.6	24.61(0.08)	16.1	-2.26(0.11)
52627.4	flux:0.050(0.03)	-12.9	—(—)
2002hp ($z = 1.305$)			
	<i>F775W</i>		<i>F775W</i> → <i>U</i>
52579.5	25.52(0.10)	3.3	-0.03(0.07)
	<i>F850LP</i>		<i>F850LP</i> → <i>B</i>
52537.1	26.83(0.39)	-15.0	-1.47(0.06)
52579.5	24.32(0.04)	3.3	-1.27(0.05)
52589.1	24.89(0.06)	7.4	-1.23(0.03)
52595.4	25.06(0.08)	10.1	-1.22(0.03)
52603.8	25.67(0.08)	13.8	-1.19(0.05)
52613.8	26.09(0.14)	18.1	-1.10(0.09)
52629.3	26.60(0.17)	24.9	-1.00(0.03)
52639.4	27.30(0.35)	29.2	-0.99(0.04)
	<i>F110W</i>		<i>F110W</i> → <i>V</i>
52589.2	24.28(0.07)	7.5	-1.52(0.06)
52595.5	24.33(0.07)	10.2	-1.46(0.06)
2002fw ($z = 1.30$)			
	<i>F775W</i>		<i>F775W</i> → <i>U</i>
52536.8	25.37(0.05)	-5.8	-0.22(0.04)
52548.3	25.01(0.08)	-0.8	-0.14(0.07)

Table 2—Continued

Date ^a	Vega Mag	Epoch(rest)	K-Corr
52578.4	26.45(0.10) <i>F850LP</i>	12.2	0.111(0.08) <i>F850LP</i> → <i>B</i>
52536.9	24.49(0.05)	-5.8	-1.40(0.02)
52548.3	24.17(0.04)	-0.8	-1.40(0.07)
52552.5	24.44(0.06)	0.9	-1.40(0.07)
52557.4	24.36(0.05)	3.1	-1.36(0.05)
52567.9	24.48(0.06)	7.6	-1.33(0.02)
52577.5	24.85(0.07)	11.8	-1.31(0.04)
52578.5	25.07(0.07)	12.2	-1.30(0.05)
52595.5	25.88(0.17)	19.6	-1.17(0.08)
52603.8	26.68(0.25) <i>F110W</i>	23.2	-1.07(0.03) <i>F110W</i> → <i>V</i>
52549.5	23.96(0.08)	-0.3	-1.67(0.04)
52557.6	24.11(0.08) <i>F160W</i>	3.1	-1.64(0.07) <i>F160W</i> → <i>R</i>
52549.8	23.83(0.08)	-0.2	-1.92(0.09)
52557.8	23.76(0.09)	3.2	-1.85(0.07)
2002dc ($z = 0.475$)			
	<i>F775W</i>		<i>F775W</i> → <i>B</i>
52405.4	22.41(0.02)	-0.0	-0.78(0.05)
52438.0	23.57(0.03)	22.0	-1.66(0.13)
52449.3	24.07(0.05) <i>F850LP</i>	29.7	-1.78(0.02) <i>F850LP</i> → <i>V</i>
52415.2	22.38(0.02)	6.6	-0.89(0.06)
52438.1	23.23(0.03)	22.1	-1.02(0.08)
52449.4	23.51(0.06)	29.7	-1.14(0.04)
52455.2	23.85(0.05)	33.7	-1.15(0.05)
52600.0	27.54(0.65)	131.8	-0.94(0.01)
2002dd ($z = 0.95$)			
	<i>F775W</i>		<i>F775W</i> → <i>U</i>
52405.4	23.66(0.02)	0.8	-0.66(0.12)
52438.0	24.99(0.06)	17.5	-0.98(0.01)
52449.3	25.51(0.09) <i>F850LP</i>	23.3	-1.01(0.03) <i>F850LP</i> → <i>B</i>
52405.4	23.24(0.05)	0.8	-1.27(0.05)
52415.2	23.45(0.02)	5.8	-1.31(0.02)
52438.1	24.34(0.08)	17.6	-1.44(0.08)
52449.4	24.85(0.12)	23.4	-1.56(0.02)
52455.2	24.96(0.09) <i>F110W</i>	26.3	-1.58(0.01) <i>F110W</i> → <i>V</i>
52438.0	23.98(0.05)	17.5	-1.27(0.03)

3. Distance Fitting and Cosmology Constraints

Distance estimates from SN Ia light curves are derived from the luminosity distance,

$$d_L = \left(\frac{\mathcal{L}}{4\pi\mathcal{F}} \right)^{\frac{1}{2}}, \quad (4)$$

where \mathcal{L} and \mathcal{F} are the intrinsic luminosity and the absorption-free flux of the SN within a given passband, respectively. Equivalently, logarithmic measures of the flux (apparent magnitude, m), luminosity (absolute magnitude, M), and colors (to quantify the selective absorption) were used to derive extinction-corrected distance moduli, $\mu_0 = m - M = 5 \log d_L + 25$ (d_L in units of megaparsecs). In this context, the luminosity is a “nuisance parameter” whose fiducial value vanishes from a reconstruction of the expansion history (which makes use of differences in distance with redshift). We have adopted the MLCS2k2 method (Riess, Press, & Kirshner 1996; Jha 2002) used by R04 and the data described in §2 to derive accurate and individual *relative* distance moduli for the sets of SNe described in §3 and given in Table 6¹⁶. As in Riess, Press, & Kirshner (1996), we require for robust fits of light curves that SN photometry commence no less than 10 days after maximum, although in practice degeneracies in light curve fits for late-commencing SN Ia photometry are also alleviated by flux limits from the preceding epoch (typically 3 weeks earlier than the discovery point in the restframe).

¹⁶Although a new version of the MLCS2k2 algorithm is currently under development with an expanded training set (Jha, Riess, & Kirshner 2006), we utilized the same version used by R04 to maintain, as far as possible, a consistent and tested process to measure all available SN Ia data. However, tests comparing the R04 and Jha et al. (2006) versions of the algorithm show very good agreement when applied to high quality data (Lampeitl 2006). In addition we have found and corrected a minor numerical error in our calculation of K -corrections which affect a few SNe Ia at the few percent level. In the future, it will be valuable to reanalyze all available data consistently with continually improving algorithms and we will attempt to provide updated distance estimates using updated versions of data and algorithms at <http://braeburn.pha.jhu.edu/~ariess/R06> or upon request to ariess@stsci.edu.

Table 2—Continued

Date ^a	Vega Mag	Epoch(rest)	K-Corr
-------------------	----------	-------------	--------

^aJD–2,400,000.
 Uncertainties in magnitudes are listed in parentheses.

Table 3. Spectroscopic Data

SN	MJD(age)	Instrument	z
HST04Pat	53205.1(+3)	<i>HST</i> ACS	0.97 ^{a,1}
HST04Cay	53254.9	<i>HST</i> ACS	? ²
HST04Mcg	53275.6(+10)	<i>HST</i> ACS	1.357 ^{c,1}
HST05Fer	53486.8(+10)	<i>HST</i> ACS	1.02 ^{a,1}
HST05Koe	53486.8(+15)	<i>HST</i> ACS	1.23 ^{a,1}
HST05Dic	—	—	0.638 ^{b,3}
HST04Gre	53275.6(+6)	<i>HST</i> ACS	1.14 ^{a,1}
HST04Omb	53373.7(+3)	<i>HST</i> ACS	0.975 ^{a,d,1}
HST05Red	53436.6	<i>HST</i> ACS	1.189 ^{b,2}
HST05Lan	53436.6(+2)	<i>HST</i> ACS	1.235 ^{c,1}
HST04Tha	53207.7(+15)	<i>HST</i> ACS	0.954 ^{a,d,1}
HST04Rak	53373.7(+12)	<i>HST</i> ACS	0.739 ^{c,1}
HST05Zwi	53415.9(+5)	<i>HST</i> ACS	0.521 ^{a,d,1}
HST04Haw	—	—	0.490 ^{d,3}
HST04Kur	53366.1(+3)	<i>HST</i> ACS	0.359 ^{c,1}
HST04Yow	53157.0(+17)	<i>HST</i> ACS	0.457 ^{a,d,1}
HST04Man	53157.0(+5)	<i>HST</i> ACS	0.854 ^{a,d,1}
HST05Spo	53436.6(+20)	<i>HST</i> ACS	0.839 ^{a,d,1}
HST04Eag	53296.9(+2)	<i>HST</i> ACS	1.019 ^{c,1}
HST05Gab	53485.7(-1)	<i>HST</i> ACS	1.12 ^{a,1}
HST05Stro	53485.7(+5)	<i>HST</i> ACS	1.027 ^{a,d,1}
HST04Sas	53156.2(+1)	<i>HST</i> ACS	1.39 ^{a,1}

^aFrom cross-correlation with broad SN features.

^bFrom narrow features in our own additional Keck host-galaxy spectrum.

^cFrom both (a) and (b).

^dFrom Team Keck.

¹Classified as SN Ia with high confidence from spectrum.

²Photometric properties indicate likely (but not certain) SN Ia.

In Figure 6 we show the Hubble diagram of distance moduli and redshifts for all of the *HST*-discovered SNe Ia in the Gold and Silver sets from our program. The new SNe Ia span a wide range of redshift ($0.21 < z < 1.55$), but their most valuable contribution to the SN Ia Hubble diagram remains in the highest-redshift region where they now well delineate the range at $z \geq 1$ with 23 SNe Ia, 13 new objects since R04. This territory remains uniquely accessible to *HST*, which has discovered the dozen highest-redshift SNe Ia known, and its exploration is the focus of the rest of this paper.

In the inset to Figure 6 we show the residual Hubble diagram (from an empty Universe) with the Gold data uniformly binned. Here and elsewhere, we will utilize uniform, unbiased binning achieved with a fixed value of $n\Delta z$, where Δz is the bin width in redshift and n is the number of SNe in the bin.¹⁷ In Figure 6 we use $n\Delta z = 6$ which yields seven bins for our sample. Although binning is for illustrative purposes in the Hubble diagram, there are some specific advantages of binning such as the removal of lensing-induced asymmetrical residuals by flux averaging (Wang 2005) and the ease of accounting for systematic uncertainties introduced by zeropoint errors in sets of photometric passbands used at similar redshifts.

The distance-redshift relation of SNe Ia is one of few powerful tools available in observational cosmology. A number of different hypotheses and models can be tested with it, including kinematic descriptions of the expansion history of the Universe, the existence of mass-energy terms on the right-hand side of the Friedman equation, and the presence of astrophysical sources of contamination. Testing all interesting hypotheses is well beyond the scope of this paper and is best left for future work. Instead, we now undertake a few narrowly posed investigations.

For the following analyses we limit the low-redshift boundary of our sample to $cz > 7000$ km s⁻¹ to avoid the influence of a possible local, "Hubble Bubble" (Jha 2002, Zehavi et al. 1998). The Gold sample above this velocity boundary consists of 182 supernovae.

3.1. Kinematics and Model-Independent Observables

The distance-redshift relation of SNe Ia contains a cumulative record of changes in the cosmic expansion rate, $H(z)$, over the last 10 Gyr, described in flat space as given in equation 3. Although the interesting kinematic information, $H(z)$, appears to be degraded by the physical integration across its temporal variations, good sampling of SNe Ia over a wide range of redshifts allows us to recover its value at discrete, uncorrelated epochs,

¹⁷The last bin ends abruptly with the highest-redshift SN; thus, its $n\Delta z \leq$ value is smaller than the rest.

independent of the cosmological model. Such information may be more general and of longer-lasting value than constraints on any single, specific model of dark energy.

Following Wang & Tegmark (2005; see also Daly & Djorgovski 2004), we transform the Gold sample of luminosity distances to comoving coordinate distances, $r(z)$, as

$$r(z) = \frac{1}{2997.9(1+z)} 10^{\mu_0/5-5}. \quad (5)$$

We assume spatial flatness (as motivated by theoretical considerations, i.e., that most inflation models predict $\Omega_K < 10^{-5}$ or by similar resolutions to the “flatness problem”) for ease of calculations, but the following approach can be generalized to allow for nontrivial spatial curvature. After sorting the SNe Ia by redshift, we define the quantity

$$x_i = \frac{r_{i+1} - r_i}{z_{i+1} - z_i}, \quad (6)$$

where the mean value of x_i gives an unbiased estimate of the inverse of $H(z)$ at the redshift, z_i . As in Wang & Tegmark (2005), we flux average the data first ($n\Delta z \approx 1$) to remove possible lensing bias. We then calculate the minimum-variance values of $H(z)$ in 3, 4, or 5 even-sized bins across the sample, with $n\Delta z$ chosen to be 40, 20, or 15, respectively, to achieve the desired number of bins.

In the upper panel of Figure 7 we show sets of 3, 4, or 5 samplings of $H(z)$ versus redshift from the Gold sample. As seen, $H(z)$ remains well constrained until $z \approx 1.3$, beyond which the SN sample is too sparse to usefully determine $H(z)$. For comparison, we show the dynamical model of $H(z)$ derived from $H(z)^2 = H_0^2(\Omega_M(1+z)^3 + \Omega_\Lambda)$ with “concordance” values of $\Omega_M = 0.29$ and $\Omega_\Lambda = 0.71$.

In the lower panel of Figure 7 we show the kinematic quantity $\dot{a} = H(z)/(1+z)$ versus redshift. In the uncorrelated \dot{a} versus redshift space, it is very easy to evaluate the sign of the change in expansion rate independent of the cosmological model. For comparison we show three simple kinematic models: purely accelerating, decelerating, and coasting, with $q(z) \equiv (-\ddot{a}/a)/H^2(z) = d(H^{-1}(z))/dt - 1 = 0.5, -0.5, \text{ and } 0.0$, respectively. We also show a model with recent acceleration ($q_0 = -0.6$) and previous deceleration $dq/dz = 1.2$, where $q(z) = q_0 + zdq/dz$, which is a good fit to the data.

In Figure 8 we demonstrate the improvement in the measure of $H(z)$ at $z > 1$ realized from the addition of the new SNe Ia, presented here, to the sample from R04: we have reduced the uncertainty of $H(z)$ at $z > 1$ from just over 50% to just under 20%.¹⁸

¹⁸Monte Carlo simulations of the determination of uncorrelated components of $H(z)$ show that the increase

We also repeated the analysis of R04 in which the deceleration parameter, $q(z) \equiv (-\ddot{a}/a)/H^2(z) = d(H^{-1}(z))/dt - 1$, is parameterized by $q(z) = q_0 + zdq/dz$ and determined from the data and Eq. (5). As in R04, we find that the Gold set strongly favors a Universe with recent acceleration ($q_0 < 0$) and previous deceleration ($dq/dz > 0$) with 99.96% and 99.999% likelihood (summed within this quadrant), respectively. Summing the probability density in the q_0 vs. dq/dz plane along lines of constant transition redshift, $z_t = -q_0/(dq/dz)$, yields the transition redshift of $z_t = 0.43 \pm 0.07$.

However, as shown by Shapiro & Turner (2005), different parameterizations of $q(z)$ can lead to different redshifts for the transition and to different confidence levels for the epochs of acceleration and deceleration (though all appear sufficiently high to yield a robust conclusion similar to our own; see also Daly & Djorgovski 2004). Thus, our uncertainty is only statistical within a linear form for $q(z)$, and is not useful for comparing to the transition expected for a cosmological constant ($z_t \approx 0.7$) due to the different functional forms used for evaluating the redshift at which $\ddot{a} = 0$.

3.2. Alternatives to Dark Energy

After the detection of the apparent acceleration of cosmic expansion (and dark energy) by Riess et al. (1998) and Perlmutter et al. (1999), alternative hypotheses for the apparent faintness of high-redshift SNe Ia were posed. These included extragalactic gray dust with negligible tell-tale reddening or additional dispersion (Aguirre 1999a,b; Rana 1979, 1980), and pure luminosity evolution (Drell, Lored, & Wasserman 2000).

As reported elsewhere, there is considerable evidence against these possibilities and little evidence in favor of either of them (Riess et al. 1998; Perlmutter et al. 1999; Riess et al. 2001; Leibundgut 2001; Sullivan et al. 2003; Knop et al. 2003; Filippenko 2004, 2005). However, it is important to remain vigilant for such possibilities. The redshift range $z > 1$, where deceleration dominates over acceleration for the simplest cosmological models, is crucial for breaking degeneracies between astrophysical effects and cosmological effects (e.g., Riess et al. 2001).

In R04 we found that the first significant sample of SNe Ia at $z > 1$ from *HST* rejected with high confidence the simplest model of gray dust by Goobar, Bergstrom, & Mörtzell (2002), in which a smooth background of dust is present (presumably ejected from galaxies)

in precision proceeds as approximately $n^{2/3}$, significantly faster than $n^{1/2}$, where n is the number of SNe due to the rate of increase in unique pairs of SNe.

at a redshift greater than the SN sample (i.e., $z > 2$) and diluted as the Universe expands. This model and its opacity was invented to match the 1998 evidence for dimming of supernovae at $z \sim 0.5$ without invoking dark energy in a universe with $\Omega_m = 1$. This model is shown in the inset of Figure 6. The present Gold sample (at the best fitting value of H_0) rejects this model at even higher confidence ($\Delta\chi^2 = 194$, i.e., 14σ , see Table 4), beyond a level worthy of further consideration.

However, a more pernicious kind of dust was also suggested by Goobar, Bergstrom, & Mörtzell (2002), a “replenishing dust” in which a constant density of gray dust is continually replenished at just the rate it is diluted by the expanding Universe. This latter dust is virtually indistinguishable from an Ω_Λ model (see Table 4) via the magnitude-redshift relation because the dimming is directly proportional to distance traveled and thus mathematically similar to the effects of a cosmological constant. Dust of this sort with the required opacity, replenishing rate, and ejection velocity from galaxies ($> 1000 \text{ km s}^{-1}$ for it to fill space uniformly without adding detectable dispersion) may always be virtually undetectable in the Hubble diagram of SNe Ia, but its degree of fine tuning makes it unattractive as a simple alternative to a cosmological constant.

More recently, Östman & Mörtzell (2005) used 11,694 quasars from the Sloan Digital Sky Survey (SDSS), at $0.1 < z < 2$, to limit the dimming of SNe Ia at $z = 1$ by Milky Way dust to less than 0.03 mag, and by very gray dust ($R_V = 12$) to less than 0.1 mag, for either the high- z dust or replenishing dust models. Petric et al. (2006) has ruled out the presence of intergalactic gray dust at a level of $\Omega_{dust} \leq 10^{-6}$ by the lack of an X-ray scattering halo around a quasar at $z = 4.3$, limiting dimming due to micron-sized grains to less than a few percent (less than a percent to $z \sim 0.5$) and this dust scenario has also been limited by the resolution of the far infrared background (Aguirre & Haiman 2000)

We also find, as in R04 but with even greater confidence, that the data are inconsistent ($\Delta\chi^2 = 116$) with the simplest SN luminosity evolution (proportional to redshift) in lieu of a cosmological constant; see inset of Figure 6 and Table 4.

Less direct but significant failures to detect SN evolution come from detailed comparisons of the composite state of the abundance, temperature, and outward velocity of the SN photosphere as recorded through the spectra (Sullivan 2005, Blondin et al. 2006, Hook et al. 2005, Balland et al. 2006). Greater leverage for this test can be gained by extending the redshift range of the observed SED using the present sample. In Figure 16 we show the average, composite spectrum of the 13 best-observed SNe Ia at $z \geq 1$. For the spectra listed in Table 3 (and from R04), we transformed to the rest frame and calculated a 3σ -clipped average at each wavelength point. Shown are the mean and dispersion about the mean. For comparison, we used the template spectra from Nugent et al. (2002) (with

colors matched to the MLCS empirical model) averaged over the week following maximum light. As shown, the high-redshift composite, with a mean redshift of 1.2, bears a striking resemblance to the model of a post-maximum SN Ia. Two specific indications of SNe Ia are seen in the Si feature at 4130 Å and the width of the Ca II and Si II blended feature at 3750 Å which indicates the presence of both ions. We put less reliance on the region redward of 4300 Å corresponding to redward of observed 9500 Å because 1) the quantum efficiency of the detector is rapidly decaying and thus harder to calibrate and 2) modest color differences may exist between the spectral template and the mean of these objects (due to intrinsic variation or reddening).

We find no evidence for a difference in the mean SED of SNe Ia across 10 Gyr of look-back time or 1.2 units of redshift.

SNe Ia hosted by red, early-type hosts are expected to be particularly robust against absorption by dust (where the dust content is low) and may be expected to arise from the earliest forming progenitors (as compared to late-type hosts). Thus differences in distances measured to SNe Ia hosted by early and late-type hosts form an important probe of systematics (Sullivan et al. 2003). We find that the 6 SNe Ia we discovered at $z \geq 1$ with ACS residing in red, elliptical hosts (HST05Lan, 2002hp, HST04Sas, 2003es, HST04Tha, and 2003XX) all have low measured extinction ($A_V < 0.25$ mag) and the same dispersion and mean (closer for their redshift by 0.07 ± 0.10 mag) as the full sample, indicating that at $z > 1$ no differences are apparent for distances measured in early type hosts.

3.3. Dark Energy

Strong evidence suggests that high-redshift SNe Ia provide accurate distance measurements and that the source of the apparent acceleration they reveal lies in the negative pressure of a “dark energy” component. Proceeding from this conclusion, our hard-earned sample of SNe Ia at $z > 1.0$ can provide unique constraints on its properties. Strong motivation for this investigation comes from thorough studies of high-redshift and low-redshift SNe Ia, yielding a consensus that there is no evidence for evolution or intergalactic gray dust at or below the current statistical constraints on the average high-redshift apparent brightness of SN Ia (see Filippenko 2004, 2005 for recent reviews). We summarize the key findings here. (1) Empirically, analyses of SN Ia distances (after accounting for the light curve shape-luminosity relation) versus host stellar age, morphology or dust content (Riess et al. 1998, Sullivan et al. 2003, Jha, Riess, & Kirshner 2006), or metallicity or star formation rate (Gallagher et al. 2005, Riess et al. 1999) indicate that SN Ia distances are relatively indifferent to the evolution of the Universe. (2) Detailed

examinations of the distance-independent properties of SNe Ia (including the far-UV flux, e.g., as presented in the last section) provide strong evidence for uniformity across redshift and no indication (thus far) of redshift-dependent differences (e.g., Sullivan et al. 2005; Howell et al. 2005; Blondin et al. 2006). (3) SNe Ia are uniquely qualified as standard candles because a well understood, physical limit (the Chandrasekhar limit) provides the source of their homogeneity. Based on these studies, we adopt a limit on redshift-dependent systematics is to be 5% per $\Delta z = 1$ at $z > 0.1$ and make quantitative use of this in §4.1.

Many have studied the constraint placed by the redshift-magnitude relation of SNe Ia on the parameter combination Ω_M-w , where w (assumed to be constant) is the dark energy equation-of-state parameter. There are few models for dark energy that predict an equation of state that is *constant*, different from the cosmological constant, and not already ruled out by the data. On the other hand, a prominent class of models does exist whose defining feature is a time-dependent dark energy (i.e., quintessence). While the rejection of $w = -1$ for an assumed constant value of w would invalidate a cosmological constant, it is also possible that apparent consistency with $w = -1$ in such an analysis would incorrectly imply a cosmological constant. For example, if $w(z)$ is rising, declining, or even sinusoidal, a measured derivative could be inconsistent with zero while the average value remains near -1 . Therefore, when using $w(z)$ to discriminate between dark-energy models, it is important to allow for time-varying behavior, or else valuable information may be lost. Here, we seek to constrain the value of $w(z > 1)$ and bound its derivative across the range $0.2 < z < 1.3$. This is unique information afforded by the *HST*-discovered SN Ia sample.

Unfortunately, present dynamical dark-energy models in the literature (see Szydlowski, Kurek, & Krawiec 2006 for a review) do not suggest a universal or fundamental parametric form for $w(z)$. Instead, most models contain embedded, free-form functions (e.g., the shape of a scalar potential). Thus, we proceed with simple, empirical studies of variations in the equation-of-state parameter of dark energy.

The luminosity distance to SNe Ia, through the solution to the Freidman equation, is sensitive to $w(z)$:

$$d_l = cH_0^{-1}(1+z) \int_0^z \frac{dz'}{E(z')}, \quad (7)$$

Here, $E(z) \equiv \{\Omega_m(1+z')^3 + (1-\Omega_m) \times \exp[+3 \int_0^{\ln(1+z')} d \ln(1+z')(1+w(z'))]\}^{1/2}$, where Ω_m is the dimensionless matter density $8\pi\rho_m/(3H_0^2)$, H_0 is the Hubble constant (the present value of the Hubble parameter), and z is the redshift of any SN Ia.

We can determine the likelihood for parameters of $w(z)$ from a χ^2 statistic,

$$\chi^2(H_0, \Omega_M, \mathbf{w}_i) = \sum_i \frac{(\mu_{p,i}(z_i; H_0, \Omega_M, \mathbf{w}_i) - \mu_{0,i})^2}{\sigma_{\mu_{0,i}}^2 + \sigma_v^2}, \quad (8)$$

where σ_v is the dispersion in supernova redshift (transformed to units of distance moduli) due to peculiar velocities $\sigma_{\mu_{0,i}}$ is the uncertainty in the individual distance moduli, and \mathbf{w}_i is a set of dark-energy parameters describing $w(z)$. Due to the extreme redshift of our distant sample and the abundance of objects in the nearby sample, our analysis is insensitive to the value we assume for σ_v within its likely range of $200 \text{ km s}^{-1} \leq \sigma_v \leq 500 \text{ km s}^{-1}$. For our analysis we adopt $\sigma_v = 400 \text{ km s}^{-1}$. For high-redshift SNe Ia whose redshifts were determined from the broad features in the SN spectrum, we assume an uncertainty of $\sigma_v = 2500 \text{ km s}^{-1}$ in quadrature to the peculiar velocity term. Marginalizing our likelihood functions over the nuisance parameter, H_0 (by integrating the probability density $P \propto e^{-\chi^2/2}$ for all values of H_0), and the use of the described independent priors, yields the confidence intervals considered below.

Strong degeneracies exist in the effect of $w(z)$ and Ω_M on the expansion history, requiring independent constraints to make significant progress. Here we consider the use of one or more of the following constraints.

(1) *The SDSS luminous red galaxy, baryon acoustic oscillation (BAO) distance parameter to $z = 0.35$:* $A \equiv \Omega_M^{\frac{1}{2}} E(z)^{-1/3} [\frac{1}{z} \int_0^z \frac{dz}{E(z)}]^{\frac{2}{3}}$, where $z = 0.35$ and $A = 0.469(n/0.98)^{-0.35} \pm 0.017$ from Eisenstein et al. (2005). The 3-year Wilkinson Microwave Anisotropy Probe (WMAP) results yield $n = 0.95$ (Spergel et al. 2006).

(2) *The present local mass density:* $\Omega_M = 0.28 \pm 0.04$, a consensus value when combining large-scale structure (LSS) measurements from the 2dF and SDSS of $\Omega_M h$ (Tegmark et al. 2004; Cole et al. 2005) and the value of H_0 from *HST* Cepheids (Freedman et al. 2001; Riess et al. 2005).

(3) *The distance to last scattering, $z = 1089$:* In the H_0 -independent form (Bond, Efstathiou, & Tegmark 1997), $R_{CMB} \equiv \Omega_M^{\frac{1}{2}} \int_0^{1089} \frac{dz'}{E(z')}$ from the 3-year integrated WMAP analysis (Spergel et al. 2006), updated by Wang & Mukherjee (2006) to be 1.70 ± 0.03 independent of the dark-energy model.

(4) *The distance ratio from $z = 0.35$ to $z = 1089$:* Measured by the SDSS BAOs from Eisenstein et al. (2005), $R_{0.35} = \frac{0.35}{E(0.35)}^{(1/3)} [\int_0^{0.35} (dz/E(0.35))]^{(2/3)} / \int_0^{1089} dz/E(1089) = 0.0979 \pm 0.0036$.

Additional cosmological constraints exist, but in general provide less leverage and may be less robust than the above.

Unfortunately, constraints anchored at $z = 1089$ such as R_{CMB} and $R_{0.35}$ in (3) and (4) above require careful consideration when using continuous descriptions of $w(z)$. Specifically, we must consider how to evaluate integrals depending on $w(z)$ in a region where we have

no data and little intuition, i.e., between the highest-redshift SN Ia at $z \approx 1.8$ and the surface of last scattering at $z = 1089$. This span contributes significantly to R_{CMB} (and even more to $R_{0.35}$), accounting for approximately two-thirds of the total distance to last scattering. Constraints resulting from a naive leap across this present “cosmological desert” are likely to be unjustifiably strong, and extremely sensitive to our assumptions about the early behavior of dark energy or on our chosen, parametric form for $w(z)$ (as we will see).

To evaluate $w(z)$ as well as its sensitivity to assumptions about its high-redshift behavior, we will make use of three different priors. Our “weak” prior (the most conservative) will utilize only Ω_M and A which are determined at low redshifts, making no attempt to guess the behavior of dark energy in the span $1.8 < z < 1089$. Our “strong” constraint integrates the expressions containing $w(z)$ in R_{CMB} and $R_{0.35}$ between $z = 0$ and the highest-redshift SN ($z \approx 1.8$) and beyond; it assumes that the influence of dark energy on $H(z)$ is minimal by relaxing the equation-of-state parameter to $w = -1$ at $z > 1.8$. This “strong” prior strikes a balance between making maximal use of all information, but only broadly guesses at the importance of dark energy where there are no discrete data (i.e., by assuming that the high-redshift Universe is fully dark-matter dominated). Our “strongest” prior is the naive extension of $w(z)$ from $z = 1.8$ to $z = 1089$ strictly along its empirical or parametric description.

The minimum complexity required to detect time variation in dark energy is to add a second parameter to measure a change in the equation-of-state parameter with redshift. The expansion $w(z) = w_0 + w'z$, where $w' \equiv \frac{dw}{dz}|_{z=0}$ was proposed by Cooray & Huterer (1999), first used by Di Pietro & Claeskens (2003) and later by R04. However, in this form, $w(z)$ diverges, making it unsuitable at high redshift or requiring guesses as to the form of its graceful exit (Wang & Mukherjee 2006). Chevalier & Polarski (2001) and Linder (2003) suggest $w(z) = w_0 + w_a z / (1 + z)$, which solves the divergence problem but at a cost of demanding stiffer behavior for $w(z)$ than we may presume *a priori*. As we shall see, invoking the (w_0, w_a) parameterization can act like an additional, strong prior itself.

In Figure 9 we show the constraints on $w_0 - w_a$ plane for the three priors for the Gold sample. Here we focus on what is learned from the inclusion of the high-redshift SNe Ia from *HST*, both the new objects and those with improved calibration from R04.

The addition of SNe Ia at $z > 1$ with the weak prior provides valuable leverage in the $w_0 - w_a$ space, well in excess of their fractional contribution to the sample. Citing a popular metric, the area of the 95% confidence interval (Huterer & Turner 2001, Kolb et al. 2006; Albrecht & Bernstein 2006), we note a reduction by 40% or an increase in the figure of merit (inverse area) by a factor of 1.7 by the inclusion of the Gold-quality SNe Ia from *HST* with the weak prior. The reason is readily apparent; because the prior contains no

information regarding the evolution of dark energy, what little is gleaned comes exclusively from the discrete data. The highest-redshift SNe Ia are critical to breaking the degeneracy between w_0 and w_a affecting their lower-redshift brethren. Constraints measured using the parameterization, $w(z) = w_0 + w'z$ yield similar improvements, 50% in area, when the prior is weak. The best fit is consistent with a cosmological constant at $w_0 = -1$ and $w_a = 0$. However, the overall level of empirical knowledge about dark-energy evolution remains very modest. We may conclude that if dark energy evolves, the evolution is not very rapid (though it remains difficult to predict the natural level of expected evolution; see Caldwell & Linder 2005).

As our prior becomes more ambitious (maintaining the flatness prior), the confidence intervals rapidly shrink. For the strong and strongest prior, the 95% confidence interval is 1.5 and 4.4 times smaller than the weak prior, respectively. For the strongest prior, even modest values of w_a (and even more so for w') are strongly excluded because of their implication that dark energy would gradually and unhaltingly grow in importance with redshift to last scattering.¹⁹ For these priors, a cosmological constant (i.e., $w_0 = -1$, $w_a = 0$) is separated from the best fit along the direction of the major axis of the error ellipse, lying within the boundary of the *joint* 1σ to 2σ confidence level. However, it appears that the gains from the stronger priors come at a cost of reliance on the merit of our prior at high redshifts and with diminished regard for the data sampling $w(z)$ at lower redshifts.

We now explore the sensitivity of the constraints on $w(z)$ to the assumption that it can be described by a simple, parametric form. To do so we compare the constraints on $w(z)$ derived from the previous $w(z) = w_0 + w_a z / (1 + z)$ to a higher-order polynomial expansion in powers of $\ln(1 + z)$ which assumes little about $w(z)$. We will construct $w(z) = \sum_i^4 w_i (\ln(1 + z))^i$, using Eq. (3) and a similar χ^2 statistic to determine the likelihood for the terms w_i to $i = 4$ (4th order). The seven-dimensional likelihood manifold for (w_i, Ω_M, H_0) is computed using a Monte Carlo Markov Chain (MCMC). The MCMC procedure involves randomly choosing values for w_i , Ω_M , and H_0 , computing the luminosity distance, evaluating the χ^2 of the fit to supernova data, and then determining whether to accept or reject the set of parameters based on whether χ^2 is improved (using a Metropolis-Hastings algorithm). A set of parameters which is accepted to the chain forms a new starting point for the next guess and the process is repeated for a sufficient number of steps (convergence can be checked via the method of Dunkley et al. 2005). Ultimately, the list (aka chain) of the randomly chosen and accepted parameters forms a

¹⁹For comparison, a constant w model requires $w < -0.7$ if dark energy does not evolve to last scattering. From this we can see that even modest evolution, if unwavering, will become incompatible with a high-redshift constraint. This result is very similar to that of Wang & Mukerjee 2006.

good approximation of the likelihood distribution (Knox, Christensen, & Skordis 2001).

The best solution and its uncertainty for $w(z)$ is shown in Figure 10 for the quartic polynomial and low-order descriptions of $w(z)$. As shown, the low-order fit implies much greater precision concerning dark energy (with a 95% confidence region which is 7.2 times smaller).

The higher-order fit suffers in comparison, tolerating non-monotonic and even oscillating solutions for $w(z)$ as well as recent changes. The only (natural) limitation to the high-order fit comes from direct confrontation with data. Inclusion of the *HST*-discovered SNe Ia alone reduces the confidence intervals by a factor of 1.6. Yet, despite the extra freedom, the recent equation-of-state parameter remains well constrained. In Figure 11 we show the uncertainty as a function of redshift for $w(z)$ for the low-order and high-order fits with and without the high-redshift *HST* data. The difference in implied precision on $w(z)$ from the two parameterizations is very similar to the difference seen using a weak or strong prior at high redshift. Both a simple parameterization and a strong, high-redshift prior greatly restrict the allowed wandering of $w(z)$, though neither can be well-justified. In this way (and others discussed in the next section) we can see that a simple dark-energy parameterization *is equivalent* to a strong and unjustified prior on the nature of dark energy. The conclusions we draw either from the polynomial form with a strong prior or from the simple form with a weak prior are powerfully shaped by the data and are unlikely to be completely misled by a bad assumption.

An alternative approach to parameterizing $w(z)$ and constraining the parameters is to extract discrete, uncorrelated estimates of $w(z)$ as a function of redshift, analogous to the uncorrelated estimates of $H(z)$ derived in the last section. Following a method established by Huterer & Cooray (2005), we can extract the uncorrelated and model-independent band power estimates of $w(z)$ similar to a principal component analysis.

The evolution of w may be usefully resolved across several redshift bins or steps. Let w_i be a constant value of $w(z)$ in bin i . For a given experiment, the w_i will generally be correlated with each other because measurements of d_l constrain redshift integrals of $w(z)$; see Eq. (8). We can use a MCMC to obtain the likelihood surface for the variables in the vector $\vec{w} = [w_1, w_2, \dots, w_n]$.

Assume for simplicity that the mean value of \vec{w} from the likelihood surface has already been subtracted so that now $\langle w_i \rangle = 0$. In general, the variables will be correlated, with a

correlation matrix

$$\mathbf{C} = \langle \vec{\mathbf{w}} \vec{\mathbf{w}}^T \rangle = \begin{pmatrix} \sigma_{w_1}^2 & \cdots & \sigma_{w_1 w_n} \\ \vdots & & \vdots \\ \sigma_{w_n w_1} & \cdots & \sigma_{w_n}^2 \end{pmatrix}$$

What we're interested in is finding a linear transformation from \vec{w} into some new vector $\vec{\mathcal{W}}$ such that the correlation matrix for the new vector is diagonal (in other words, we want $\langle \mathcal{W}_i \mathcal{W}_j \rangle = 0$ for $i \neq j$). Since there are an infinite number of matrices that diagonalize \mathbf{C} there are an arbitrary number of ways to do this.

The simplest is to decompose \mathbf{C} into eigenvalues and eigenvectors, and use the eigenvectors to multiply \vec{w} . If

$$\mathbf{C} = \mathbf{V}^T \mathbf{\Lambda} \mathbf{V},$$

where $\mathbf{\Lambda}$ is diagonal, then in turn

$$\mathbf{V} \mathbf{C} \mathbf{V}^T = \mathbf{\Lambda}.$$

Therefore if we choose the vector $\vec{\mathcal{W}}$ to be equal to $\mathbf{V} \vec{\mathbf{w}}$, then

$$\begin{aligned} \langle \vec{\mathcal{W}} \vec{\mathcal{W}}^T \rangle &= \langle (\mathbf{V} \vec{\mathbf{w}}) (\mathbf{V} \vec{\mathbf{w}})^T \rangle \\ &= \mathbf{V} \langle \vec{\mathbf{w}} \vec{\mathbf{w}}^T \rangle \mathbf{V}^T = \mathbf{V} \mathbf{C} \mathbf{V}^T = \mathbf{\Lambda}. \end{aligned}$$

So in this case $\vec{\mathcal{W}}$ has a diagonal correlation matrix. However, transforming from \vec{w} to $\vec{\mathcal{W}}$ in this way will often involve both adding and subtracting individual entries of \vec{w} to get a particular entry of $\vec{\mathcal{W}}$ so physically interpreting what $\vec{\mathcal{W}}$ means can be difficult. It's actually possible to use a different transformation to get a $\vec{\mathcal{W}}$ that is in some sense “closer” to \vec{w} . A slightly more complicated transformation is to define a matrix \mathbf{T} such that

$$\vec{\mathcal{W}} = \mathbf{T} \vec{\mathbf{w}} = \mathbf{V}^T \mathbf{\Lambda}^{-\frac{1}{2}} \mathbf{V} \vec{\mathbf{w}},$$

where $\mathbf{\Lambda}^{-\frac{1}{2}}$ is just the diagonal matrix of the reciprocal of the square root of each eigenvalue. With this transformation the covariance matrix for $\vec{\mathcal{W}}$ is

$$\begin{aligned} \langle \vec{\mathcal{W}} \vec{\mathcal{W}}^T \rangle &= \langle (\mathbf{V}^T \mathbf{\Lambda}^{-\frac{1}{2}} \mathbf{V} \vec{\mathbf{w}}) (\mathbf{V}^T \mathbf{\Lambda}^{-\frac{1}{2}} \mathbf{V} \vec{\mathbf{w}})^T \rangle \\ &= \mathbf{V}^T \mathbf{\Lambda}^{-\frac{1}{2}} \mathbf{V} \langle \vec{\mathbf{w}} \vec{\mathbf{w}}^T \rangle \mathbf{V}^T \mathbf{\Lambda}^{-\frac{1}{2}} \mathbf{V} \\ &= \mathbf{V}^T \mathbf{\Lambda}^{-\frac{1}{2}} \mathbf{V} \mathbf{C} \mathbf{V}^T \mathbf{\Lambda}^{-\frac{1}{2}} \mathbf{V} \\ &= \mathbf{V}^T \mathbf{\Lambda}^{-\frac{1}{2}} \mathbf{\Lambda} \mathbf{\Lambda}^{-\frac{1}{2}} \mathbf{V} = \mathbf{I}. \end{aligned}$$

So with this transformation the correlation matrix for $\vec{\mathcal{W}}$ is just the identity matrix. Further, with a matrix of the form $\mathbf{V}^T \mathbf{\Lambda}^{-\frac{1}{2}} \mathbf{V}$, the entries of \mathbf{T} are much more likely to be

positive (the eigenvalues are positive, so any negative entries in the eigenvector matrix \mathbf{V} will tend to multiply together and become positive).

This is the transformation we used, with one further modification. Explicitly writing out the transformation for a single entry in $\vec{\mathcal{W}}$

$$\mathcal{W}_i = \sum_j T_{ij} w_j.$$

For a given i , T_{ij} can be thought of as weights for each w_j in the transformation from \vec{w} to \mathcal{W}_i . We are free to rescale each \mathcal{W}_i without changing the diagonality of the correlation matrix, so we then multiply both sides of the equation above by an amount such that the sum of the weights $\sum_j T_{ij}$ is equal to one. This allows for easy interpretation of the weights as a kind of discretized window function. This is, in fact, what we plot as the window function for the decorrelated parameters in the paper.

The resultant values of \mathcal{W}_i are thus uncorrelated (in that there is no covariance between the errors of any pair) and free to vary independently, subject only to the constraints of the data. Each uncorrelated measure of \mathcal{W}_i can be tested against the cosmological constant expectation of $\mathcal{W}_i = -1$, independently as well as collectively. Again, we use the weak, strong, and strongest priors, the last two including R_{CMB} and $R_{0.35}$ with $w(z > 1.8)$ equal to -1 or the value in the highest-redshift bin, respectively. We also used the same three redshift bins defined by $n\Delta z = 40$, resulting in three independent measures of $w(z)$ anchored at approximately $z=0.25, 0.70$, and 1.35 (with boundaries of $z = 0, 0.45, 0.935$, and 1.8) for the terms $\mathcal{W}_{0.25}$, $\mathcal{W}_{0.70}$, and $\mathcal{W}_{1.35}$, respectively. Thus there are five free parameters in the MCMC chain corresponding to the 3 values for \mathcal{W}_i , Ω_M , and H_0 . The likelihoods and confidence intervals for these terms are shown in Figure 12, 13, and 14 (respectively) and given in Table 5. The rows of \mathbf{T} are represented as the window functions in Figures 12, 13, and 14. As expected, the lowest-redshift measure of $w(z)$, $\mathcal{W}_{0.25}$, is derived primarily from the lowest-redshift bin which provides over 90% of the weight. The highest-redshift measure, $\mathcal{W}_{1.35}$, is mostly derived from the highest-redshift bin which contributes two-thirds of the weight of the measurement, but also relies on the lower-redshift bins to decouple high-redshift measurements of d_l from the low-redshift behavior of $w(z)$.

For the two lowest-redshift bins, the likelihood distributions are close to Gaussian, but for $\mathcal{W}_{1.35}$ the distribution can be quite skewed, requiring an explanation of the definition of our confidence intervals and reported values of \mathcal{W}_z . In Table 5 and Figures 12, 13, and 14, we define a $+1\sigma$ and -1σ region to be the boundaries at which the likelihood falls to 0.6065 of the peak on either side (i.e., as for a Gaussian), a definition which neglects the non-Gaussian tails to provide the frequently sought error bar. Likewise, we define a 2σ region as the boundaries of equal likelihood which contain 95% of the likelihood. We also

report the values of the peak of the likelihood for \mathcal{W}_z in the table.

For the weak prior, the three measures ($\mathcal{W}_{0.25}$, $\mathcal{W}_{0.70}$, and $\mathcal{W}_{1.35}$) are all consistent with $w = -1$ at or near the 68% confidence interval. The lowest-redshift bin remains well constrained with $\mathcal{W}_{0.25} = -1.06 \pm 0.10$ despite the additional freedom at higher redshifts. The next bin is modestly well constrained at $\mathcal{W}_{0.70} = -0.46 \pm 0.46$, though the likelihood in the highest-redshift bin has only begun to appear at all localized. Although the maximum likelihood values of $w(z)$ are monotonic in redshift, any trend is not significant. The constraints are weakest at high redshift where the data are sparse and discrete values of $w(z)$ become harder to isolate from integrated constraints. Figure 15 shows the impact of adding SNe Ia to the sample at the highest redshifts from *HST*. The first published sample from R04 began the process of localizing the highest redshift bin and markedly improved the intermediate bin, with no impact on the nearest bin. For the weakest prior which lacks any complementary constraints at high redshift, the increased sample has provided only modest gains.

For the strong prior, the nearby bin is unchanged, the uncertainty in the intermediate bin tightens by 25%, and the highest-redshift bin becomes significantly more peaked with a factor of two reduction in uncertainty. A modest tension exists with $w = -1$ in the middle bin (less than 2σ) (with no apparent trend in redshift). However, most of the data in this intermediate bin come from previous and on-going ground-based surveys and is rapidly growing in size. Thus we can expect this bin to soon come into better focus. Interestingly, the full sample considered here will soon be significantly augmented by the addition of 60 new SNe Ia with high-quality data from the first ESSENCE dataset of Wood-Vasey et al. (2007) which taken together with the past data, we note, results in a reduction of the difference with $w = -1$ at these redshifts to $\sim 1 \sigma$.

For the strong prior, the addition of the high-redshift *HST* data shown in Figure 15 provides strong gains in the precision of $\mathcal{W}_{1.35}$, especially with the sample published here for which we find $\mathcal{W}_{1.35} = -0.8_{-1.0}^{+0.6}$, marking significant inroads into the measurement of the early-time behavior of dark energy. Indeed, this measurement represents the most distinctive contribution of the *HST*-discovered SNe Ia. Combined with the low-redshift measurement, $\mathcal{W}_{0.25}$, the change $\mathcal{W}_{0.25} - \mathcal{W}_{1.35} = -0.3_{-1.0}^{+0.6}$ over one unit of redshift, disfavoring rapid changes, i.e., $|dw/dz| \gg 1$. Indeed, without the *HST* data, any measurement of the same $\mathcal{W}_{1.35}$ is not meaningful because the sample would contain no SNe at $z \sim 1.35$. The gain from the weak to the strong prior results from the complementary nature of the contributions of the SN data, the BAO measurement, and the WMAP measurement moderated by the high-redshift integration.

For the strongest prior, the tension within the highest-redshift bin has grown between

the SNe contained within and the extrapolation of the implied behavior of dark energy continuously to $z = 1089$. Any growing mode or non-accelerating type behavior for dark energy ($w > -1/3$) is curtailed. While this plot looks convincing, it is worth noting that non-accelerating modes were mildly favored by the weak prior. The embedded assumption of the way dark energy changes with redshift dominates over the information added by considering the data on $w(z)$. Because this prior relies on the correctness of guesses, we conclude that the apparent gain in information is at best risky and at worst, illusionary. Thus, we discourage the use of other parameterizations of dynamic dark energy in which the behavior of dark energy between $z = 1.8$ and $z = 1089$ remains important and a determining factor.

Not surprisingly, the addition of the SNLS sample to the full sample provides the most improvement in the lowest-redshift bin, about 10% in σ_w , but little gain in the intermediate bin (3%) and none in the highest redshift bin.

The likelihood distribution for $\mathcal{W}_{1.35}$ also empirically characterizes the most basic property of dark energy at $z > 1$, the way it gravitates. Using the strong prior, the likelihood that high-redshift dark energy has negative pressure, i.e., $\mathcal{W}_{1.35} < 0$, is 97.6% (or 99% for the MLCS2k2 fits to the Astier et al. light curves). (We note that the likelihood contained beyond a single boundary such a $w < 0$ cannot be directly inferred from our non-gaussian confidence regions because they have been defined using two boundaries and the requirement that the boundary likelihoods match.)²⁰ *Thus, the defining property of dark energy appears to be intact even during the epoch of matter domination.* We can say with greater confidence (99.99%) that if a decaying scalar field is responsible for this high-redshift dark energy, its energy is not primarily kinetic ($w = 1$). With less confidence, 93.4%, we can say that early dark energy provided repulsive gravity ($w < -1/3$). The nature of dark energy at high redshift ($z > 1$) may be of particular interest because classes of tracker models predict rapid changes in $w(z)$ near epochs when one energy density (e.g., radiation, dark matter, or dark energy) becomes dominant over another. For example, Albrecht and Skordis (2000) describe a form of potential which gravitates as the dominant mass-energy component at a given epoch. Simply put, this model would predict that the equation of state of the dark energy would mimic matter ($w = 0$) during the decelerating, matter-dominated phase (with a brief transition “ripple” during which $w > 0$) and the aforementioned likelihood for $\mathcal{W}_{1.35} \geq 0$ would appear inconsistent with this model.

²⁰The strongest prior would appear to provide even greater confidence for this statement. However, as we discussed, this prior seems unjustifiably strong and its use in this context is somewhat circular (i.e., guessing, and then inferring, the nature of dark energy at high redshift). In contrast, the strong prior brings the most independent information to bear on the early-time behavior of dark energy.

However, future observational and theoretical work should better define if variants of this idea remain viable.

Finally, we may consider whether three additional parameters to describe $w(z)$ are actually needed to improve upon a flat, Λ -cold-dark-matter (Λ CDM) model fit to the data (i.e., the “concordance” value of $\Omega_M = 0.29$, $\Omega_\Lambda = 0.71$). The residuals from this fit are shown in Figure 17 and have a dispersion for all data of 0.21 mag. To determine the need for complex forms of $w(z)$ we can calculate the improvement to the fit,

$$\chi_{eff}^2 \equiv -\Delta(2\ln\mathcal{L}) = 2\ln\mathcal{L}(w = -1) - 2\ln\mathcal{L}(w_i = \mathcal{W}_i), \quad (9)$$

with i additional free parameters. For the weak, strong, and strongest priors we find an improvement of $\chi_{eff}^2 = 4$, 5.5, and 5.5, respectively, for the three additional degrees of freedom, in no case requiring the additional complexity in dark energy (improvements of > 14 would be noteworthy). Likewise, there is no improvement at all for the Akaike Information Criterion (i.e., $\Delta\text{AIC} = \Delta\chi^2 - 2i$; Liddle et al. 2004) with changes of -2 , -0.5 , and -0.5 , respectively which fail to overcome the penalty of increased complexity in the model.

4. Discussion

We have presented a sample of SNe Ia at $z \geq 1.0$, found and followed with *HST*, more than double the size of those in R04. We have also performed a set of limited cosmological analyses focusing on tests and models we expect to be most sensitive to the additional data. Given the set of independent experimental constraints and the panoply of dark-energy models, we expect that the most interesting tests and constraints will be discovered by future work. We now discuss caveats and tests of this dataset.

4.1. Systematics

Past research has sought to quantify and characterize possible systematic errors in supernova-based cosmological inference (e.g., Riess et al. 1998; Perlmutter et al. 1999; Knop et al. 2003; Tonry et al. 2003; Riess et al. 2004; Filippenko 2005; Astier et al. 2006). Here we consider systematics which are more sensitive to the uniquely high redshifts of our sample or otherwise merit new consideration.

Strong or weak lensing may skew the distribution of magnitudes but will not bias the mean (Holz 1998). Extensive analyses of the expected lensing along the line-of-sight for the

SNe found in the GOODS fields in R04 by Jönsson et al. (2006) show that the distribution of magnifications matches an unbiased sample having a mean consistent with unity and that attempting to correct for this effect has negligible impact on the derived cosmological parameters. This is not surprising, as the dispersion of lensing-induced magnitudes is less than 0.05 mag, far less than the intrinsic dispersion. The same was concluded in R04 using the methods of Benítez et al. (2002), though with less accuracy than in Jönsson et al. (2006).

As high-redshift SN Ia surveys continue, sample sizes increase, and data collection methods improve, it may become sensible to discard older samples in an effort to reduce systematic errors in the cosmological sample associated with inferior calibration (e.g., data from Riess, et al. 1998, Perlmutter et al. 1999, Tonry et al. 2003, and Knop et al. 2003). At present we do not believe this is warranted, especially since it is not yet possible to similarly replace the low-redshift sample whose data was collected with similar techniques as the older high-redshift data. Nevertheless, it may be instructive to determine the impact on the determination of the nature of dark energy using at intermediate redshifts only the more modern and homogeneous data from Astier et al. (2006) and with the same HST data at high redshift and low-redshift sample found here. From this more limited sample we find no significant change for the lowest redshift measure of the equation of state, $\mathcal{W}_{0.25}$, and a 30% decrease in its precision. For the intermediate redshift bin, $\mathcal{W}_{0.70}$, we find values *more* consistent with a cosmological constant with $-1.11^{+0.59}_{-0.82}$ and $-0.76^{+0.42}_{-0.56}$, for the weak and strong prior, respectively, representing a 50% to 100% decrease in the precision. For the highest redshift measure, $\mathcal{W}_{1.35}$, we find values *less* consistent from a cosmological constant, with $3.39^{+4.21}_{-2.91}$ and $-0.23^{+0.75}_{-0.72}$, for the weak and strong prior, respectively, representing little change in the mean precision. The two most discrepant measurements from $w(z) = -1$ are with the full dataset and the strong prior for $\mathcal{W}_{0.70} = -0.15$ ($-1\sigma = -0.41$, $-2\sigma = -0.89$) and for the limited dataset and the weak prior for which $\mathcal{W}_{1.35} = 3.39$ ($-1\sigma = -2.91$, $-2\sigma = -23.1$). Both measurements are inconsistent at more than the 1 sigma level and less than the 2 sigma level with a cosmological constant, an insignificant difference for 3 independent measurements of $w(z)$. We also note that an increased sample of 60 new SNe Ia at $0.3 < z < 0.7$ from ESSENCE (Wood-Vasey et al. 2007) further reduces the apparent difference from a cosmological constant from the full-sample for the intermediate redshift bin.

Evolution of SN explosions remains the most pernicious systematic source of uncertainty and is challenging to quantify (see, however, Riess & Livio 2006 for a suggestion for future observations). The two most direct lines of evidence that evolution with redshift, is limited to less than $\sim 10\%$ in luminosity comes from studies of SN Ia distances across host-galaxy (characteristic) ages (Sullivan et al. 2003; Riess et al. 1998; Jha 2002; Jha, Riess, & Kirshner 2006, Gallagher et al. 2005) and the consistency of SN Ia distances with the

expected deceleration at $z > 1$ (R04).

An alternative to evolution proportional to redshift would be evolution that is proportional to look-back time (Wright 2002). However, this seems unlikely, as the evolution of cosmic properties to which SNe Ia may respond is more closely correlated with redshift than with time. Two natural examples are the evolution of cosmic metallicity as seen in damped Ly α systems (Kulkarni et al. 2005) and the minimum stellar mass of a star which can turn off the main sequence and donate the SN Ia white dwarf. Combined with the necessary delay required to produce SNe Ia (> 1 Gyr), the gradient in these physical parameters lies primarily with redshift, not time (Riess & Livio 2006).

Recent work has questioned the validity of the mean Galactic reddening-law parameter, $R_V = A_V/E_{B-V} = 3.1$, for use in determining the extinction in extragalactic SNe. Estimates of the typical value of R_V in distant galaxies hosting SNe Ia tend to prefer values somewhat less than 3.1 (Riess, Press, & Kirshner 1995; Jha 2002; Jha, Riess, & Kirshner 2006; Phillips et al. 1999), with values as low as $R_V = 2.3$ by Wang et al. (2006). An apparent correlation exists between R_V and A_V : SNe with greater extinction prefer lower values of R_V , and both of the well-studied SNe Ia with $A_V > 2$ mag (SN 1999cl and SN 1996ai) yield $R_V < 2.0$ (Jha, Riess, & Kirshner 2006). Wang et al. (2006) have suggested, as a natural explanation for reduced values of R_V , the occasional dominance of scattering over absorption caused by dust clouds in the circumstellar environment. Evidence does exist for the occasional and significant presence of circumstellar dust from at least 3 SNe Ia exhibiting light echos (SN 1995E, Quinn et al. 2006; SN 1998bu, Cappellaro et al. 2001; SN 1991T, Schmidt et al. 1994) and a few possible SNe Ia with circumstellar hydrogen seen at late times (e.g., SN 2002ic; Hamuy et al. 2003). In the presence of local dust, Wang et al. (2006) show that $1.8 < R_V < 3.1$ for normal, Milky-Way-type dust.

However, past determinations of the mean R_V for distant SNe Ia are strongly biased toward the few objects with large extinction and lower R_V , which have greater weight in these analyses. For example, Jha, Riess, & Kirshner (2006) analyzed the 33 nearby SNe Ia with the highest extinction ($A_V > 0.5$ mag) and found a median $R_V = 2.8$, well in excess of the weighted mean value of 1.8 (with half of this difference explained by the two SNe Ia with $A_V > 2$ mag). Because our cosmological analysis excludes (from the Gold sample) all SNe with $A_V > 0.5$ mag, we would expect the characteristic R_V in our sample to be better represented by the median, or perhaps closer to Galactic for low-extinction events. Further analyses of large samples of low-extinction events may yield greater insight on this issue.

Analyses which seek to correlate SN color with luminosity, such as those by Tripp & Branch (1999), Guy et al. (2005), and Astier et al. (2006), combine both the reddening-law parameter R_V and intrinsic luminosity-color relation parameter into a single relation.

If these independent, physical relations have the same dependence between color and brightness, or if the relative contributions of dust and populations to the relation do not change with redshift, then combining these effects into one should succeed. However, if one of these assumptions fails significantly (e.g., there is more or less dust on average at different redshifts), important systematic errors in the cosmological inference may result. In any case, the effective value of R_V from these analyses should be an average of the value from dust and the physics of SN explosions. The MLCS2k2 templates suggest that the intrinsic relation from normal SNe Ia would be $M/(B - V) \approx 1.8$, reducing the effective R_V below the typical value for the Galaxy as found by Tripp & Branch (1999), Guy et al. (2005), and Astier et al. (2006).

To determine the sensitivity of our cosmological analyses to a reduced value of R_V , we refit all of the distances using $R_V = 2.5$ and 2.0 and compared the results to our preceding distances determined with $R_V = 3.1$. We found our mean distance to increase by 0.026 mag and 0.042 mag for $R_V = 2.5$ and $R_V = 2.0$, respectively. However, we found the mean variation of this change to be negligible across redshift with less than a 0.01 mag difference between the bins used in Figure 7. The distance determinations to objects with large extinction ($A_V > 1$ mag) depend more critically on R_V , with an increase of 0.10 and 0.35 mag for SN 2002kc ($A_V = 1.35$ mag for $R_V = 3.1$) for $R_V=2.5$ and 2.0 , respectively. Such sensitivity is exactly the reason it is unwise to make use of well-reddened objects in cosmological analyses and why we limited our Gold sample to $A_V < 0.5$ mag.

Wood-Vasey et al (2007) has shown that a selection bias exists in the distribution of observed extinctions and luminosities of SNe Ia found in the ESSENCE Survey for supernovae discovered near the redshift limit of the survey. This bias can be corrected using Monte Carlo simulations of the survey selection. The bias becomes significant for SNe Ia which can only be found at a signal-to-noise ratio of less than 15 due to their apparent faintness and the survey’s limitations. For our HST SN survey, this limit occurs for SNe Ia at $z > 1.4$ and thus such selection bias has little affect on our sample, the great majority of which is at $z < 1.4$. The reason for the absence of SNe Ia at the redshift limit of our survey ($z \sim 1.7$) has been attributed to an apparent 2 to 3 Gyr delay between the formation of stars and the production of SNe Ia (Strolger et al. 2004).

At present, none of the *known*, well-studied sources of systematic error rivals the statistical errors presented here.

Now we consider systematic errors whose definition includes our present inability to discover them and to correct for them. Here we will quantify the translation of such systematic errors to our data analysis and their propagated effects on the cosmology. A simple form for general systematic errors in SN distances to take is a correlation with

redshift. Such a model provides an adequate (if naive) description of zeropoint errors tied to fixed passbands, errors in K-corrections, random errors from evolution (tied to look-back time), etc. This model is good at addressing zeropoint errors between small ground-based telescopes used to collect the $z < 0.1$ sample, errors from large ground-based programs which collected the sample at $0.1 < z < 0.8$, and from *HST* at $z > 1$. It is similar to the model used by the Supernova Acceleration Probe (SNAP) collaboration (Aldering 2005).

We define the covariance between two SNe to be $\langle \sigma_{\mu,1}\sigma_{\mu,2} \rangle = A^2 \exp[-|z_1 - z_2|/z_T]$, where A provides the correlation (in mag) for two SNe at the same redshift and z_T provides the decay length of the correlation in redshift. For the expected precision of calibration of *HST* and past datasets, we examine a model with $(A, Z_T) = (0.05, 0.05)$, and $(0.05, 0.10)$ against the error-free case $(0.0, 0.0)$. We consider $(0.05, 0.10)$ to be a rough estimate of the covariance of the SN dataset, in which SNe at like redshifts suffer the same 0.05 mag errors related to calibration, those transformed to adjacent rest-frame bandpasses ($z_T > 0.20$) share 0.02 mag of systematic error, and the entire Hubble flow sample ($z_T = 0.1$) shares an 0.03 mag error in common (and is not improved beyond the inclusion of ~ 100 SNe Ia). For the more optimistic model, $(0.05, 0.05)$, the correlation length of these errors is halved in redshift.

For the Gold sample of SNe Ia presented here, we use the redshifts and the distance errors (but not the distance measurements) to compute the Fisher Information Matrix combined with a typical prior on $\sigma_{\Omega_M} = 0.03$. To study these systematic errors we include a covariance matrix with off-diagonal terms given by our model and parameters. We then compute the expected 68% confidence level interval for the parameter space $w_0 - w'$ for the 3 cases. We find that our best guess at covariance, $(0.05, 0.10)$ broadens the interval by 27% whereas the more optimistic $(0.05, 0.05)$ broadens the interval by 17%. Thus we conclude that our present results remain dominated by statistical errors. However, as the sample grows, for this balance to remain true, ongoing improvements in calibration must be realized.

5. Summary and Conclusions

(1) We present 21 new *HST*-discovered SNe Ia and an improved calibration of the previous sample from R04. Together this sample contains 23 SNe Ia at $z \geq 1$, extending the Hubble diagram over 10 Gyr.

(2) We derive uncorrelated, model-independent estimates of $H(z)$ which well-delineate current acceleration and preceding deceleration. The *HST*-discovered SNe Ia measure

$H(z > 1)$ to slightly better than 20% precision.

(3) The full *HST*-discovered SN Ia sample, presented here, provides a factor of two improvement over our present ability to constrain simple parameterizations of the equation-of-state parameter of dark energy (w) and its evolution.

(4) Stronger priors and tighter constraints on the preferred cosmological model can be extracted from independent measurements tied to the surface of last scattering, but the use of these requires assumptions about the behavior of dark energy across a wide range of redshift ($1.8 < z < 1089$). The strongest of these priors, like the simplest dark energy parameterizations, appears unjustified in the presence of our current ignorance about dark energy. Assuming the effect of dark energy at $z > 1.8$ is minimal, we derive meaningful constraints on the early properties of dark energy: $w(z > 1) = -0.8_{-1.0}^{+0.6}$ and $w(z > 1) < 0$, i.e., negative pressure, at 98% confidence.

(5) At present, we find that the use of additional parameters to describe $w(z)$ does not provide a statistically significant improvement to the fit of the redshift-magnitude relation over the use of a simple cosmological constant.

(6) An analysis of the $z > 1$ sample-averaged spectrum shows it to be consistent with the mean spectrum of SNe Ia over the last 10 Gyr, failing to reveal direct evidence for SN Ia evolution.

We are grateful to Dorothy Fraquelli, Sid Parsons, Al Holm, Tracy Ellis, Richard Arquilla, and Mark Kochte for their help in assuring rapid delivery of the *HST* data. We also wish to thank Ryan Chornock, Anton Koekemoer, Ray Lucas, Max Mutchler, Sherie Holfeltz, Helene McLaughlin, Eddie Bergeron, and Matt McMaster for their help. Financial support for this work was provided by NASA through programs GO-9352, GO-9728, GO-10189, and GO-10339 from the Space Telescope Science Institute, which is operated by AURA, Inc., under NASA contract NAS 5-26555. Some of the data presented herein were obtained with the W. M. Keck Observatory, which is operated as a scientific partnership among the California Institute of Technology, the University of California, and NASA; the Observatory was made possible by the generous financial support of the W. M. Keck Foundation.

Table 4. χ^2 Comparison of Gold Set Data to Models, $cz > 7000 \text{ km s}^{-1}$

Model	χ^2 (for 184 SNe Ia)
$\Omega_M = 0.29, \Omega_\Lambda = 0.71$	150 ^a
$\Omega_M = 1.00, \Omega_\Lambda = 0.00$	285 ^a
$\Omega_M = 0.00, \Omega_\Lambda = 0.00$	164 ^a
High-redshift gray dust (with $\Omega_M = 1.00, \Omega_\Lambda = 0.00$)	344 ^b
Replenishing dust (with $\Omega_M = 1.00, \Omega_\Lambda = 0.00$)	150 ^b
Dimming $\propto z$ (with $\Omega_M = 1.00, \Omega_\Lambda = 0.00$)	266 ^b

^abest χ^2 after marginalizing over H_0

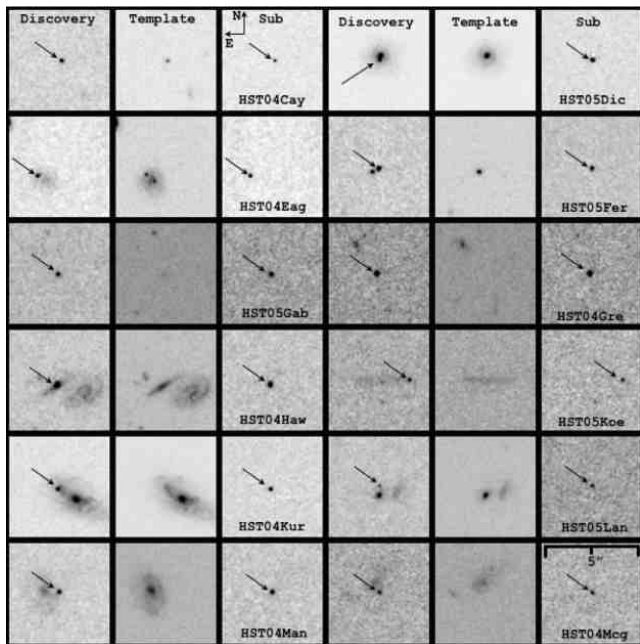
^abest χ^2 for best H_0

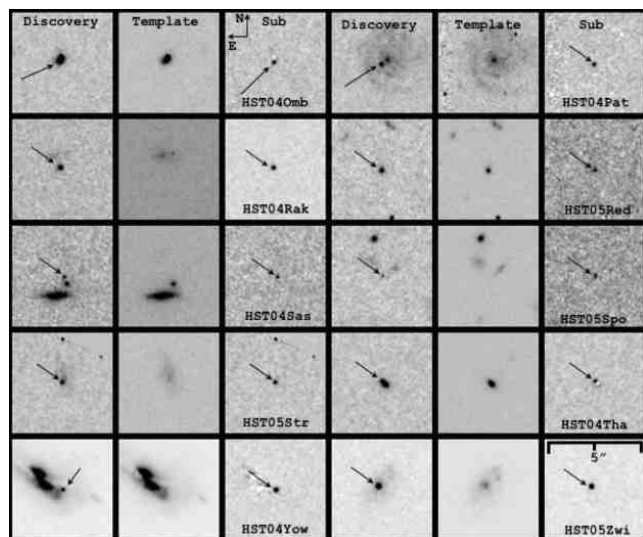
Table 5. Likelihood Regions For \mathcal{W}_z

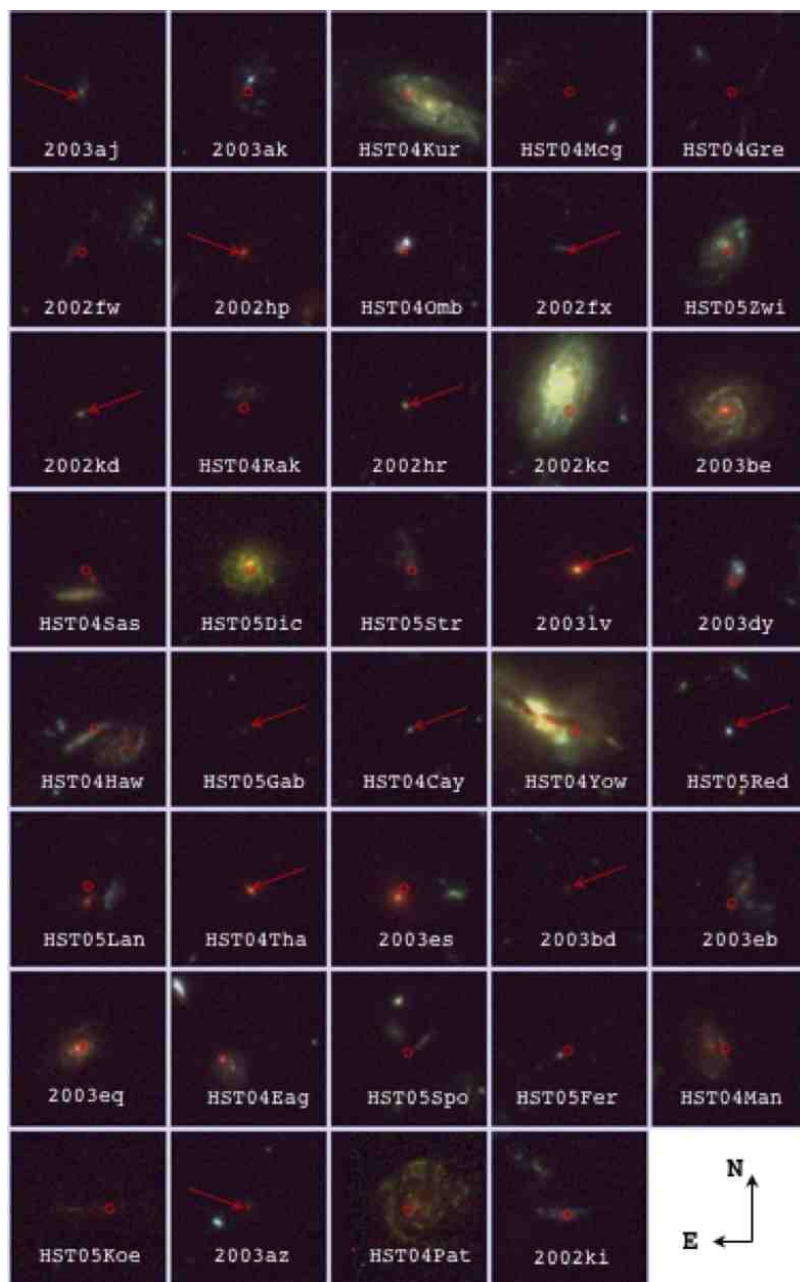
w_z	peak	1σ	2σ
Prior=Weak, Sample=All Gold			
$\mathcal{W}_{0.25}$	-1.05	-1.15 to -0.95	-1.26 to -0.85
$\mathcal{W}_{0.70}$	-0.45	-0.86 to -0.06	-1.49 to 0.32
$\mathcal{W}_{1.35}$	0.59	-2.62 to 3.03	-16.6 to 6.15
Prior=Weak, Sample=Gold minus HST			
$\mathcal{W}_{0.25}$	-1.06	-1.16 to -0.95	-1.27 to -0.86
$\mathcal{W}_{0.70}$	0.11	-0.43 to 0.61	-1.17 to 1.17
$\mathcal{W}_{1.35}$	10.77	1.86 to 18.55	-20.1 to 27.92
Prior=Strong, Sample=All Gold			
$\mathcal{W}_{0.25}$	-1.02	-1.12 to -0.93	-1.23 to -0.84
$\mathcal{W}_{0.70}$	-0.15	-0.57 to 0.131	-1.05 to 0.46
$\mathcal{W}_{1.35}$	-0.76	-1.78 to -0.16	-15.8 to 0.51
Prior=Strong, Sample=Gold minus HST			
$\mathcal{W}_{0.25}$	-1.03	-1.14 to -0.94	-1.25 to -0.85
$\mathcal{W}_{0.70}$	0.151	-0.26 to 0.61	-0.80 to 1.00
$\mathcal{W}_{1.35}$	-1.95	-5.89 to -0.70	-17.8 to 0.35
Prior=Strongest, Sample=All Gold			
$\mathcal{W}_{0.25}$	-1.02	-1.11 to -0.92	-1.21 to -0.83
$\mathcal{W}_{0.70}$	-0.13	-0.47 to 0.17	-0.88 to 0.48
$\mathcal{W}_{1.35}$	-0.85	-1.81 to -0.46	-17.0 to -0.30
Prior=Strongest, Sample=Gold minus HST			
$\mathcal{W}_{0.25}$	-1.03	-1.13 to -0.94	-1.24 to -0.85
$\mathcal{W}_{0.70}$	0.24	-0.17 to 0.64	-0.70 to 1.06
$\mathcal{W}_{1.35}$	-1.89	-5.50 to -0.80	-18.0 to -0.34
Prior=Strong, Sample=All Gold with MLCS2k2 Fits to SNLS SNe			
$\mathcal{W}_{0.25}$	-1.05	-1.14 to -0.94	-1.26 to -0.84
$\mathcal{W}_{0.70}$	-0.09	-0.45 to 0.23	-0.91 to 0.56
$\mathcal{W}_{1.35}$	-1.01	-2.23 to -0.26	-15.8 to 0.37

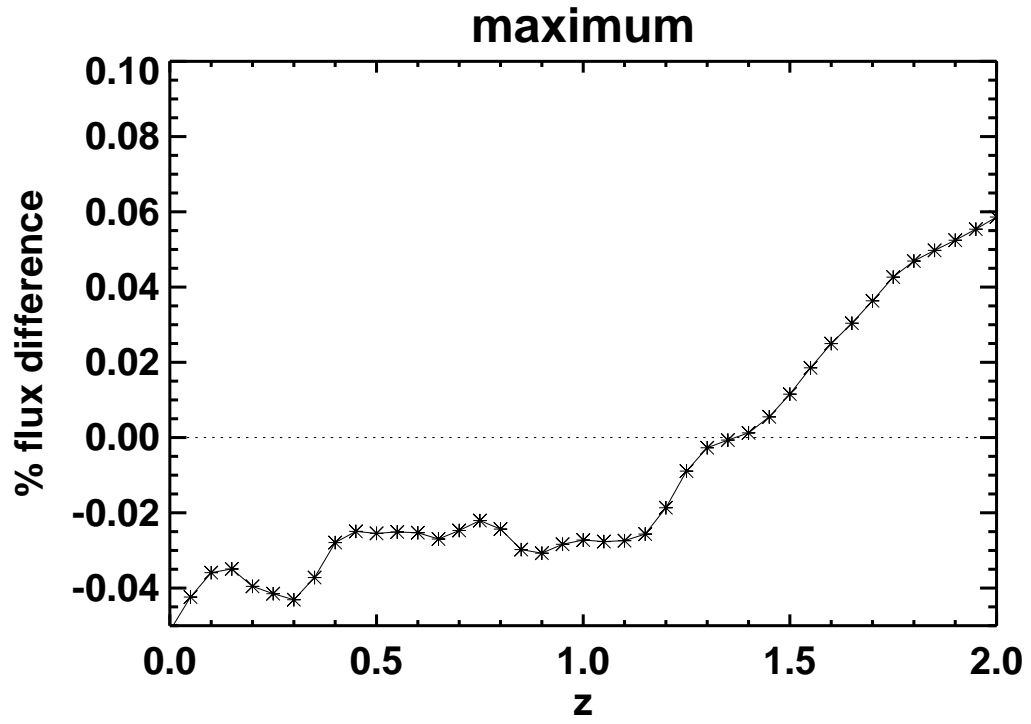
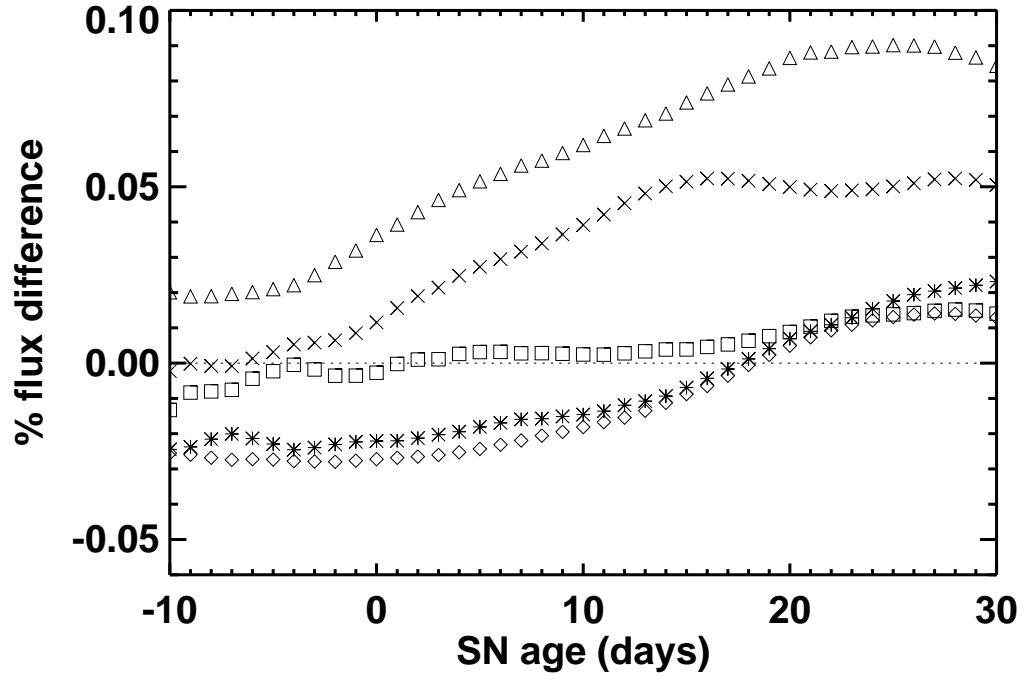
Table 6. HST-discovered Sample*; Distance Scale of Riess et al. 2004

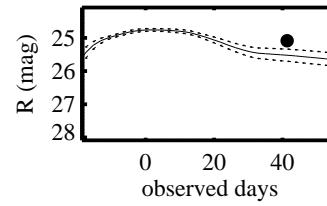
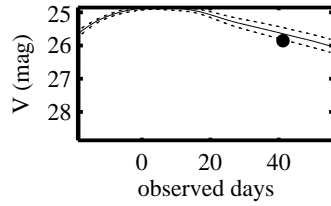
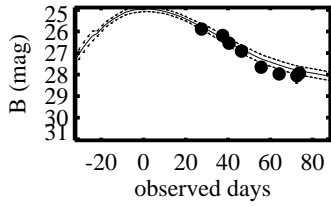
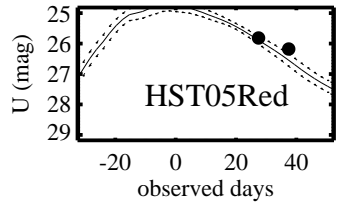
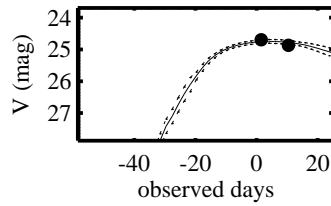
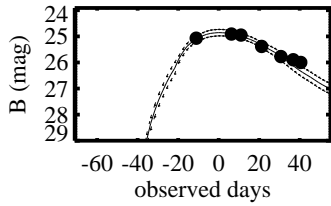
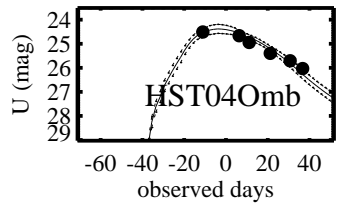
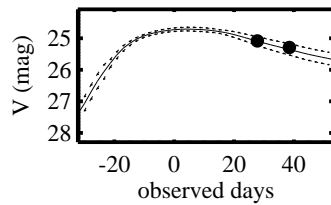
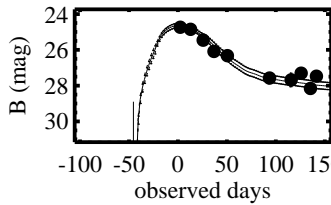
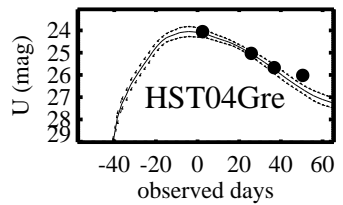
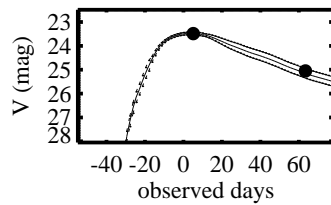
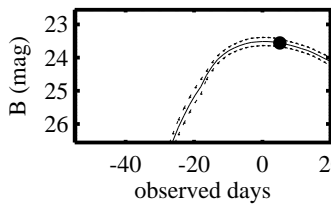
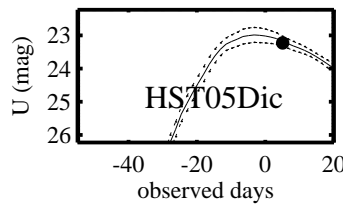
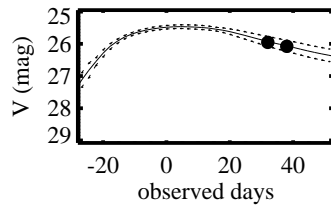
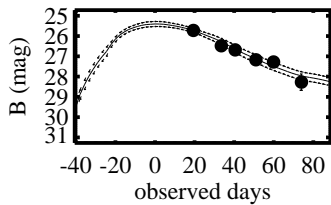
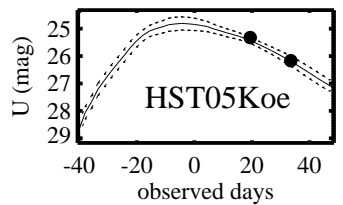
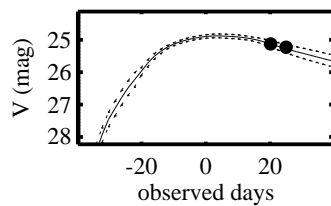
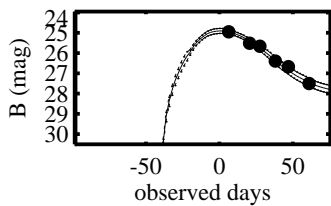
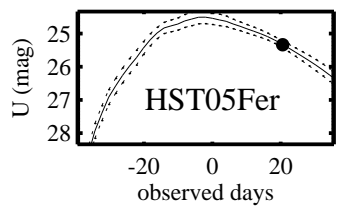
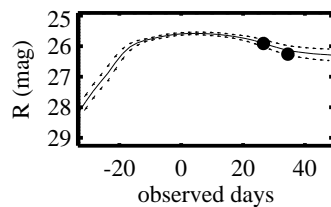
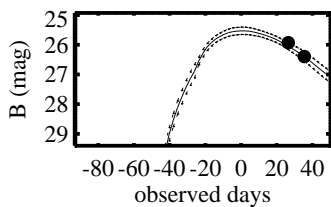
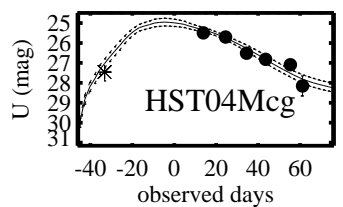
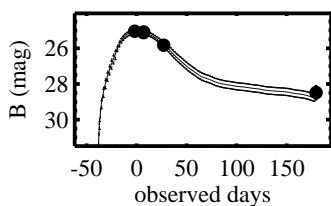
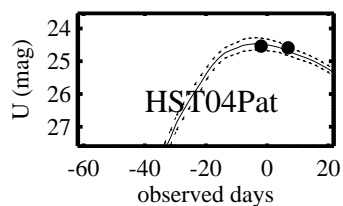
SN	z	μ_0^a	σ^b	host A_V	Δ	sample
1997ff	1.755	45.35	0.35	0.00	—	Gold
2002dc	0.475	42.24	0.20	0.21	0.19	Gold
2002dd	0.950	43.98	0.34	0.35	-0.34	Gold
2003aj	1.307	44.99	0.31	0.29	0.09	Silver
2002fx	1.400	45.28	0.81	0.50	-0.01	Silver
2003eq	0.840	43.67	0.21	0.22	-0.04	Gold
2003es	0.954	44.30	0.27	0.10	-0.08	Gold
2003az	1.265	44.64	0.25	0.73	-0.4	Silver
2002kc	0.216	40.33	0.19	1.35	-0.31	Silver
2003eb	0.900	43.64	0.25	0.28	-0.4	Gold
2003XX	0.935	43.97	0.29	0.26	-0.31	Gold
2002hr	0.526	43.08	0.27	0.70	-0.4	Silver
2003bd	0.670	43.19	0.24	0.34	0.02	Gold
2002kd	0.735	43.14	0.19	0.21	0.12	Gold
2003be	0.640	43.01	0.25	0.42	-0.22	Gold
2003dy	1.340	44.92	0.31	0.43	-0.4	Gold
2002ki	1.140	44.71	0.29	0.13	0.04	Gold
2003ak	1.551	45.07	0.32	0.75	-0.4	Silver
2002hp	1.305	44.51	0.30	0.22	0.32	Gold
2002fw	1.300	45.06	0.20	0.25	-0.20	Gold
HST04Pat	0.970	44.67	0.36	0.19	-0.4	Gold
HST04Mcg	1.370	45.23	0.25	0.14	-0.4	Gold
HST05Fer	1.020	43.99	0.27	0.45	-0.13	Gold
HST05Koe	1.230	45.17	0.23	0.13	-0.4	Gold
HST05Dic	0.638	42.89	0.18	0.42	-0.39	Silver
HST04Gre	1.140	44.44	0.31	0.11	-0.4	Gold
HST04Omb	0.975	44.21	0.26	0.39	-0.39	Gold
HST05Red	1.190	43.64	0.39	0.53	0.08	Silver
HST05Lan	1.230	44.97	0.20	0.23	0.26	Gold
HST04Tha	0.954	43.85	0.27	0.19	0.06	Gold
HST04Rak	0.740	43.38	0.22	0.20	-0.10	Gold
HST05Zwi	0.521	42.05	0.37	0.56	-0.18	Silver
HST04Hawk	0.490	42.54	0.24	0.18	-0.40	Silver
HST04Kur	0.359	41.23	0.39	2.49	-0.34	Silver
HST04Yow	0.460	42.23	0.32	0.43	-0.04	Gold
HST04Man	0.854	43.96	0.29	0.13	-0.01	Gold
HST05Spo	0.839	43.45	0.20	0.22	-0.07	Gold
HST04Eag	1.020	44.52	0.19	0.18	-0.27	Gold
HST05Gab	1.120	44.67	0.18	0.11	-0.20	Gold
HST05Str	1.010	44.77	0.19	0.12	-0.29	Gold
HST04Sas	1.390	44.90	0.19	0.26	0.35	Gold

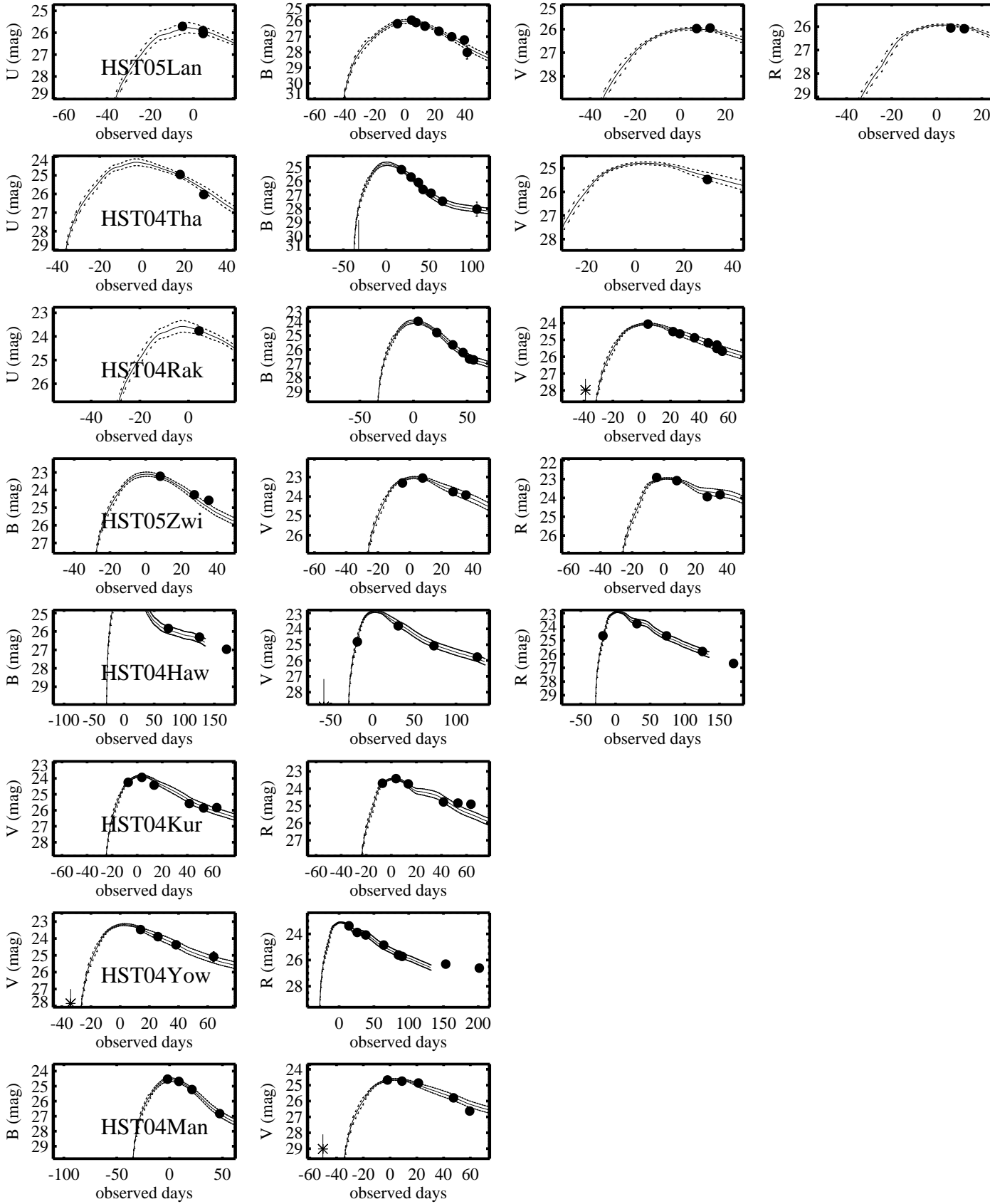


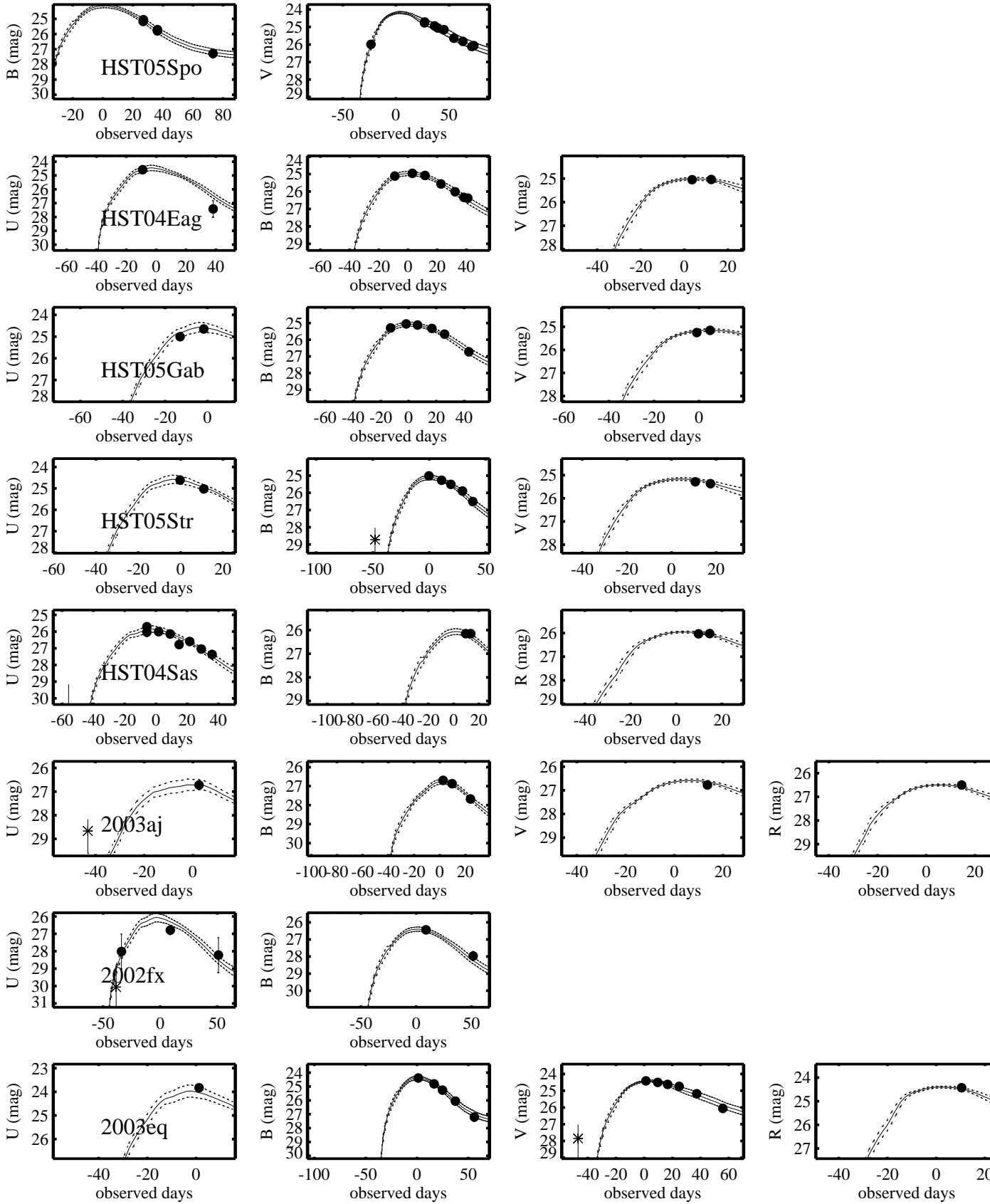


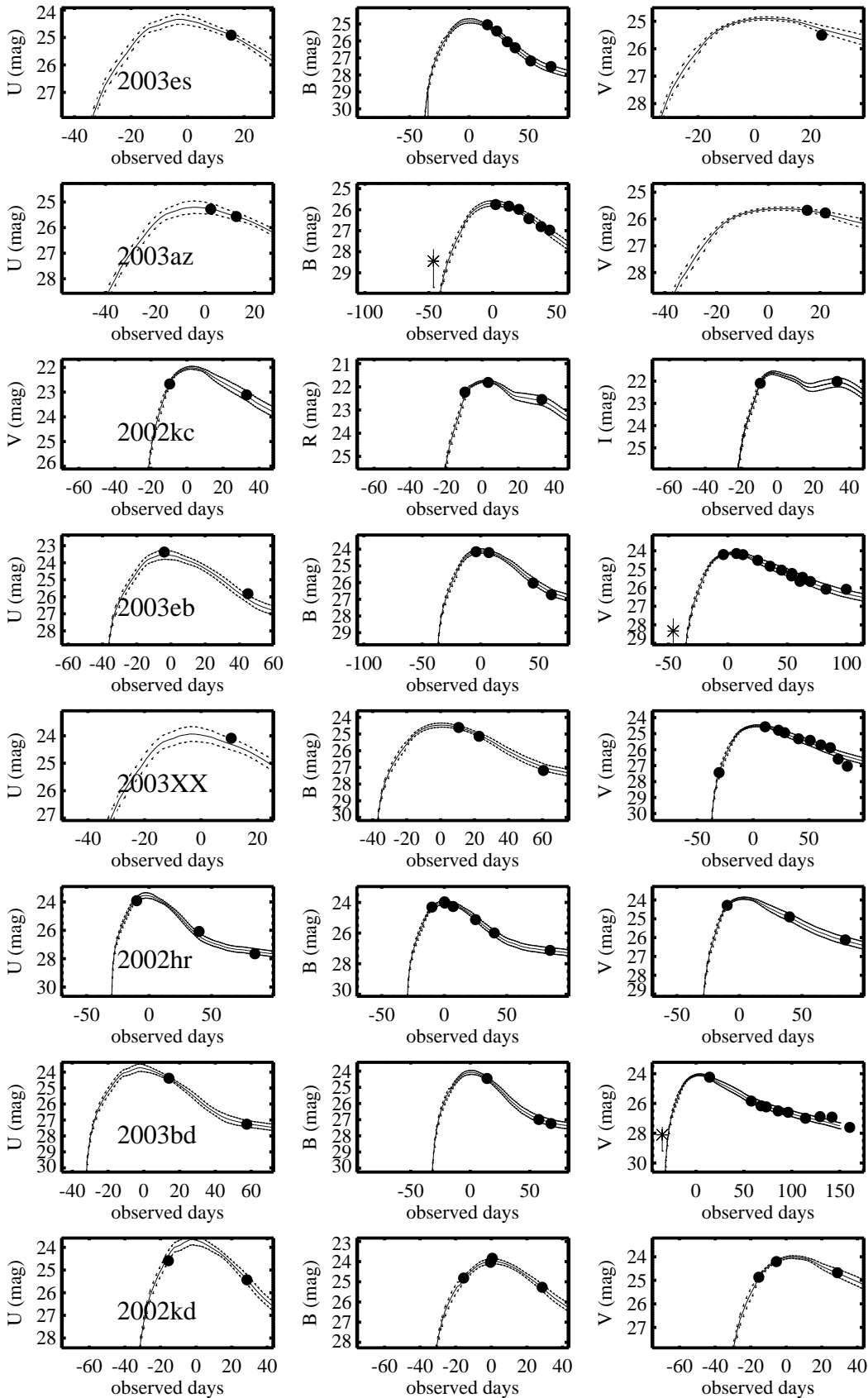


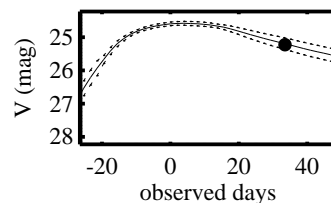
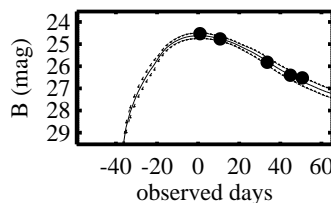
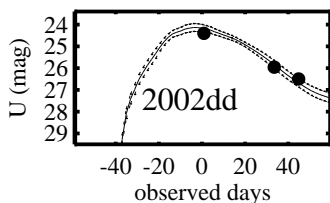
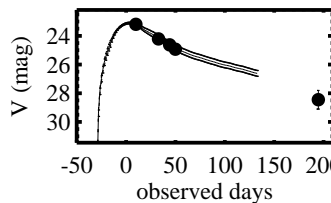
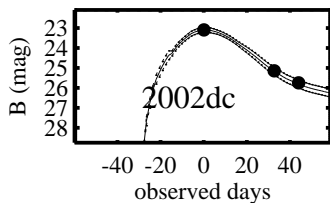
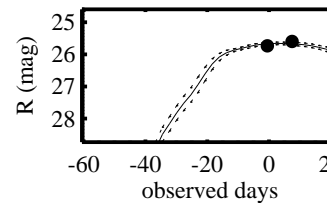
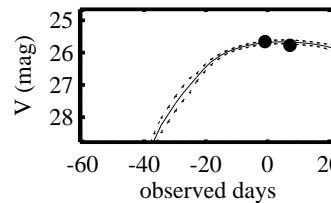
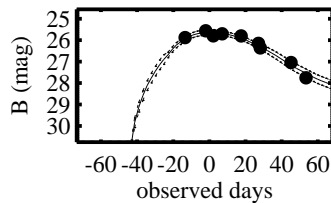
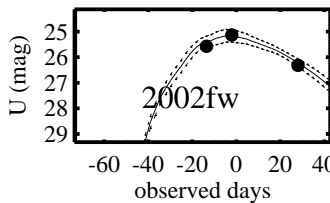
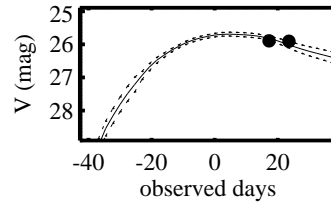
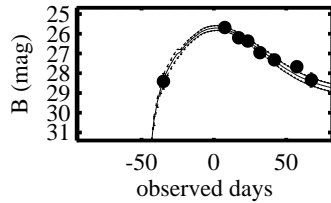
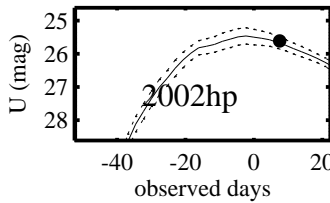
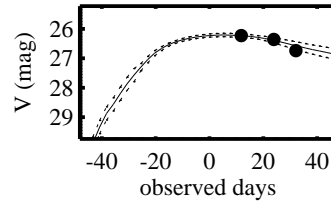
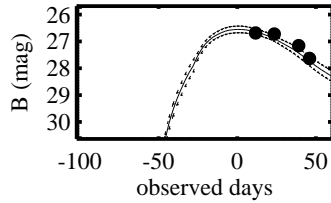
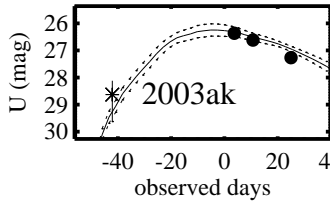
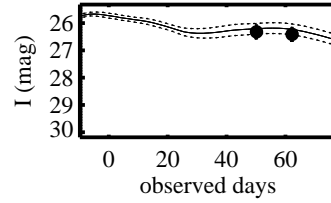
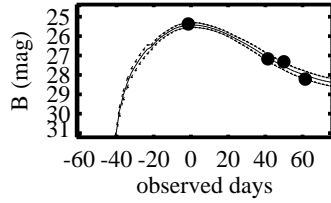
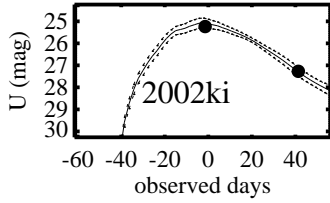
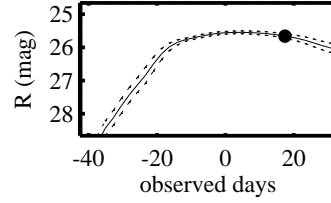
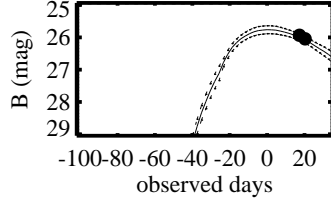
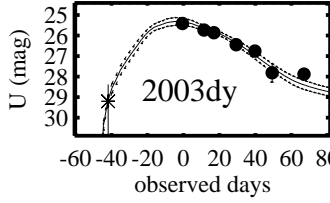
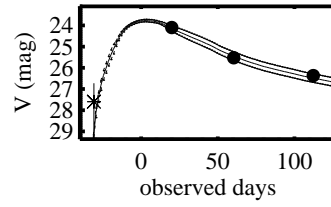
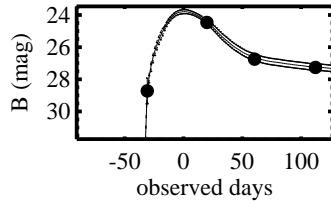
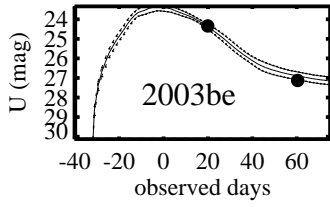


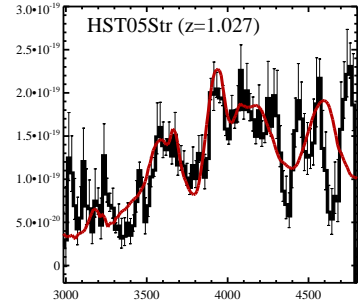
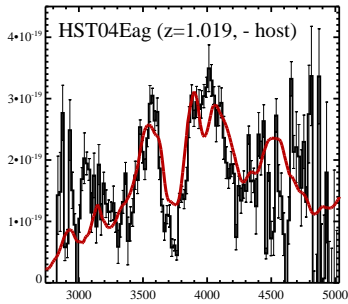
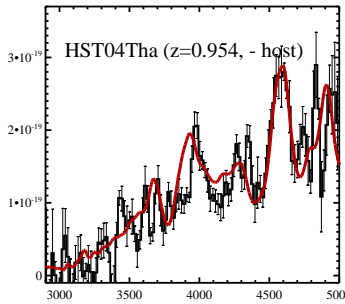
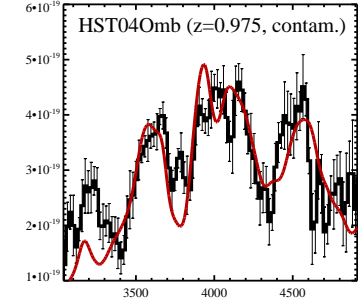
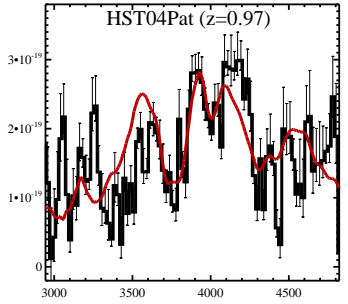
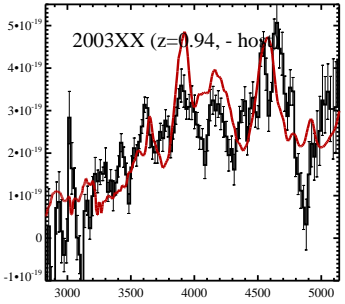
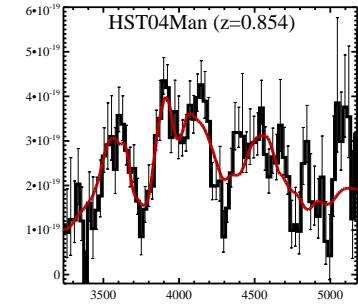
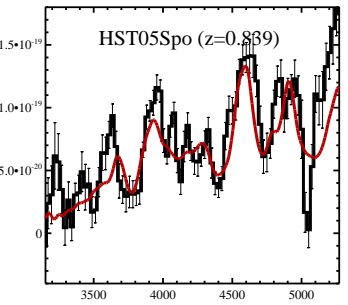
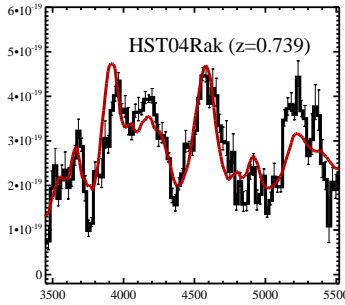
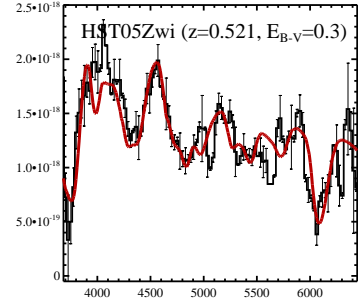
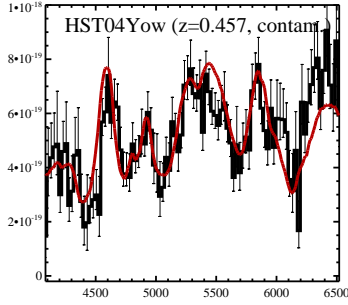
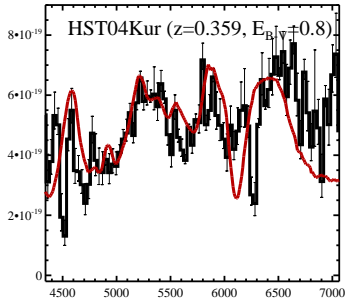


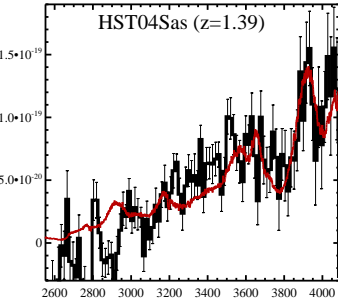
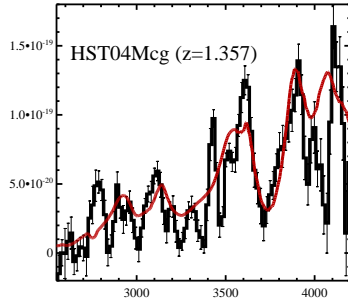
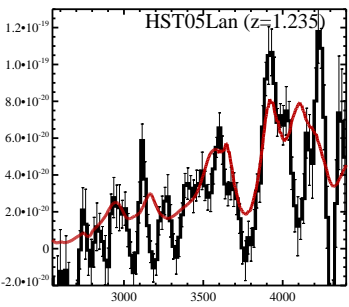
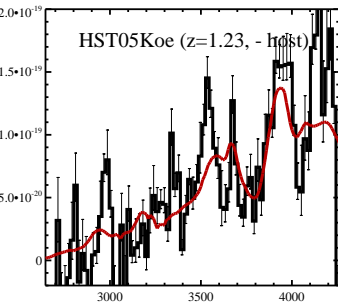
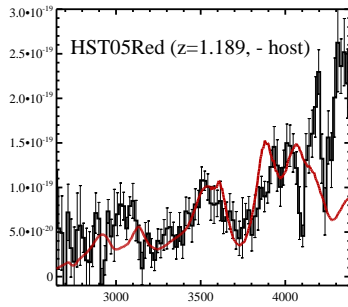
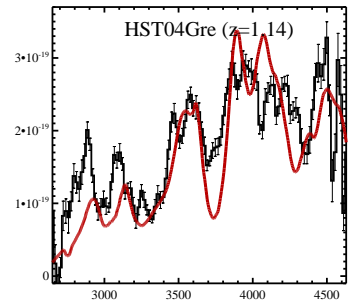
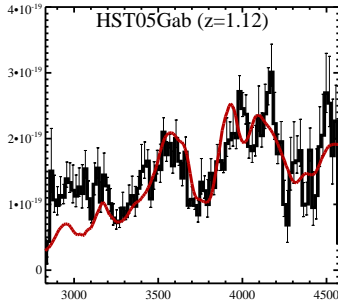
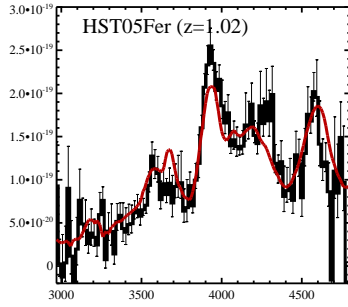


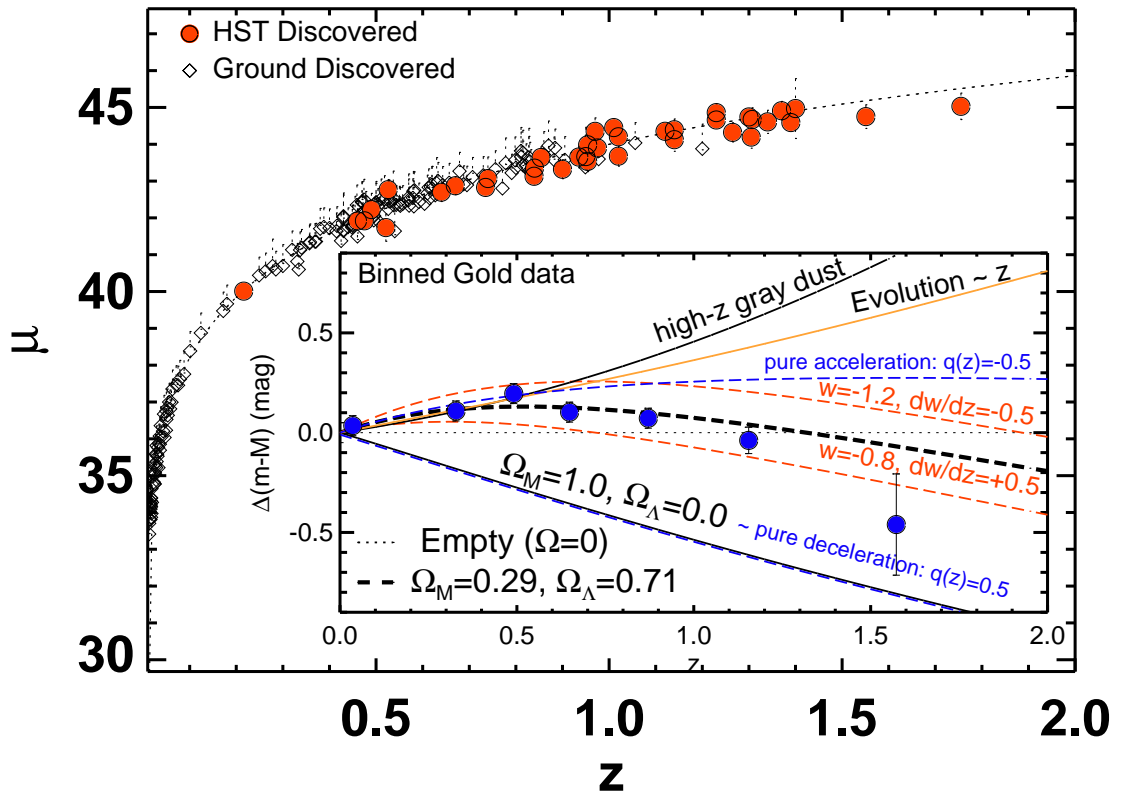


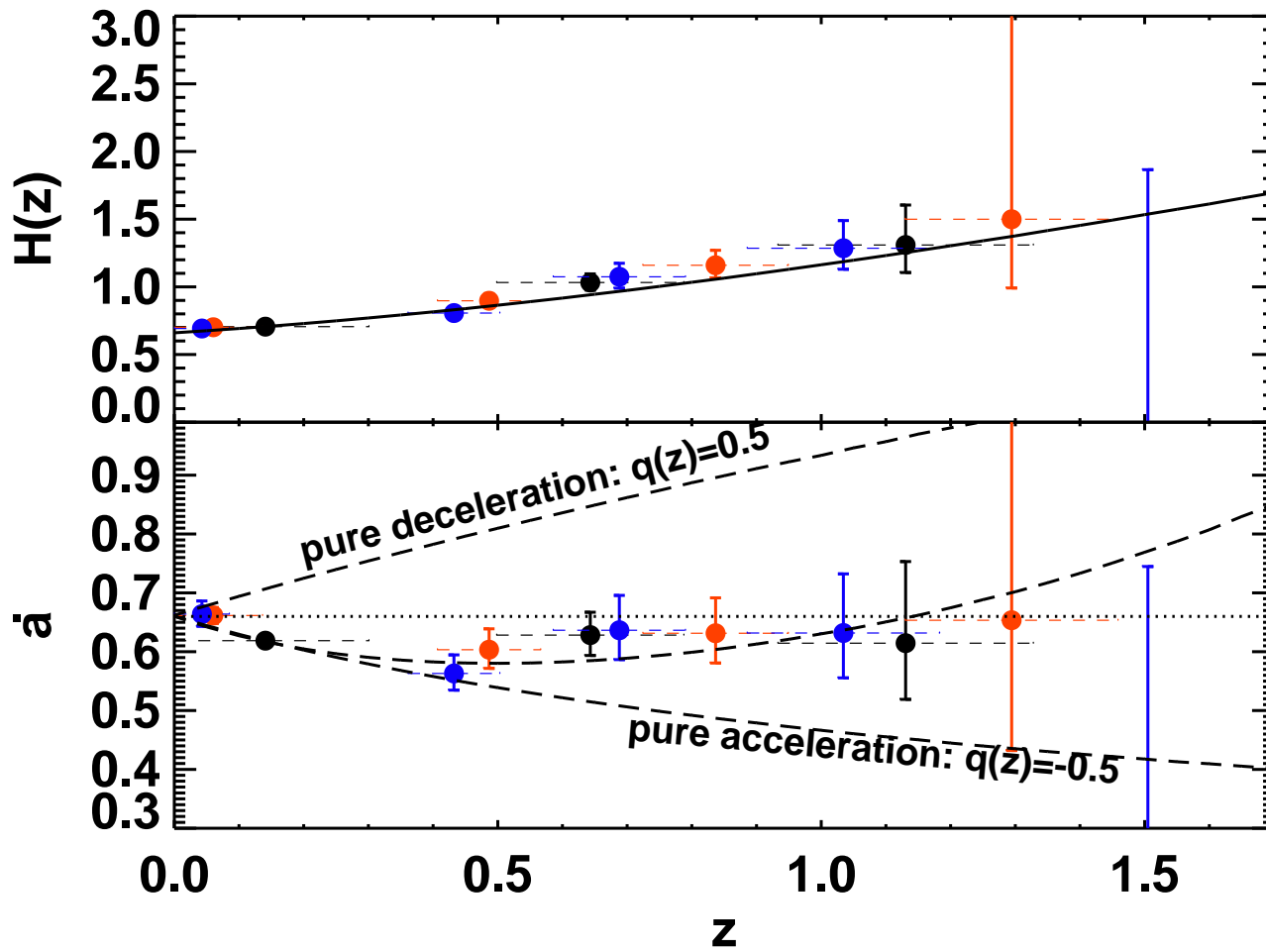


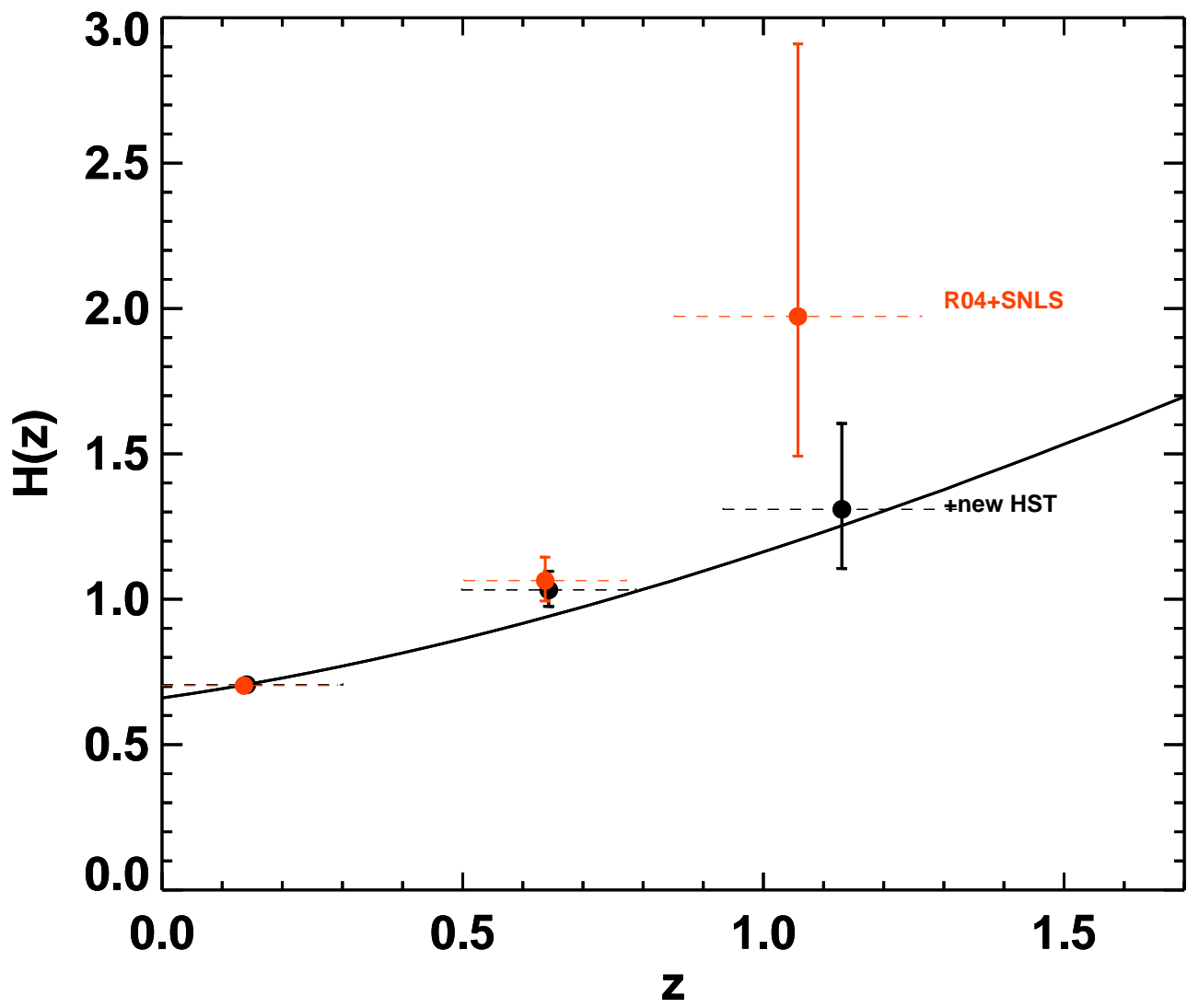


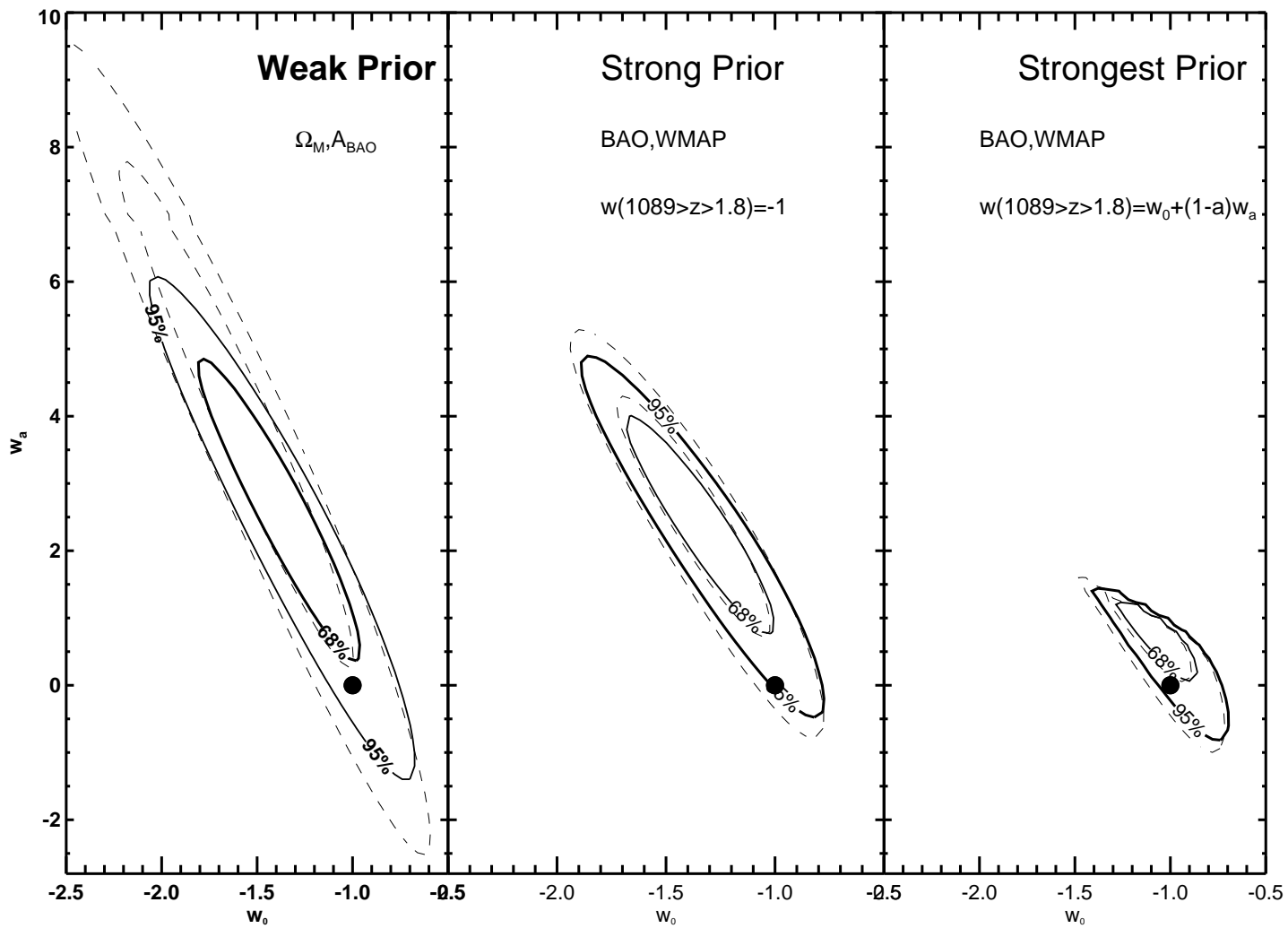


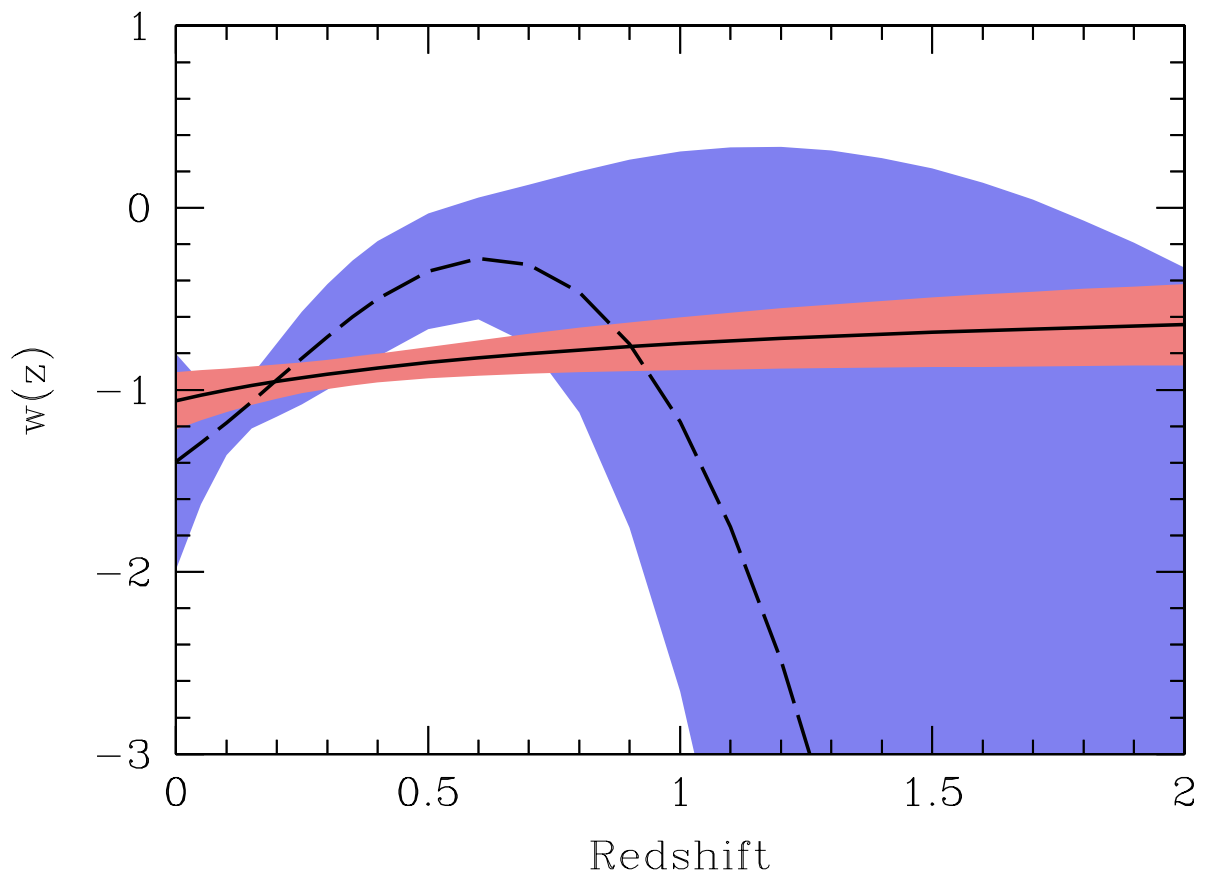


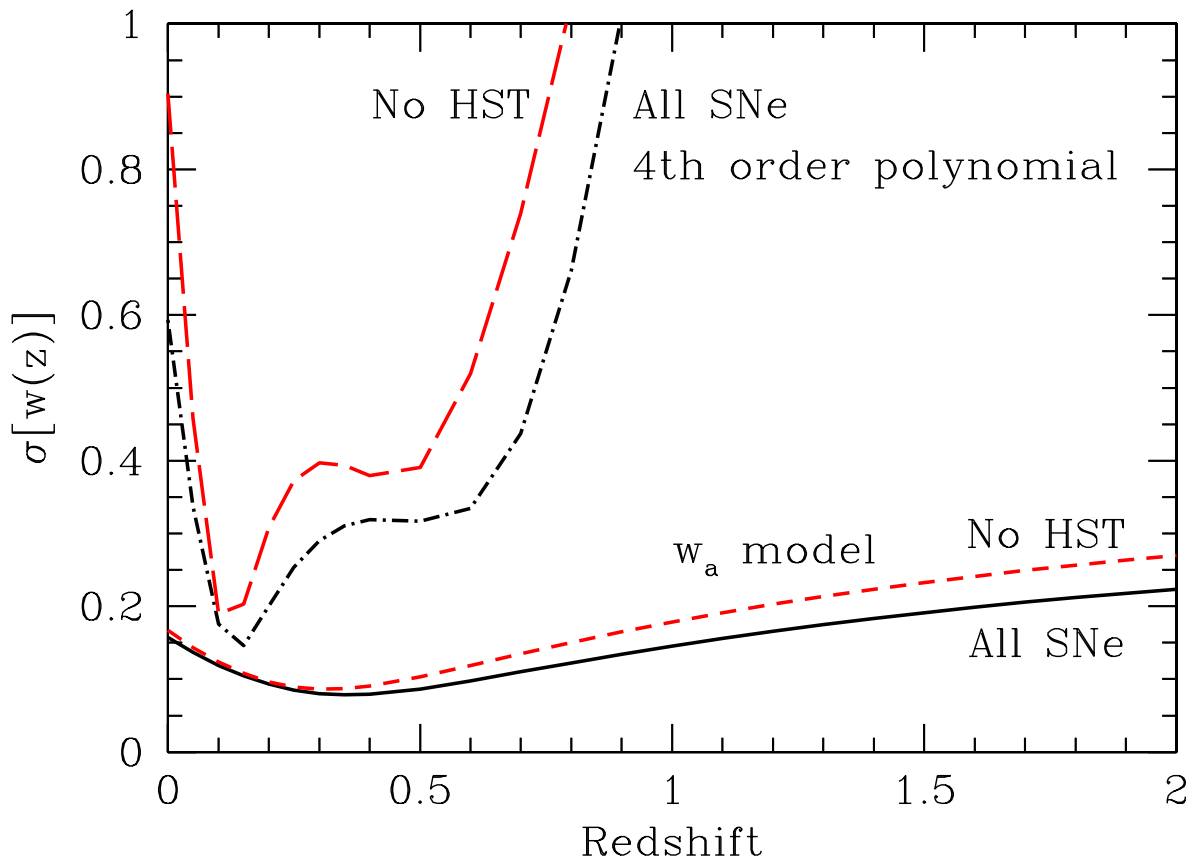


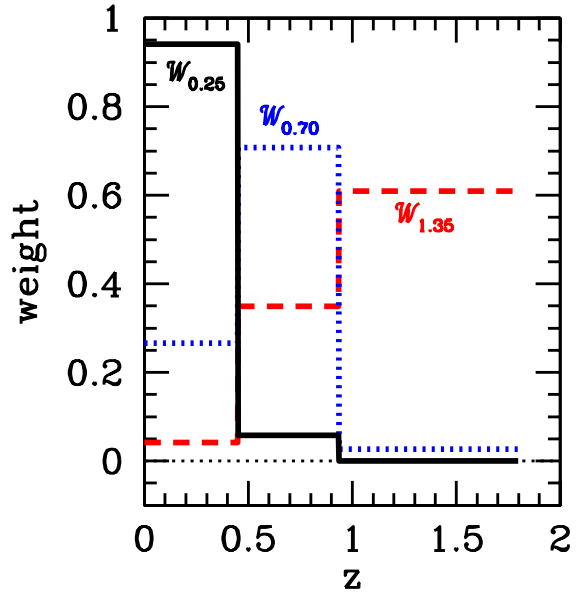
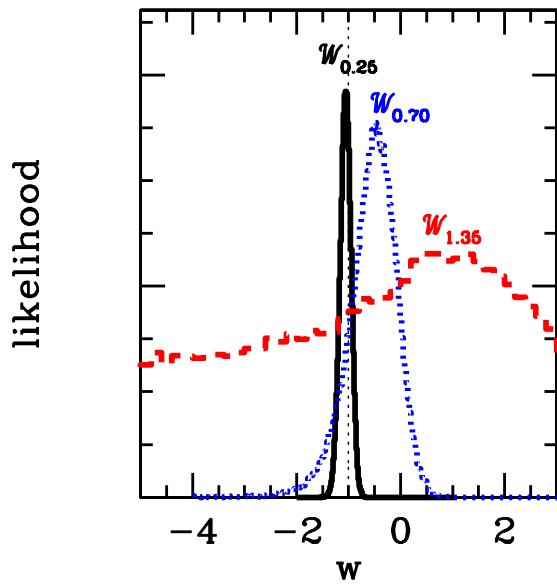
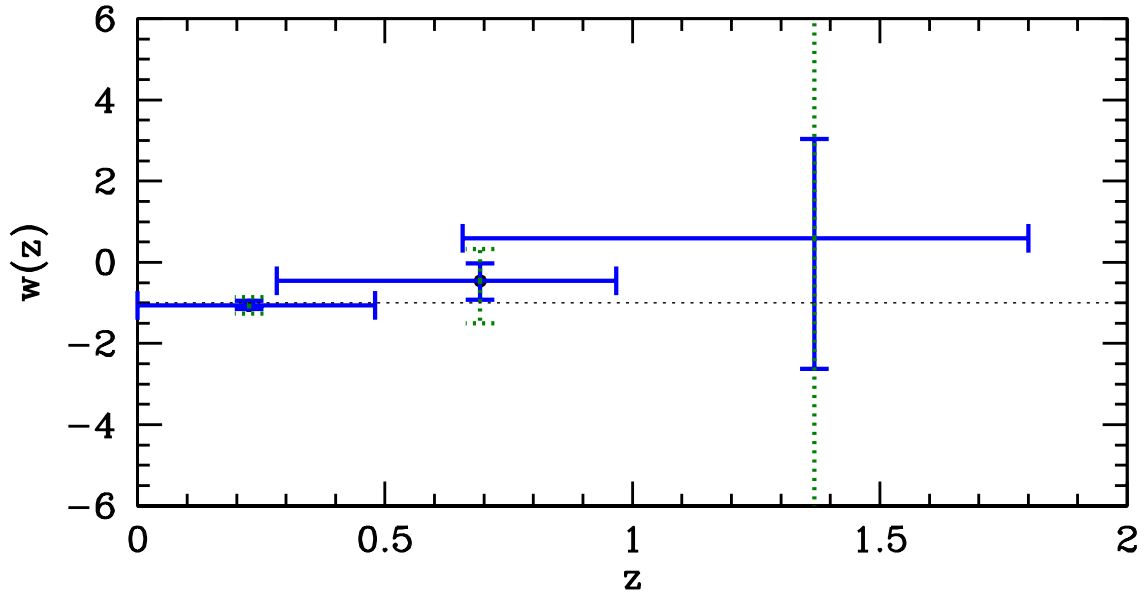


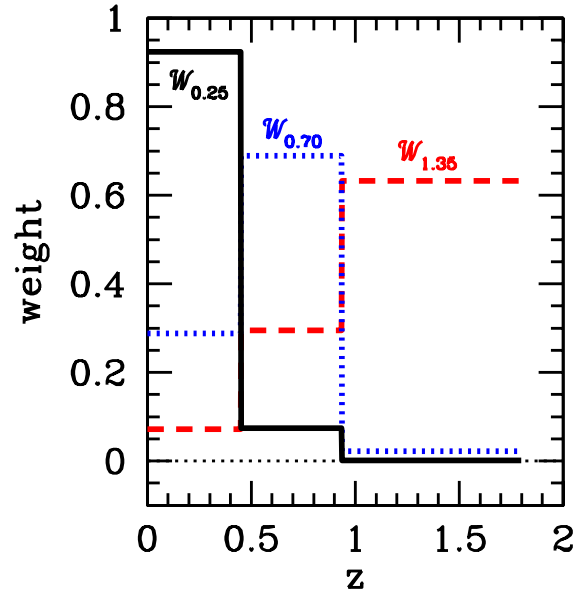
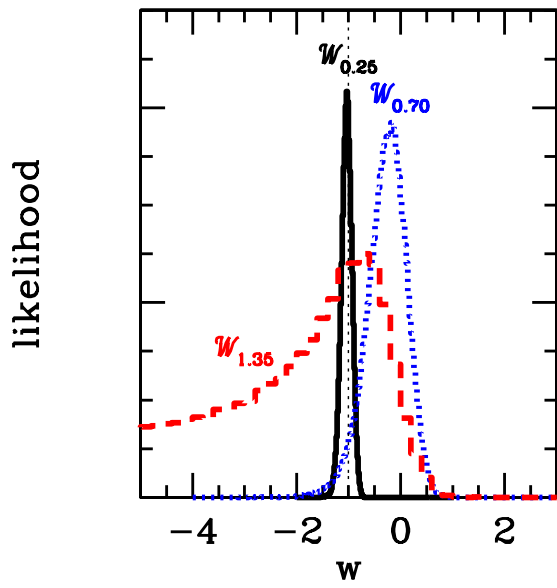
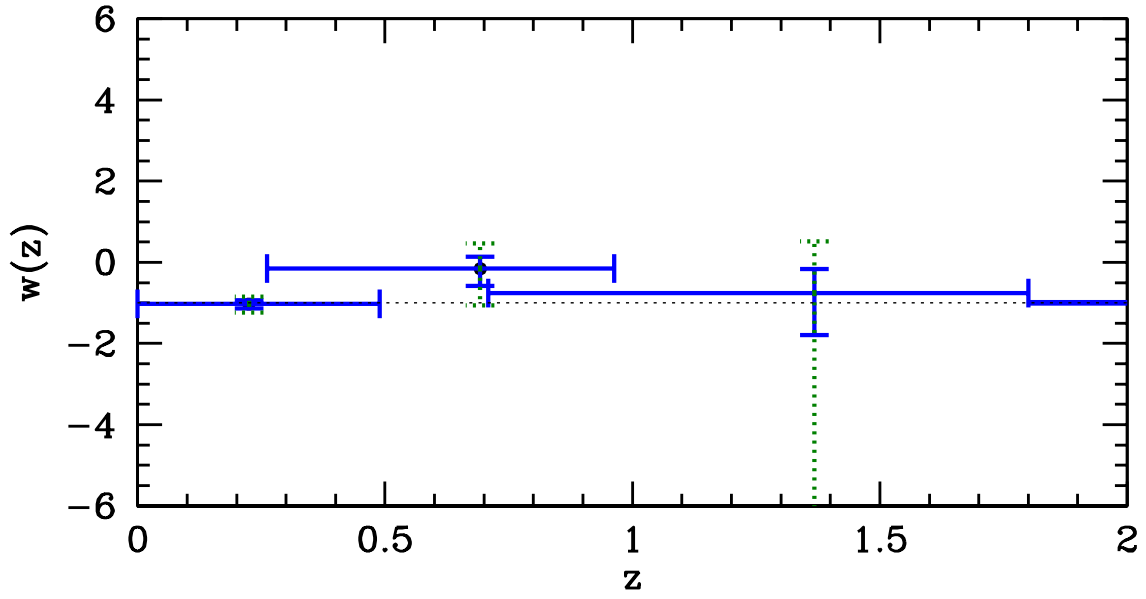


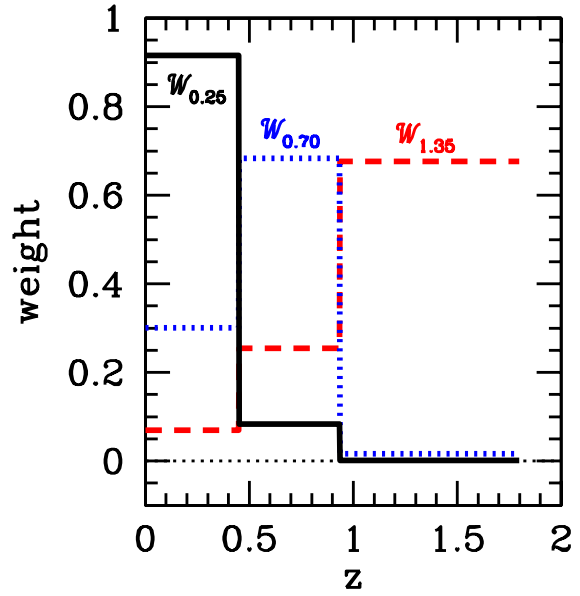
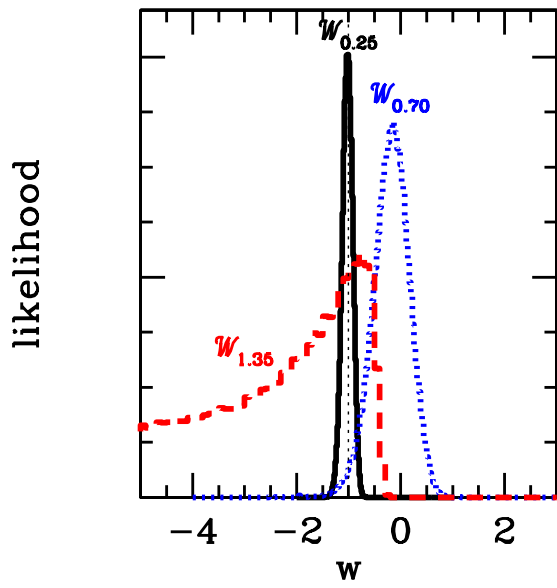
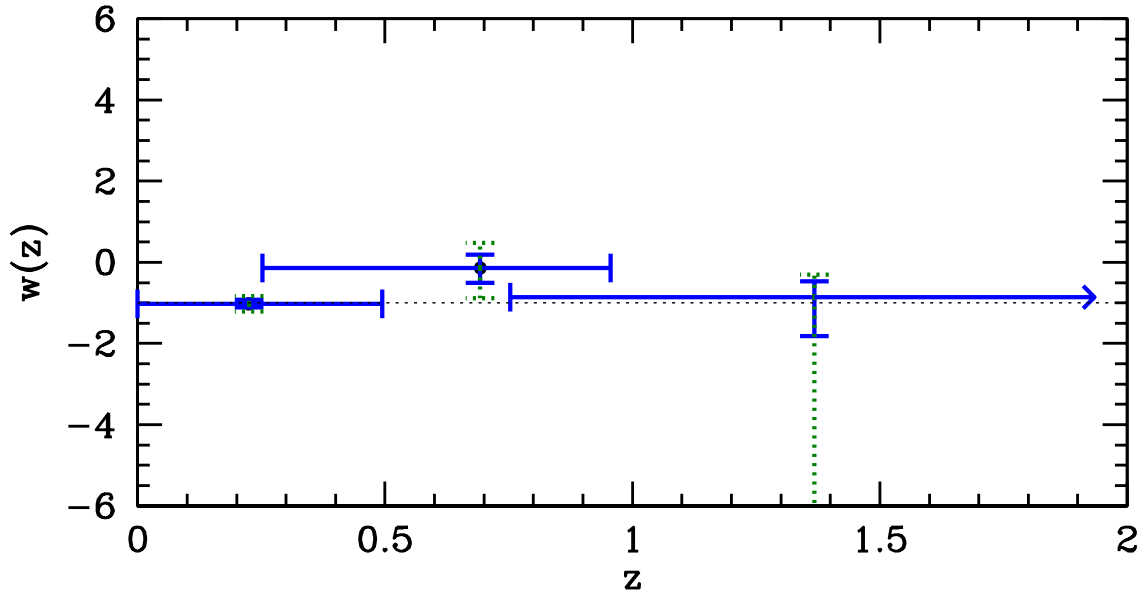


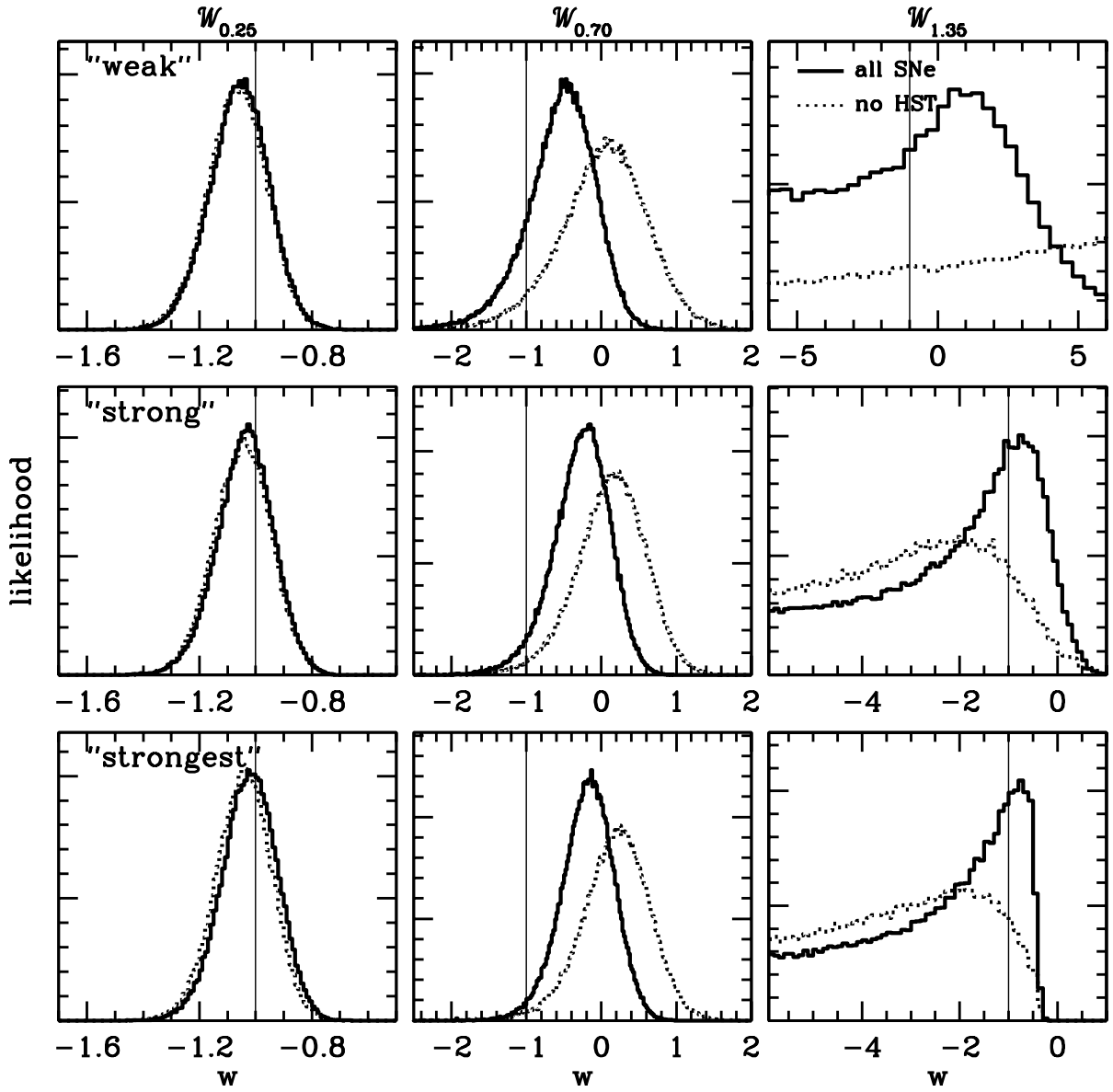


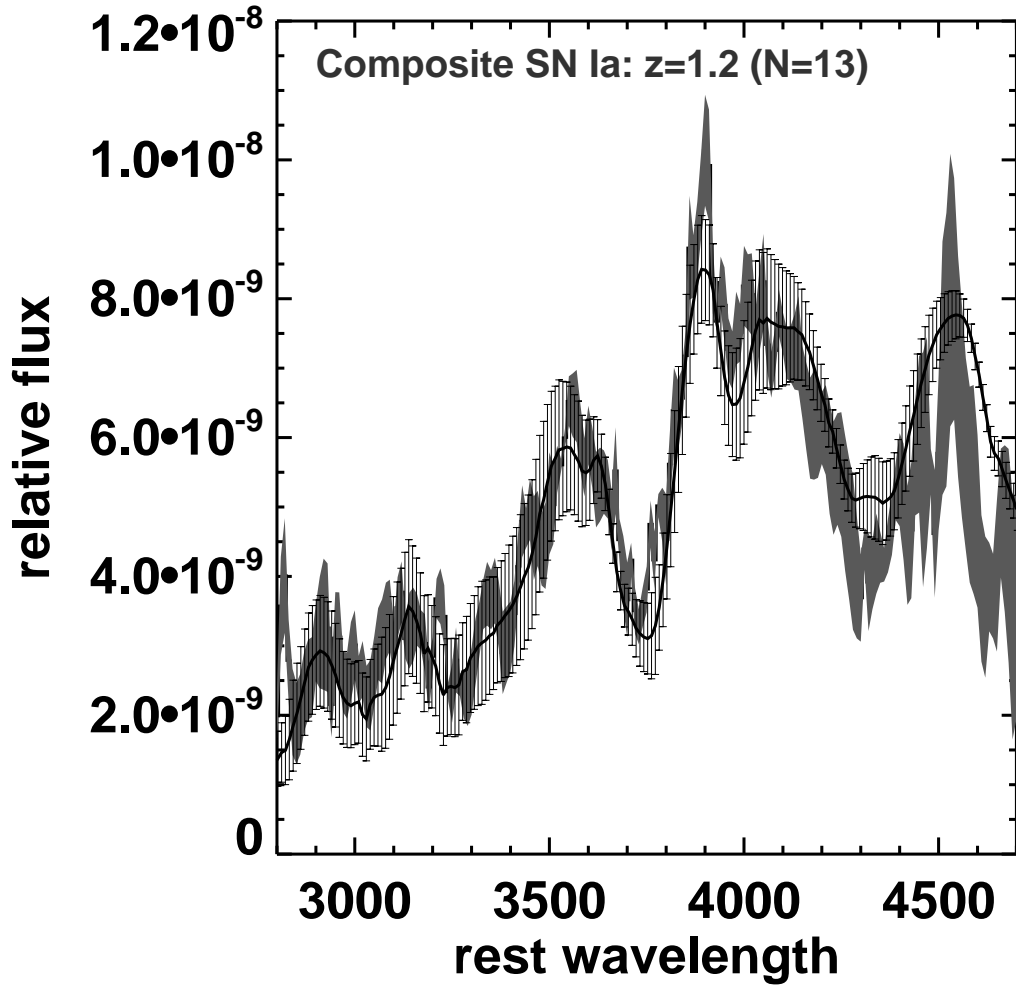












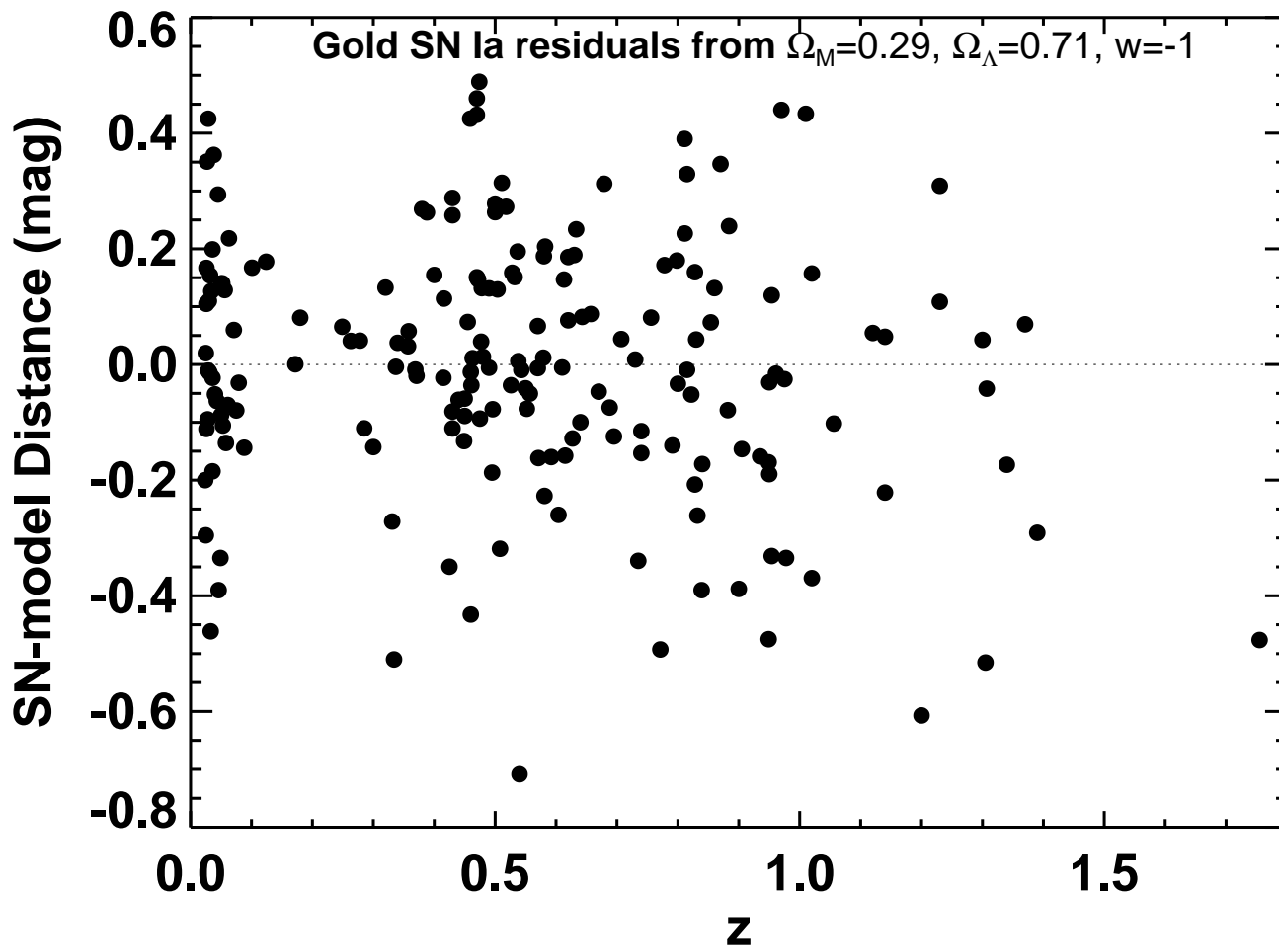


Figure Captions

Figure 1: Discovery-image sections from ACS *F850LP* images around each SN. Panels on the left and middle show the discovery epoch and the preceding (template) epoch, respectively. The panels on the right show the results of the subtraction (discovery epoch minus template). Arrows indicate position of the SNe. Image scales and orientations are given.

Figure 2: Color images of hosts with site of SN indicated. Filters *F850LP*, *F606W*, and *F435W* correspond to red, green, and blue, respectively.

Figure 3: Corrections to single-model PSF fitting photometry in the *F850LP* band for SNe Ia due to the red halo. At red wavelengths, the PSF model and aperture corrections for ACS WFC strongly depend on the monochromatic wavelength of incident light as measured from narrow-band filters. Thus the use of a single PSF model or aperture correction to measure photometry in a wide passband necessitates the use of a correction derived synthetically by weighting the monochromatic photometric variations by the appropriate SN SED. In the upper panel we show this correction for *F850LP* as a function of SN Ia age for different redshifts: 0.75 (asterisks), 1.00 (diamonds), 1.30 (squares), 1.50 (Xs), and 1.70 (triangles). In the lower panel we show the correction as a function of redshift for a SN Ia at maximum light.

Figure 4: Multi-color light curves of SNe Ia. For each SN Ia, multi-color photometry transferred to rest-frame passbands is plotted. The individual, best-fit MLCS2k2 model is shown as a solid line, with a $\pm 1\sigma$ model uncertainty, derived from the model covariance matrix, above and below the best fit.

Figure 5: Identification spectra (in f_λ) of 12 of the new *HST*-discovered high-redshift SNe Ia all shown in the rest frame. Classification features are analyzed in §3. The data are compared to nearby SN Ia spectra of a similar age as determined by the light curves (see Table 3).

Figure 6: MLCS2k2 SN Ia Hubble diagram. SNe Ia from ground-based discoveries in the Gold sample are shown as diamonds, *HST*-discovered SNe Ia are shown as filled symbols. Overplotted is the best fit for a flat cosmology: $\Omega_M = 0.27$, $\Omega_\Lambda = 0.73$. Inset: Residual Hubble diagram and models after subtracting empty Universe model. The Gold sample is binned in equal spans of $n\Delta z = 6$ where n is the number of SNe in a bin and Δz is the redshift range of the bin.

Figure 7: Uncorrelated estimates of the expansion history. Following the method of Wang & Tegmark (2005) we derive 3, 4, or 5 independent measurements of $H(z)$ from the

Gold sample using $n\Delta z = 40, 20,$ and $15,$ respectively. The bottom panel shows the derived quantity \dot{a} versus redshift. In this plane a positive or negative sign of the slope of the data indicates deceleration or acceleration of the expansion, respectively.

Figure 8: Same as upper panel of Figure 7 comparing the improvement to the highest-redshift measure of $H(z)$ due only to the newest *HST* data, i.e. since R04.

Figure 9: Joint confidence intervals derived from SN samples for a two-parameter model of the equation-of-state parameter of dark energy, $w(z) = w_a + w_a z / (1 + z)$. For each panel, constraints from a SN sample are combined with the indicated prior to yield the indicated confidence intervals. The position of a cosmological constant $(-1, 0)$ is shown as a filled symbol.

Figure 10: Best solution and uncertainty for a quartic polynomial fit (blue), and simple $w_0 - w_a$ parameterization using a strong prior (red). As seen, the simple parameterization highly constrains the behavior of $w(z)$ as compared to the polynomial. The greater constraint on $w(z)$ implied by the $w_0 - w_a$ parameterization derives from implicit and unjustified priors on dark energy: that its evolution is monotonic, linear, and most important at low redshifts.

Figure 11: As in Figure 10, uncertainty for $w(z)$ for $w_0 - w_a$ and quartic polynomial parameterizations with and without high-redshift *HST* data.

Figure 12: Measurement of 3 uncorrelated components of $w(z)$ using the Gold sample of SNe Ia and the weak prior. Following the method of Huterer and Cooray (2005) we derived measurements of $w(z)$ in the same 3 redshift bins used in Figure 7 ($n\Delta z=40$). Using their covariance matrix we derived new, uncorrelated components of $w(z)$ shown in the upper panel with window functions given in the lower right panel and likelihoods given in the lower left panel.

Figure 13: Same as in Figure 12 but using the strong prior.

Figure 14: Same as in Figure 12 but using the strongest prior.

Figure 15: Difference between Figure 12,13 and 14 with and without the *HST*-discovered SNe Ia for the weak, strong and strongest prior. However, without the *HST* data, any measurement of the highest-redshift value, $\mathcal{W}_{1.35}$, is not very meaningful because the sample would contain no SNe at $z \sim 1.35$.

Figure 16: Average spectrum derived from *HST* ACS grism spectra of thirteen SNe Ia $z > 1$. The high redshift average and dispersion (mean $z = 1.1$) shown in thick gray compares well to the low redshift average (over the 10 days following maximum) and

dispersion (day-to-day, for the 10 days post maximum) shown as the heavy line with error bars.

Figure 17: Distance difference in magnitudes for all Gold SNe ($cz > 7000$ km s^{-1}) between the measured distance and that predicted for the concordance cosmology ($\Omega_M = 0.29$, $\Omega_\Lambda = 0.71$) with $w = -1$. As discussed in the text, increased complexity in the description of $w(z)$ is not presently justified by the improvement in the fit.

References

- Afshordi, N., Loh, Y.-S., & Strauss, M. S. 2004, *Phys. Rev. D*, 69, 083524
- Aguirre, A. N. 1999a, *ApJ*, 512, L19
- . 1999b, *ApJ*, 525, 583
- Aguirre, A., Haiman, Z., 2000, *ApJ*, 532, 28
- Albrecht, A. & Bernstein, G., 2006, astro-ph/0608269
- Albrecht, A. & Skordis, *Phys Rev. Lett.*, 2000, 84, 2076
- Aldering, G., 2005, astro-ph/0507426, *New Astron. Rev.* 49, 346
- Allen, S. W., Schmidt, R. W., Ebeling, H., Fabian, A. C., & van Speybroeck, L. 2004, *MNRAS*, 353, 457
- Astier, P., et al. 2006, *A&A*, 447, 31
- Balland, C. et al. 2006, *A&A*, 445, 387
- Barris, B., et al. 2004, *ApJ*, 602, 571
- Benítez, N., Riess, A., Nugent, P., Dickinson, M., Chornock, R., Filippenko, A. V. 2002, *ApJ*, 577, L1
- Benot, M.C., Bertolami, O., & Sen, A.A., 2002, *PhRvD*, 66,4, 3507
- Blondin, S., et al. 2006, *AJ*, 131, 1648
- Bohlin, R. C., & Gilliland, R. L. 2004, *AJ*, 127, 3508
- Bohlin, R. C., Lindler, & Riess, A. G. 2005, STScI NICMOS ISR, 2005-002
- Bond, J. R., Efstathiou, G., & Tegmark, M. 1997, *MNRAS*, 291, L33
- Boughn, S., & Crittenden, R. 2004, *Nature*, 427, 45
- Caldwell, R. R., Davé, R., & Steinhardt, P. J. 1998, *Ap&SS*, 261, 303
- Caldwell, R. R., & Linder, E. V. 2005, *Phys. Rev. Lett.*, 95, 141301
- Cappellaro, E., et al. 2001, *ApJ*, 549, L215
- Carroll, S. M., Duvvuri, V., Trodden, M., & Turner, M. S. 2004, *Phys. Rev. D*, 70, 043528
- Casertano, S., & Riess, A. G. 2007, in preparation
- Chevalier, & Polarski, D., 2001, *Int. J. Mod Phys, D10*, 213
- Coil, A. L., et al. 2000, *ApJ*, 544, L111
- Cole, S., et al. 2005, *MNRAS*, 362, 505
- Conley, A., et al. 2006, *ApJ*, 644, 1
- Cooray, A. & Huterer, D., *ApJ*, 1999, 513, L95
- Daly, R. A., & Djorgovski, S. G. 2004, *ApJ*, 612, 652
- Deffayet, C., Dvali, G., & Gabadadze, G. 2002, *Phys. Rev. D*, 65044023
- de Jong, R.. S. et al 2006 astro-ph 0604394
- Di Pietro, E., & Claeskens, J. 2003, *MNRAS*, 341, 1299
- Drell, P. S., Lored, T. J., & Wasserman, I. 2000, *ApJ*, 530, 593
- Einstein, A. 1917, *SPAW*, 142
- Eisenstein, D. J., et al. 2005, *ApJ*, 633, 560

- Filippenko, A. V. 1997, *ARA&A*, 35, 309
- Filippenko, A. V. 2004, in *Carnegie Observatories Astrophysics Series, Vol. 2: Measuring and Modeling the Universe*, ed. W. L. Freedman (Cambridge: Cambridge Univ. Press), 270
- Filippenko, A. V. 2005, in *White Dwarfs: Cosmological and Galactic Probes*, ed. E. M. Sion, S. Vennes, & H. L. Shipman (Dordrecht: Springer), 97
- Fosalba, P., et al. 2003, *ApJ*, 597, L89
- Freedman, W., et al. 2001, *ApJ*, 553, 47
- Freese, K. 2005, *New Astronomy Reviews*, 49, 103
- Giavalisco et al 2004, *ApJ* 600, 93
- Goobar, A., Bergstrom, L., & Mörtzell, E. 2002, *A&A*, 384, 1
- Guy, J., Astier, P., Nobili, S., Regnault, N., & Pain, R. 2005, *A&A*, 443, 781
- Hamuy, M., et al. 2003, *Nature*, 424, 651
- Holz, D. E. 1998, *ApJ*, 506, L1
- Hook, I.M., et al. 2005, *AJ*, 130, 2788
- Howell, D. A., et al. 2005, *ApJ*, 634, 1190
- Huterer, D., & Cooray, A. 2005, *Phys. Rev. D*, 71, 023506
- Huterer, D., & Turner, M., 2001, *Phys Rev D.*, 64, 123527
- Jha, S. 2002, Ph.D. thesis, Harvard University
- Jha, S., Riess, A. G., & Kirshner, R. P. 2006, submitted
- Jönsson, J., Dahlén, T., Goobar, A., Gunnarsson, C., Mörtzell, E., & Lee, K. 2006, *ApJ*, 639, 991
- Knop, R., et al. 2003, *ApJ*, 598, 102
- Knox, L., Christensen, N., & Skordis, C. 2001, *ApJ*, 563, L95
- Kolb, E. W., et al. 2006, *Dark Energy Task Force White Paper*
- Krisciunas, K., et al. 2005, *AJ*, 130, 2453
- Kulkarni, V. P., Fall, S. M., Lauroesch, J. T., York, D. G., Welty, D. E., Khare, P., & Truran, J. W. 2005, *ApJ*, 618, 68
- Landolt, A. U., 1992, *AJ*, 104, 340
- Leibundgut, B. 2001, *ARAA*, 39, 67
- Liddle, A. R. 2004, *MNRAS*, 351, 49
- Linder, E. V. 2003, *Phys. Rev. Lett.*, 90, 91301
- Miknaitis, G. A. et al. 2007, in prep
- Nolta, M. R., et al. 2004, *ApJ*, 608, 10
- Nugent, P., Kim, A., & Perlmutter, S. 2002, *PASP*, 114, 803
- Östman, L., & Mörtzell, E. 2005, *JCAP*, 2, 005
- Peebles, P. J., & Ratra, B. 2003, *Rev. Mod. Phys.*, 75, 559
- Perlmutter, S. 1999, *ApJ*, 517, 565

- Petric, A., Telis, A., Paerels, F., Helfand, D. J., 2006, ApJ in press
- Phillips, M. M., et al. 1999, AJ, 118, 1766
- Pirzkal, N., et al. 2005, ApJ, 622, 319
- Quinn, J.L., Garnavich, P.M., Li, W., Panagia, N., Riess, A., Schmidt, B.P., & Della Valle, M., 2006, ApJ, submitted
- Rana, N. C. 1979, Ap&SS, 66, 173
- Rana, N. C. 1980, Ap&SS, 71, 123
- Riess, A. G., & Livio, M. 2006, astro-ph/0601319
- Riess, A. G., Press, W. H., & Kirshner, R. P. 1995, ApJ, 438, L17
- Riess, A. G., Press, W. H., & Kirshner, R. P. 1996, ApJ, 473, 588
- Riess, A. G., et al. 1998, AJ, 116, 1009
- . 1999, AJ, 118, 2668
- . 2001, ApJ, 560, 49
- . 2004a, ApJ, 600, L163
- . 2004b, ApJ, 607, 665 (R04)
- . 2005, 627, 579
- Schmidt, B. P., et al. 1994, ApJ, 434, L19
- Scranton, R., et al. 2005, ApJ, 633, 589
- Shapiro, C. & Turner, M. S. astro-ph/0512586
- Sirianni, M., et al. 2005, PASP, 117, 1049
- Spergel, D. N., et al. 2006, astro-ph/0603449, in press
- Strolger, L. et al 2004 ApJ 613, 200
- Sullivan, M., et al. 2003, MNRAS, 340, 1057
- Sullivan, M., 2005, private communication
- Szydlowski, M., Kurek, A. and Krawiec, A. 2006 astro-ph/0604327
- Tegmark, M., et al. 2004, ApJ, 606, 702
- Tonry, J. T., et al. 2003, ApJ, 594, 1
- Tripp, R., & Branch, D. 1999, ApJ, 525, 209
- Wang, L., Strovink, M., Conley, A., Goldhaber, G., Kowalski, M., Perlmutter, S., & Siegrist, J. 2006, ApJ, 641, 50
- Wang, Y. 2005, New Astronomy Reviews, 49, 97
- Wang, Y., & Tegmark, M. 2005, Phys. Rev. D, 71, 103513
- Wang, Y., & Mukherjee, P. 2006, ApJ (in press), astro-ph/0604051
- Wetterich, C., 1995, A&A, 301, 321
- Wirth, G. D. et al 2004 AJ 127, 3121
- Wood-Vasey, W. M., et al. 2007, ApJ, submitted
- Wright, E. L. 2002, BAAS, 161.17 (astro-ph/0201196)

Table 6—Continued

SN	z	μ_0^a	σ^b	host A_V	Δ	sample
----	-----	-----------	------------	------------	----------	--------

*The full sample used here for the cosmological analyses consists of the union of Table 5 from Riess et al. 2004, this table (with the new distances to SNe from 2002 to 2003 replacing those in Riess et al. 2004), and the SNLS sample from Astier et al. (2006) listed in §2.3 of this paper. The full sample is also available at <http://braeburn.pha.jhu.edu/~ariess/R06> or upon request to ariess@stsci.edu.

^bRedshift and velocity error and intrinsic SN Ia dispersion of 0.08 mag already included.

^aDistance normalization is arbitrary; see Appendix.